Electronic Thesis and Dissertation Repository

12-9-2015 12:00 AM

Solvothermal Synthesis and Characterization of CuInS2, CuInSe2 and AgInS2 Nanoparticles from Single Source Precursors

Xuzhao Zhao
The University of Western Ontario

Supervisor
John F. Corrigan
The University of Western Ontario Joint Supervisor
Yining Huang
The University of Western Ontario

Graduate Program in Chemistry
A thesis submitted in partial fulfillment of the requirements for the degree in Master of Science
© Xuzhao Zhao 2015

Follow this and additional works at: https://ir.lib.uwo.ca/etd

Part of the Inorganic Chemistry Commons, and the Materials Chemistry Commons

Solvothermal Synthesis and Characterization of $CuInS_2$, $CuInSe_2$
and $AgInS_2$ Nanoparticles from Single Source Precursors

by

Xuzhao Zhao

Graduate Program in Chemistry

A thesis submitted in partial fulfillment
of the requirements for the degree of
Master of Science

The School of Graduate and Postdoctoral Studies
The University of Western Ontario
London, Ontario, Canada

ABSTRACT

Nanoscale semiconductors have emerged as alternative candidates for the absorber layer in solar cells. Group 11-13-16 semiconductors have received a lot attention because of their direct band gap energies, high absorption coefficients and environmental friendly nature. To date, $CuInS_2$, $CuInSe_2$ and $AgInS_2$ semiconductors are three of the main ternary nanomaterials investigated. Besides the application in solar cells, these nanoscale semiconductors can also be applied in areas such as biosensors and hydro catalysis.

However, it is often challenging to prepare small-sized nanoparticles with uniform size and shape, especially for large scale production. In this thesis, the synthesis of $CuInS_2$, $CuInSe_2$ and $AgInS_2$ nanomaterials were probed by using single source precursors via one-step solvothermal reaction. Single source precursors were applied to control the composition, shape and size without the need of balancing the stoichiometric ratio, which is also a challenge for the fabrication of ternary semiconductors. Solvothermal methods can take full advantage of the reaction pressure and simplify the traditional routes for crystallization. Various conditions were investigated including different precursors, reaction temperatures, times and secondary chalcogen source. After optimizing the conditions, products were controlled in a form of wurtzite structure with tunable sizes in a range of 2 to 5 nm, which ultimately tunes the band gap energy. Especially for $CuInSe_2$ nanoparticles, the band gap was successfully tuned to 1.62 eV versus 1.04 eV of bulk $CuInSe_2$, which made this material to be more efficient to generate an exciton pair under exposure to visible light instead of infrared light. In addition, quantum yields of emission for these nanoparticles experienced a slight increase compared to the previously published work, approaching 11.5 % for $CuInS_2$ and 19.0 % for $CuInSe_2$. Also, powder X-ray diffraction, electron microscopy and optical spectroscopy were used to characterize the structures and optical properties.

Key words: semiconductor, $CuInS_2$, $CuInSe_2$, $AgInS_2$, solvothermal method, single source precursor, powder X-ray diffraction, electron microscopy, optical microscopy

ACKNOWLEDGMENTS

To my parents for their love, support, respective and perspective

and

To my friends for their selfless help, suggestions, patience and enthusiasm

CONTENTS

v

LIST OF FIGURES:

VI

LIST OF TABLES:

LIST OF ABBREVIATIONS:

A	Absorbance	m_e^*	effective mass of electron
α	absorption coefficient	m_h^*	effective mass of hole
Å	Angstrom	Me	methyl
AIS	silver indium sulfide	MHz	MegaHertz
^nBu	n-butyl	mL	milliliter
^tBu	tert-butyl	mmol	millimole
℃	Celsius	n	integer
CIS	copper indium sulfide	λ	wavelength of X-ray
CISe	copper indium selenide	n_i	refractive indices of reference
d	lattice spacing of crystal plane	n_s	refractive indices of sample
d (NMR)	Doublet	nm	nanometer
deg	Degree	NMR	nuclear magnetic resonance
DMF	Dimethylformamide	Ph	phenyl
E	chalcogen atom	Φ_f^i	quantum yields of reference
E	band gap energy of nanoparticles	Φ_f^s	quantum yields of sample
E_{gap}	band gap energy of bulk	ppm	parts per million
EDX	energy-dispersive X-ray spectroscopy	PXRD	powder X-ray diffraction
Et	ethyl	QY	quantum yield
eV	electron volts	r	radius of nanoparticles
f_i	absorbance of reference	r	relative space distance
f_s	absorbance of sample	R	organic side group
F^i	emission peak integration of reference	R	reflectance
F^s	emission peak integration of sample	s (NMR)	singlet
g	Gram	S	scattering coefficient
h	hours	SAED	selected area electron diffraction
h	Planck's constant	SEM	scanning electron microscope
HR-TEM	high resolution-TEM	t (NMR)	triplet
$h\nu$	discrete photo energy	T	temperature
K	Kelvin	TEM	transmission electron microscopy
kJ	kilojoule	θ	diffraction angle
L	camera length	TGA	thermogravimetric analysis
m (NMR)	multiplet	THF	tetrahydrofuran
M	Cu, Ag	UV-vis	ultraviolet-visible

CHAPTER 1.Introduction and Literature Review

1.1 Background

In 1988, when the Intergovernmental Panel on Climate Change (IPCC) was established, the deterioration of global climate was first brought to the forefront of the public.[1] Since then, an abundance of research has emerged, supplying unequivocal evidence that the average global temperature is increasing. The use of fossil fuels in the 20th century has been identified as one of the contributing factors to this increase, thereby leading researchers to focus on alternative green energy projects such as fuel cells, batteries, and solar cells.[2] However, compared to the traditional energies, the renewable energies are usually complicated to produce and also costly, so it will be challenging to shift away from fossil fuels if these problems cannot be overcomed.

Among these renewable energies, solar energy conversion is most widely studied. According to recent reviews, the incident solar power received by Earth was around 17.7 Terawatt (TW) in 2014, but such a large amount of energy cannot be utilized efficiently.[3] To date, the percentage of global power coming from solar is less than 1 % and even with conservative growth estimates of 25 % per year, the solar energy used in the year 2040 would still not compose 1 % of the total energy.[4] Clearly, solar energy has huge potential as a major portion of global energy use in the future and the solar cells fabricated in mature procedures and low cost will be the key point. The operating principle in solar energy conversion is the photovoltaic effect, discovered by Edmond Becquerel in 1839.[5] He observed that the silver battery electrodes produced a voltage in an electrolyte upon illumination. The first solid solar cell was developed 38 years later and in the mid-20th century, the formation of revolutionary homojunction and heterojunction solar cell improved the efficiency significantly due to the semiconductor junctions.[6] Until now, the most common solar cells studied are silicon solar cells, thin film solar cells and the third generation solar cells which involves organometallic semiconductors. In order to achieve the goal of producing low-cost, high-efficiency solar cells, nanosized semiconductor materials have risen as a research focus and are very promising to be industrially feasible.

1.2 Semiconductors

As the key part of solar cell devices, semiconductors have received a lot attention due to their characteristic features. As illustrated in Fig. 1.1, semiconductors have electrical conductivity intermediate between that of insulators (e.g. glass) and conductors (e.g. metals). Unlike conductors which have an overlap between the valence and conduction bands, semiconductors have an intrinsic band gap (E_{gap}), typically between 0.1 eV and 4 eV, and the electrons can be excited from the valence band to the higher energetic conduction band by absorbing either a phonon (heat) or a photon (light). However, if the band gap is too large (> 4 eV), the electrons cannot be excited to across the gap and these materials are classified as insulators.[7]
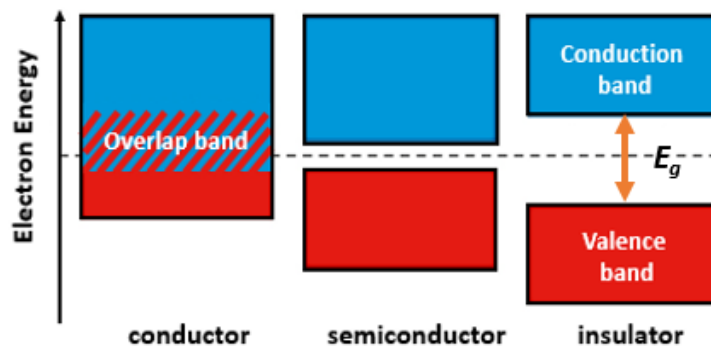
Fig. 1.1 Energy band levels of an insulator, a semiconductor, and a conductor

For semiconductor materials, the conduction band is mostly unoccupied by electrons at room temperature and only a small number of intrinsic electrons have enough thermal energy to pass through the band gap and populate the conduction band.[8] After an electron is excited to occupy the conduction band, a 'hole' is created in the valence band that has charge opposite to that of the electron. This transition creates the formation of an electron-hole pair, known as an exciton. The relative population of electrons and holes in a semiconductor influence the conductivity of the material. There are two different categories of semiconductors: intrinsic and extrinsic. Intrinsic semiconductors have an equal number of electrons and holes, while extrinsic semiconductors have an unequal electron and hole population.[8] And depending on the different concentrations of electron and hole in extrinsic semiconductors, they can be further classified as n-type and p-type. N-type semiconductors have more electrons than holes, while p-type semiconductors have more holes than electrons.

2

1.3 Nanoscale Semiconductors and Quantum Confinement

1.3.1 Nanoscale Semiconductors

As is well known, the performance of photovoltaic solar cells is intimately related to the properties of the semiconductor materials used. Recently, semiconductor materials in nanoscale have been investigated and pursued in order to improve the properties of photovoltaic bulk semiconductors, such as electrical conductivity and optical response.[9] Nanoscale semiconductors are a class of nanomaterials having at least one dimension in the range of 1-100 nm. According to their dimensions, they can be classified as (1) zero-dimensional (0-D), wherein all the dimensions are confined to nanoscale, such as nanoparticles and quantum dots; (2) one-dimensional (1-D), which have two dimensions within 100 nm and no confinement along the third dimension, such as nanorods and nanowires; (3) two-dimensional (2-D), which means two dimensions are out of confinement such as nanofilm and nanosheets with only one dimension is at nanoscale and (4) three-dimensional (3-D), which are usually referred to as bulk materials (Fig.1.2).[10]
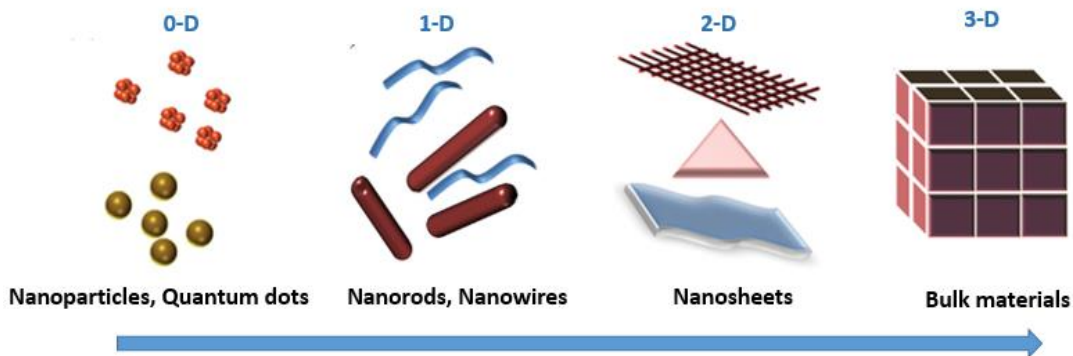
Fig. 1.2 Classification of nanosemiconductors based on dimensionality
(Reproduced with permission from ref. 10. Copyright © 2011 Nano Reviews)

Because the size of nanoscale semiconductors is between that of typical molecules and bulk solids, they usually demonstrate unique size-dependent phenomena including optical, thermal and magnetic properties, all of which cannot be observed in bulk or molecular materials.[11-15] It is important to understand the reasons behind these unique properties first and then explore how to synthesize the nanoscale semiconductors in an industrially feasible procedure.

1.3.2 Quantum Confinement Effect and Size-dependent Properties

To some extent, the science of nanomaterials is driven by size. Compared to bulk materials, solids at the nanoscale can display features that distinguish them from the intrinsic properties of the bulk. The reason behind this is referred to as the quantum confinement effect. When the diameter of a material is small enough, that it is of the same magnitude as the size of the material's exciton Bohr radius, quantum confinement effects can be observed and this is the source for unique quantized properties of the material.[16, 17] Under this circumstance, the exciton is confined by the dimension of the material and the electronic structure is intermediate between that of a single molecule and that of the corresponding bulk material. In another words, the continuous energy spectrum becomes discrete states.[18] As a result, the band gap energy of the particle become size-dependent, as shown in Equation 1.1, where E is the band gap energy of nanoparticles, E_{gap} is the band gap energy of the same material in bulk, h is the Planck's constant, r is the radius of the quantum dots and $m_e{}^*$ and $m_h{}^*$ are the effective masses of the electron and hole, which are the masses that it seems to have for the material when responding to lattice forces. From this equation, it is obvious that as the size decreases, the band gap energy of the quantum dot increases, allowing optical spectroscopy to visualize these radii changes. However, this is a simplified equation which neglects the coulombic interaction between the charge carriers in the confined systems, and offers a convenient method to estimate the particle size from the band gap energy.

$$E = E_{gap} + \frac{h^2}{8r^2} \left(\frac{1}{m_{e*}} + \frac{1}{m_{h*}} \right) \qquad \text{Equation 1.1}$$

Due to the quantum confinement effect, the size of the particles has a significant role on the optical properties.[19, 20] For example, it is well known that when the particle size is tuned, the wavelength of the peak maximum in absorption spectra will shift accordingly, without altering the chemical composition. Xie *et al.* demonstrated a red shift in the absorption spectra of $CuInS_2$ nanoparticles when increasing the size from 2 nm to 16 nm (Fig. 1.3 (A)).[19] Similarly, the emission spectra of $CuInS_2/ZnS$ quantum dots, in which ZnS was coated on the surface of $CuInS_2$ core to form a core/shell structure, was tuned to cover the range from visible to infrared (Fig. 1.3 (B)).[19] All of these modifications will contribute to obtain a high efficiency of the solar energy conversion.

4
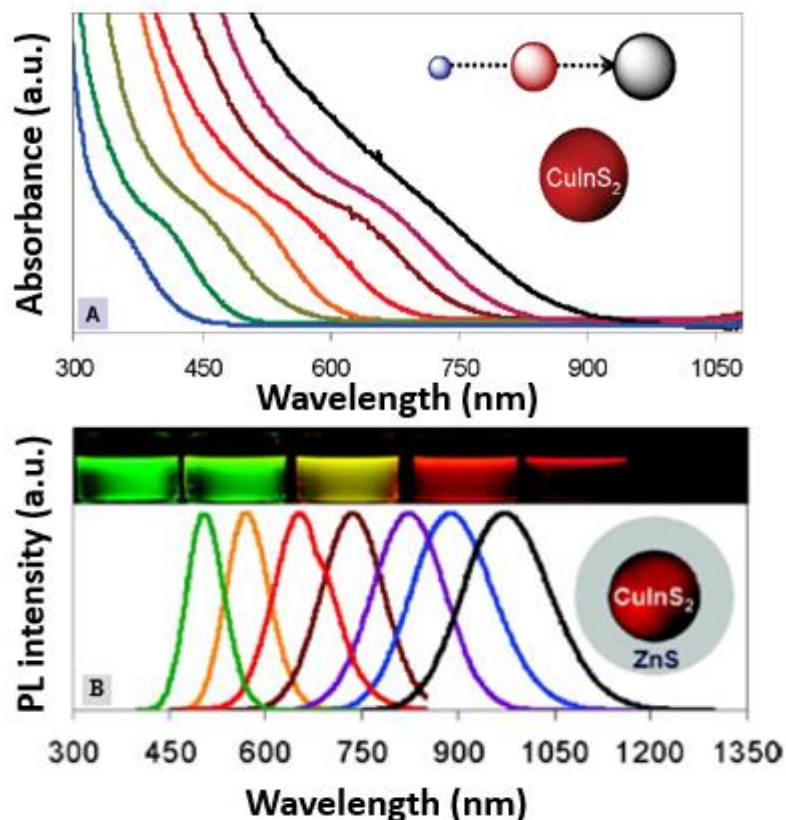
Fig. 1.3 Optical properties of nanoparticles in different sizes
(A) Absorption spectrum of CuInS$_2$ nanoparticles
(B) Photoluminescence spectrum of CuInS$_2$/ZnS nanoparticles)
(Reproduced with permission from ref. 19. Copyright 2009 © American Chemical Society)

Although particle size has an important influence on the optical properties, the morphologies and the crystal facets are also important. The morphologies of nanoparticles can be controlled to tune their performance for certain applications. For instance, Pd nanocrystals have five different crystal morphologies, among which the cubic shape was found to be the best structure when used as a catalyst for formic acid formation.[21] CuInS$_2$ nanoparticles have also been known for several decades but only recently more morphologies have been prepared and the wurtzite structure is believed to be the most efficient structure for the absorber layer of solar cells.[22] It was found that the properties of nanoparticles are also related to the surface modification.[19, 23] For example, when using ammonium thiocyanate (NH$_4$SCN) as ligand to synthesize metallic nanoparticles instead of long-chain, insulating ligands, it can enhance the electronic coupling between nanoparticles and further increase the conductivity of the material.[23]

5

As a result, the control of both size and morphology is very important but difficult to achieve. In order to synthesize nanoparticles which have good properties, a central theme is to obtain those with controllable size and uniform morphology through preparative methods. To date, there are several different reported methods for fabricating nanoparticles in a manner that allows their sizes and shapes, even surface chemistry to be manipulated, and further control the optical properties and surface reactivity. For metal chalcogenide nanoparticles, they are often prepared by metathesis reaction involving salt [24] or silane elimination.[25, 26] But recently, it is found that by utilizing small clusters as building blocks, the clusters can be rearranged to form nanoparticles with controllable size and shape through methods such as photolytic decomposition [27] or solvothermal synthesis.[28]

1.4 Types of Semiconductors

According to the number of elements in the formation of materials, semiconductors can be divided into unitary (e.g. silicon), binary (e.g. ZnO, CdS), ternary (e.g. $CuInS_2$, $CdIn_2Se_4$), quaternary (e.g. Cu_2ZnSnS_4) and even quinary classes.[29-32] Based on the element's position in the periodic table, they can also be further classified as Group 14 semiconductors, 13-15 semiconductors, 12-16 semiconductors, 11-17 semiconductors, 11-13-16 semiconductors, 12-13-14 semiconductors and so on.

1.4.1 Structures of Different Semiconductors

The Group 14 semiconductors are the most traditional semiconductors and are also called elemental semiconductors due to the single element type involved. To date, Group 14 semiconductors have been widely explored for a variety of applications in electronic devices and already been produced in a large scale. All the elemental semiconductors of this group crystallize in a diamond structure. As shown in Fig. 1.4 (a), it is a face-centered cubic structure with a repeating pattern of 8 atoms connected by covalent bonds. In the structure, each atom is surrounded by four equidistant atoms and positioned at the corners of a regular tetrahedron.[33]

Group 13-15 and Group 12-16 semiconductors are two relatively mature groups among binary semiconductor materials. As indicated by the name, this group of

6

semiconductors contains two elements, thus, the bonds between the two different elements are no longer as symmetric as those in Group 14 semiconductors. The bonds display both covalent and ionic character, with electron distribution closer to a covalent system. These substances crystallize in two different structures as shown in Fig. 1.4 (b): zinc blende and wurtzite structures, in both of which, the cations occupy one of the two types of tetrahedral corners. In either structure, the nearest neighbor connections are similar (tetrahedral coordination), but the repeating order of zinc blende is ABC while the wurtzite structure is ABAB repeating. Also, they have different numbers of asymmetric units that zinc blende has 4 whereas wurtzite only has 2.
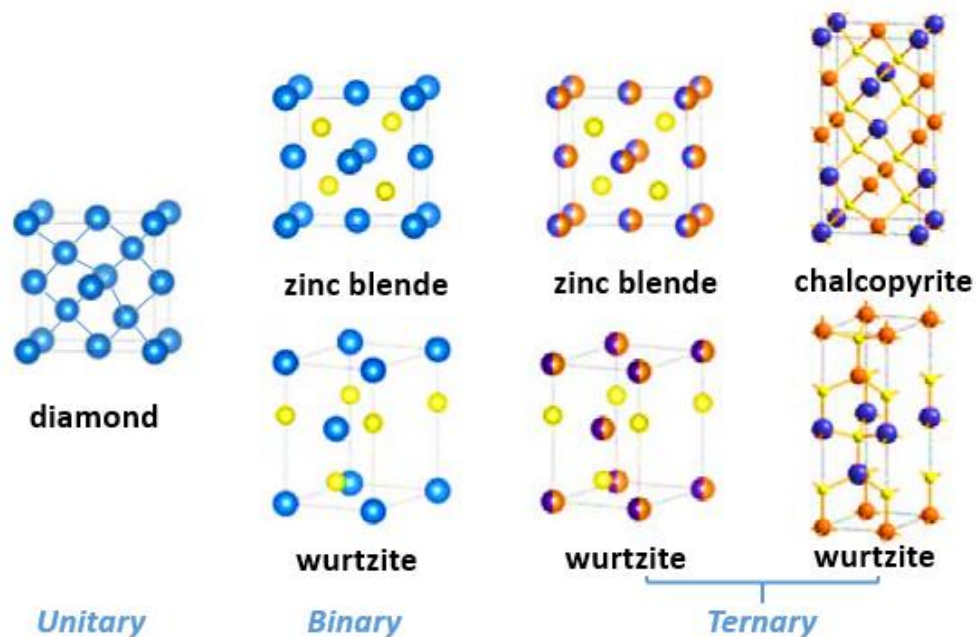
Fig. 1.4 Illustration of structural derivation from unitary to binary and ternary [34, 35]

The ternary semiconductors, generally speaking, are a derivation of a binary semiconductor just like quaternary is derived from ternary.[34, 35] The ternary semiconductors include Groups 12-14-15, 11-13-16 and 12-13-14, the last of which is much rarer when compared with the first two types. Based on the structure of binary class, the ternary semiconductors crystallize in three different structures: chalcopyrite, zinc blende and wurtzite structures. Both zinc blende and wurtzite structure possess the same crystal structure as in the binary class, however the metal sites are occupied by two different cations. The chalcopyrite structure is considered as a super-lattice of the zinc blende structure, consisting of two inter-penetrating face-centered cubic lattices (Fig. 1.4 (c)).

7

1.4.2   11-13-16 Metal Chalcogenide Nanoparticles

Among these semiconductors in different groups, elemental semiconductors and binary semiconductors such as crystalline silicon,[36] cadmium chalcogenides (CdS and CdSe),[37, 38] TiO$_2$,[39] ZnO,[40] and PbS [41] have been the most heavily investigated. Although some of which have already been commercialized due to a number of merits such as suitable band gap energies, high conversion efficiency and low toxicity,[42-44] each of them also has some disadvantages.

Table 1.1 Comparison of different types of semiconductor materials for photovoltaic device application [36-42, 45-48]

Semiconductors	Type	Band Gap (eV)	Transition Type	Conversion Efficiency (%)	Toxic
Crystalline Si	14	1.12	Indirect	18.0	✗
ZnO	12-16	3.63	Direct	4.7	✗
CdTe	12-16	1.44	Direct	16.0	✓
CdS	12-16	2.42	Direct	15.1	✔
GaAs	13-15	1.42	Direct	30.3	✓
CuGaSe$_2$	11-13-16	1.68	Direct	33.9	✗
CuInS$_2$	11-13-16	1.55	Direct	32.0	✗

Crystalline silicon is most widely used as the photovoltaic absorber material in large-scale production. However, this elemental semiconductor is indirect band gap semiconductors as shown in Table 1.1. The indirect nature of band gap means that the minimal-energy state in the conduction band and the maximal-energy state in the valence band have different momenta. Thus, in order to form an exciton pair, more energy is needed to process a transition in momentum. Due to this fact, it cannot provide a favourable conversion efficiency and will miss a sufficient amount of incident photons. This low probability transition results in a small absorption coefficient and limits the ability of silicon to make fully use of incident light except when fabricated in very thick layers.

8

Unlike crystalline silicon, binary semiconductors are direct band gap materials.[48] If they have favourable band gap energies, they will exhibit a high molar absorptivity and a high conversion efficiency, both of which are attractive for further applications.[49-51] However, they are also burdened by some negative aspects. For instance, ZnO have a large band gap of and 3.63 eV, which requires higher energy to excite electrons and form exciton pairs.[53] Since early 1993, CdTe and CdS have been widely explored and have become promising solar cell materials due to their suitable band gaps.[46] Although the efficiency is only 15 - 16 %, the easy-controlled synthesis procedures allowed their rapid development from the laboratory to industrial production. However, from the view of green chemistry, no one can ignore the health concern about the toxicity of this type and the relatively low abundance of cadmium and the heavier chalcogenides will limit industrial production. GaAs, the typical material for Group 13-15 semiconductors, does not have the element as extremely toxic as Cd (although As is still toxic) and is promising to be a replacement of CdTe. It also has outstanding photophysical features, especially the emissive properties, which are at a level comparable to that of cadmium chalcogenides.[42, 47] However, the synthesis of GaAs usually involves expensive, unstable and hazardous precursors, such as $As(SiMe_3)_3$, thus it is very difficult to apply in large-scale process. As a result, people start to turn their attention to ternary or quaternary semiconductor materials which enjoy the same advantages as binary material, but they also offer some extraordinary merits to improve upon the drawbacks mentioned above.[45]

Among the ternary metal chalcogenide semiconductors, the 11-13-16 family has been a focus in photovoltaics.[54, 55] As direct band gap semiconductors, it is possible for them to obtain colour-tunable emitters from visible to near-infrared (NIR) regions of the photoluminescence spectrum with high extinction coefficients. Even though this kind of photovoltaic device is known to be less expensive than other types of solar cells fabricated by molecular beam epitaxy or related techniques, cost is still a roadblock. There are two efficient ways to lower the cost associated with fabrication. The first one is to find a method, which can be used to fabricate high quality semiconductor thin films through simplified procedures. Korgel *et al.* used solution-based techniques to avoid traditional complicated procedures and this method was further confirmed as a "cost-saving" way.[56]

9

The second one is to synthesize high efficiency semiconductor materials from inexpensive precursors, thus photovoltaic devices can be fabricated by using these inexpensive materials to control the expense.[57] Borchert *et al.* have developed a nano-engineered heterojunction solar cell using $CuInS_2$ nanocrystals which showed high conversion efficiency, while the cost is much lower than other devices.[58] However, in both approaches, it is crucial to obtain monodisperse nanoparticles with uniform size and morphology which contribute to a high efficiency.

1.4.3 $CuInS_2$, $AgInS_2$ and $CuInSe_2$ Nanoparticles

Among the 11-13-16 family, $CuInS_2$, $AgInS_2$ and $CuInSe_2$ are the most typical chalcogenide semiconductors. All of them have band gaps that match with solar energy, which means they are the suitable materials to fabricate absorber layers of the solar cell as shown in Fig. 1.5. As shown, a solar cell contains at least five layers. Transparent materials such as glass are commonly used as substrate and a back contact layer is coated on the surface of substrate. The back contact layer usually has a good contact with absorber layer to decrease the voltage of interface and it also acts as a reflection layer to reflect reflects unabsorbed light back into the absorber layer. Absorber layer is the key part of devices and as the working layer it converses photons to excitons. In order to equilibrate the system efficiently, buffer layer is required between absorber layer and front contact, which has an opposite extrinsic type to absorber layer to collect and move electrons out of the cell.[61, 62] To date, the highest conversion efficiency that has been reached is 20.3%, which is from polycrystalline Cu(In, Ga)Se$_2$ devices.[59, 60] With similar compositions, $CuInS_2$, $AgInS_2$ and $CuInSe_2$ are also good options with promising prospects for fabrication into stacked cells.

Front contact (ZnO)

Buffer (CdS)
Absorber (CuInS$_2$, AgInS$_2$, CuInSe$_2$)
Back contact (Mo)
Substrate (glass)
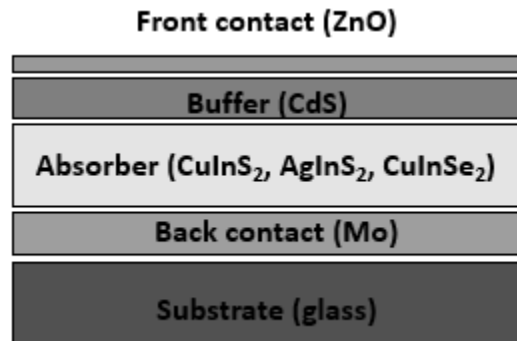
Fig. 1.5 Cross section of solar cells

CuInS$_2$, the most researched material in this family, has a direct band gap of 1.53 eV and a high conversion efficiency of 10^5 cm^{-1},[63] which means that incident photons can be easily absorbed by this material and greatly enhance the opportunity to form exciton pairs.[63, 64] With such a high conversion efficiency, CuInS$_2$ would be able to be implemented as thin layers without sacrificing the quality of the material, which is challenging for the traditional devices such as silicon based solar cells. Thus, CuInS$_2$ is a potential material to overtake the shortcomings of traditional semiconductors, getting rid of the limitation of the thickness. When decreasing the size of produced CuInS$_2$ to nanometer scale, more interesting optical properties can be observed such as larger range of absorption wavelength and tunable emission region, all of which can contribute to the potential and specific applications in the future. However, CuInS$_2$ in nanoscale is a relatively new material, although bulk CuInS$_2$ has been studied for years.[53, 56]

Research in another direct band gap material, CuInSe$_2$, was first reported in 1953 by Hahn,[65] as one of the earliest ternary semiconductor materials studied. Until now, CuInSe$_2$, especially in nanoscale, still attracts a large amount of attention. Compared to CuInS$_2$, the smaller band gap (1.02 eV) makes it more challenging to tune the band gap energy to fit the solar spectrum. However, by changing the particle size, CuInSe$_2$ achieved a good efficiency and has been considered as one of the most promising materials for absorber layer. Also, by introducing Ga inside CuInSe$_2$, an outstanding conversion efficiency about 20.3 % is shown and this is the highest efficiency obtained until now.[66, 67]

AgInS$_2$-based materials are also an alternative to fabricate high efficiency absorber layers in solar cells. With a band gap energy of $\sim$ 1.9 eV,[68] it was first believed to be not as good as other materials in performance. However, because the lattice parameter of AgInS$_2$ crystals is almost same as that of Cu(In, Ga)Se$_2$, this material was reinvestigated and showed a promise in conversion efficiency.[69] It was also noticed recently that if AgInS$_2$ was controlled effectively to obtain reasonable size distribution and well defined spherical morphology, it showed high photoluminescence quantum yield ($\sim$ 41%).[70] Thus, how to achieve a suitable morphology and size distribution of AgInS$_2$ nanocrystals will be very crucial in the synthetic process of AgInS$_2$.

11

Overall, these three materials are promising for fabrication into absorber layers of optical devices due to the high conversion efficiency as well as being environment friendly. Due to their quantum optical properties for the nanoparticles, especially for AgInS$_2$, it is believed that they can also act as the alternative luminescent semiconductors, offering the potential applications such as photocatalysts, optical devices, biomolecular tags and light emitting diodes (LEDs).[71-73]

More details about these three materials such as structure and properties will be introduced in the following related chapters.

1.5 Synthesis Techniques and Methods

There are many methods available for the fabrication of nanomaterials since nanotechnology is one of the most investigated areas in the modern science. Depending on the state of the starting material, synthetic routes can be divided into vapor-phase, liquid-phase and solid-phase methods. For vapor-phase methods, techniques such as vapour deposition,[74, 75] magnetron sputtering [76] and laser ablation [77] are often used for the reaction whose starting materials are in gaseous form. Liquid-phase routes such as sol-gel, hydrothermal/solvothermal, hot-injection, and electrochemical synthesis are commonly involved. If using solids as starting materials, the favored processes are high-energy ball milling, equal channel angular extrusion, and lithography techniques. For both vapor-phase and liquid-phase synthesis, the route are usually called bottom-up which means combining small building blocks to form nanoparticles, while for the solid-phase methods, the reactions involved are categorized as top-down which means break down the bulk into particles in nanoscale. According to the criterion of industrial feasibility as well as the convenient control of procedures, liquid-phase methods are most commonly used.

Since 11-13-16 ternary chalcopyrite semiconductors have potential for many applications, many synthesis methods have been investigated and various nanostructures such as nanoparticles,[78, 79] hollow nanospheres [80] and nanorods [81, 82] have been synthesized. To date, the most common methods include colloidal synthesis,[83] single source decomposition,[27] solvothermal,[84, 85] and microwave irradiation.[86]

12

1.5.1 Schlenk Techniques

Schlenk techniques are one of the most traditional routes for liquid-phase synthesis.[87] The Schlenk line is a commonly used chemistry apparatus developed for oxygen and water free conditions during synthesis, and since all the precursors for $CuInS_2$, $AgInS_2$ and $CuInSe_2$ are air sensitive compounds, this technique is used for the synthesis of the precursors in this project. The Schlenk line consists of a dual manifold with three ports. One manifold is connected to a source of purified inert gas (typically using N_2 gas in our experiments), while the other is connected to a mechanical pump. In experiments, the reaction flask is firstly pulled to vacuum, and then the system is filled with N_2 gas. The reaction flask which contains starting materials is pulled to vacuum and filled with N_2 and the line can be connected with reaction bottles under N_2 flow.[87, 88] Thereafter, required solvents can be transferred inside the reaction bottle and after the reaction is complete, all the filtration and crystallization procedures are also performed under N_2 flow to avoid oxygen and water.

1.5.2 Single Precursor Synthesis

One obvious challenge for fabricating ternary nanocrystals is to balance their ternary composition and control the ratio of precursors. The stoichiometric ratio between the Group 11 and Group 13 elements may vary substantially with different structures.[89] As a result, single source decomposition is highly simplified the routes of synthesis to fabricate a material in an intended way or with a specific structure. As an example shown,
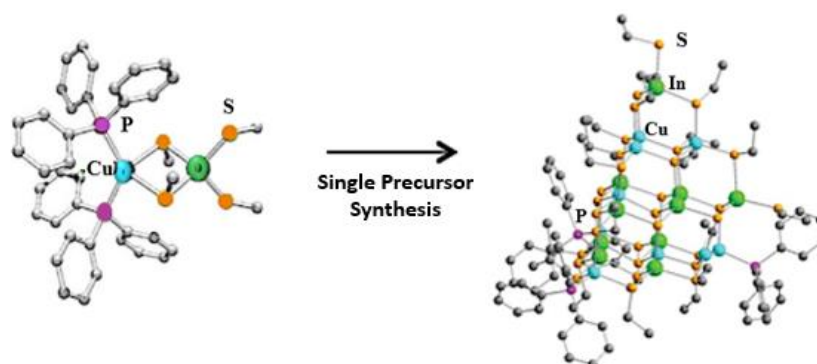
Fig. 1.6 $Cu_9In_{10}S_9(SEt)_{21}(PPh_3)_3$ nanocluster synthesized through single source decomposition method (Yellow: Sulfur; Green: Indium; Blue: Copper; Purple: Phosphorus) (Reproduced from ref. 27 with permission of Royal Society of Chemistry)

13

Gardner *et al.* used two liquid single source precursors, $[(R_3P)_2CuIn(SR')_4]$ (R = n-Bu, R' = Et, Pr), to from monodispersed chalcopyrite $CuInS_2$ nanoparticles through a decomposition method. They mentioned that the single source precursor provided a clean route to form ternary materials.[90] Shapiro and her colleagues explored the photochemical decomposition of different single source precursors and successfully prepared $CuInS_2$ nanoclusters by using ultraviolet (UV)-photolysis (shown in Fig. 1.6).[27]

1.5.3 Solvothermal Synthesis

Solvothermal synthesis is a method similar to hydrothermal synthesis, but involves organic solvents instead of water. Compared to other methods, solvothermal synthesis has several advantages. First, solvothermal conditions permit rapid convection in solution. The comparably mild environment offers conditions to form crystals with few lattice defects and it allows for the precise control over the size, shape distribution, and crystallinity of nanoparticles.[91] Second, the low boiling point of organic solvent involved can provide a higher reaction pressure when proceed at high temperatures, which will contribute to the procedure of crystallization. Third, because of the mild temperature, special structural features of precursors can be transferred to the products so that the morphology of products can be controlled. Solvents can also provide functional groups, which can further react with the precursors or the products to synthesize novel materials.[92, 93] Finally, for some reaction systems such as the one including toxic starting materials, solvothermal synthesis can reduce the releasing of harmful vapour during the reaction. The sealed system not only contributes to carry out "green chemistry", but also efficiently reduces the possibility of oxidation and contamination from atmosphere or oxygen, an important point for high-purity products.

As a result, in order to control the size as well as the shape of nanoparticles synthesized in this thesis, solvothermal method was probed as a convenient route for fabricating the $CuInS_2$, $AgInS_2$ and $CuInSe_2$ nanoparticles from single source precursors. Similar to the single source decomposition introduced, it is possible to utilize one-step solvothermal synthesis to grow nanoparticles directly through the single molecules of relative precursors acting as building blocks.

14

1.6 **Analytical Techniques**

The characterization techniques used in this thesis can be generally divided into two types. First, the techniques for probing the crystallinity, particle size and optical properties of the as-made materials are termed bulk characterization method. This category includes powder X-ray diffraction (PXRD), single crystal X-ray diffraction (XRD), solid-state nuclear magnetic resonance spectroscopy (SS-NMR), UV-vis solution absorption spectroscopy, solid-state diffuse reflectance spectroscopy, and emission spectroscopy. The second type of analytical techniques investigates the morphology of the surface or the structure of the materials including scanning electron microscopy (SEM), transmission electron microscopy (TEM), energy dispersive X-ray spectroscopy (EDX) and selected area electron diffraction (SAED).

1.6.1 Powder X-ray Diffraction (PXRD)

Powder X-ray diffraction is one of the primary techniques used for the determination of phase and crystallinity of semiconductor nanoparticles. By comparison against reference patterns from the Joint Committee on Powder Diffraction Standards (JCPDS), the basic structural information of materials such as cell parameters, orientation and crystallite size can be determined. The X-rays emitted from an evacuated tube can be scattered by the electrons of the atoms in different, but certain directions and a unique pattern can be obtained. According to the Bragg Law (Equation 1.2), derived by W.H. Bragg,[94] it can explain the relationship between the lattice planes of crystals and the reflected X-ray beams at certain angles of incidence. In the equation, **d** is the lattice spacing of certain crystal plane; θ is the diffraction angle; *n* is an integer and λ is the wavelength of the X-ray. Therefore, for a known X-ray wavelength (typically, elemental Cu or Co are used in XRD experiments), by measuring the diffraction angle, it is possible to determine the value of **d**, which yields the information of the lattice constant of the material examined.

$$n\lambda = 2d\sin\theta$$
<div align="right">Equation 1.2</div>

In the XRD patterns, nanocrystallite size can cause broadening of the diffraction peaks. Although P. Scherrer explored the relationship between crystallite size and X-ray line broadening, size measurement of nanoparticles using this method is usually difficult and imprecise.[95] In this thesis, when focusing on nanoparticles, PXRD is used to confirm the identity of the samples and for other information such as size, further characterization by electron microscopy is typically required.

1.6.2 Electron Microscopy

1.6.2.1 **Scanning Electron Microscopy (SEM)**

Scanning electron microscopy is one of the crucial electron microscopy methods for characterizing nanoparticles. By scanning with a high-energy electron beam, it can show the images of the surface morphology of the specimen. Under a voltage of 5-30 kV between cathode and anode, electrons generated from a field emission are accelerated and reach the surface of sample in a current of $10^{-10} \sim 10^{-12}$ A. The accelerated electrons carry significant amounts of kinetic energy, and this energy is dissipated as a variety of signals depending on the surface. By scanning over the surface, the morphology can be detected by a detection system.

1.6.2.2 **Energy Dispersive X-ray Spectroscopy (EDX)**

At the same time as obtaining SEM images, by using an energy dispersive X-ray detector, the elemental composition of samples can be determined. This is a semi-quantitative analysis based on the characteristic X-rays for different elements. Excited electrons are produced by inelastic collisions of the incident electrons with electrons in discrete orbitals of atoms in the sample. After the excited electrons returning to lower energy states, X-rays with a fixed wavelength will be generated. Thus, characteristic X-rays are produced for each element in a specimen and, through an EDX detector, the composition of samples can be determined. However, due to the incident electrons, the characteristic X-rays can only be generated from the larger sample area to obtain a relative precise result, as a result of which the resolution of EDX in SEM is much worse than that of SEM imaging.

16

1.6.2.3 **Transmission Electron Microscopy (TEM)**

The principle of transmission electron microscopy is similar to that of an optical microscope; however, it is based on an electron beam in place of light. TEM is capable of imaging at a higher resolution versus SEM images and enables examination of fine details of the surface. Since the tension of field emission in a conventional TEM system varies from 80 kV to 300 kV, such high tension can accelerate electrons greatly so that for the thin samples (< 200 nm), electrons of TEM can pass through the samples.[96] Unlike SEM, it can thus obtain information about the internal phase structures. High-resolution (HR) - TEM is one important mode of TEM that especially explores the phases of nanosized materials. HR-TEM can directly present the atomic structure of the sample and make it convenient to study properties of materials on the atomic scale. When the electrons pass through the sample with only one layer, the phase of electron waves is only modified by the potential field of the atoms in the specimen, from which the information of image plane can be obtained by measuring the interference. By comparison with distances in standard, the phase structures can be determined.

1.6.2.4 **Electron Diffraction**

Electron diffraction is usually characterized along with TEM. When incident electron beams illuminate along an axis of highly crystalline samples, periodical 2D diffraction spots will appear. Since the wavelength of the electrons is known, interplanar distances can be calculated and further information about crystal symmetry can be obtained. Consequently, electron diffraction represents a valuable tool in crystallography. But for polycrystalline samples with random crystal orientations, the diffraction patterns are not presenting as dots. Instead, diffraction spots distributed randomly and consists of diffused rings, which arise from the short range atomic ordering. Selected Area Electron Diffraction (SAED) is one type of electron diffraction. Lattice spacings are extracted from the electron diffraction pattern by applying Equation 1.3, which relates the spacing of a lattice plane, *d*, with the electron wavelength, *λ*, relative space distance, *r*, and camera length, *L*. Lattice spacings obtained in this manner are used to identify phase in nanoparticles.

$$r \times d = \lambda \times L$$
Equation 1.3

17

1.6.3 Optical Spectroscopy

1.6.3.1 **UV-Vis Absorbance Spectroscopy**

UV-Vis absorption spectroscopy refers to absorption spectroscopy or reflectance spectroscopy in the ultraviolet (UV), visible and near-infrared (NIR) spectral region. In this case, the transmitted light which does not interact with the sample can be detected, indicating which particular wavelength can be absorbed by the sample. It is vital to control the concentration of absorbing materials in the sample because the absorbance is proportional to the concentration and the absorbance intensity lower than 1 is more reliable. The absorption wavelength can be further used to obtain the band gap energy for nanosized semiconductor samples by using Kubelka-Munk Formula (Equation 1.4) and Tauc Relation (Equation 1.5), where A is absorbance, R is reflectance, α is the absorption

$$A = -lg(R)$$

Equation 1.4

$$F(R) = \frac{(1-R)^2}{2R} = \frac{\alpha}{S}$$

$$(\alpha h v)^2 = c\,(h v - E)$$

Equation 1.5

$$h v = hc/\lambda$$

Equation 1.6

coefficient, S is scattering coefficient (equal to 1 in our case), hv is the discrete photo energy which is related to wavelength by Equation 1.6 , c is a constant, and E is the band gap energy of the particles. By combining with and plotting the tangent line of curve $(\alpha h v)^2$ vs hv, and extrapolating it to the energy axis at $(\alpha h v)^2 = 0$, the band gap can be roughly estimated as shown in Fig. 1.7.
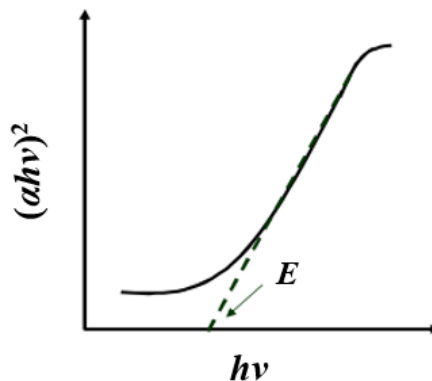

Fig. 1.7 Plot of $(\alpha h v)^2$ vs hv for measuring E (band gap of particles)

18

Furthermore, the obtained band gap energy can be used to calculate the particle size using the Brus Equation: $E = E_{gap} + \frac{h^2}{8r^2} \left(\frac{1}{m_{e*}} + \frac{1}{m_{h*}} \right)$ which was introduced as Equation 1.1 in Section 1.2.2. Since for all the parameters including E_{gap}, h, m_e* and m_h* are known for a specific material, the particle diameter r can be determined from the obtained band gap E directly.

1.6.3.2 Emission Spectroscopy

Unlike absorption spectroscopy which corresponds to the transitions from ground state to excited state, emission spectroscopy measures transitions from the excited state to the ground state. Specifically, high intensity light from an excitation source is directed at a nanoparticle suspension held in a quartz cuvette. The interaction between a single photon and a nanoparticle results in an electron being excited from the valence band into the conduction band. Subsequently, the electron and hole recombine, with a probability of emitting a photon at some point in the process dependent upon the emission quantum yield of the material. The intensity of emitted photons as a function of energy is also proportional to the concentration of sample and it is also related to the excitation wavelength. Thus, emission spectroscopy enables quantification of the spectral properties of excitation and emission. In order to record a good emission spectrum, the excitation monochromator is kept fixed at the desired excitation wavelength, and the emission monochromator swept over the desired spectral range. When recording excitation spectra, the emission monochromator is kept fixed and the excitation monochromator is swept. By comparing with a reference molecule such as rhodamine, the quantum yield of nanoparticles can be calculated from Equation 1.7.[97] F^i and F^s are the emission peak integration of the reference and sample, respectively; f_i and f_s mean the absorbance of the reference and the sample, respectively; n_i and n_s are the refractive indices of the reference and the sample, respectively; Φ_f^i and Φ_f^s are the quantum yields of the reference and sample, respectively.[98]

$$\Phi_f^s = \frac{F^s f_i n_s^2}{F^i f_s n_i^2} \Phi_f^i$$

Equation 1.7

1.7 Motivation of Study

To synthesize nanoscale semiconductor materials which can be fabricated in a large scale, the key focus is to find a synthetic method which should be low in cost, controllable in morphology and tunable in size.[99] From previous studies, the optical properties of semiconductors are known to be strongly size-dependent.[19, 20, 35, 100] In addition to tunable size, controlled phases and structures are also crucial to yield better conversion efficiency when fabricated in optical devices.[78] The aim for the work herein was to find a convenient and environmentally friendly route through which nanoparticles with controllable composition and size could be prepared.

Single source precursors are efficient to establish the desired nanoparticles from single molecules. This method has been explored by William *et al.*.[27] They applied a single source precursor, $(Ph_3P)_2Cu(SEt)_2In(SEt)_2$, in a photochemical decomposition route to form copper indium sulfide nanoclusters. When fabricating multinary semiconductors, the most challenging parameters are how to balance the ratio of composition and how to control the morphology. Thus, using single source precursors as the building blocks to fabricate nanoparticles can minimize the risk of incontrollable composition and structure. Solvothermal synthesis methods can take full advantage of temperature and pressure, simplifying the crystallization procedure. By performing reactions at relatively low temperatures, particles with small sizes can be obtained. Thus, the combination of these two methods will provide a convenient route to fabricate crystalline nanoparticles in tunable sizes and controllable structure in one step.

This thesis reports for the very first time, the use of solvothermal synthesis at low reactions temperatures to synthesize ternary nanoscale semiconductors with controlled sizes and structures from single source precursors. During the research, different solvothermal conditions were screened involving precursors with various ligand groups, additional chalcogen sources, reaction temperatures and times. Optimized conditions were determined for the preparation $CuInS_2$, $AgInS_2$ and $CuInSe_2$ nanoparticles.

References

1. J. Gale, J. C. Abanades, S. Bachu and C. Jenkins, *International Journal of Greenhouse Gas Control*, 2015, **40**, 1-5.

2. *Climate Change 2014: Synthesis Report. Contribution of Working Groups I, II and III to the Fifth Assessment Report of the Intergovernmental Panel on Climate Change*, IPCC, Switzerland, 2014.

3. *Key World Energy Statistic*, International Energy Agency, France, 2014.

4. O. Morton, *Nature*, 2006, **443**, 19-22.

5. E. Becquerel, *Compt. Rend.*, 1839, **9**, 561-562.

6. X. Z. Wu, *Sol. Energy*, 2004, **77**, 803-814.

7. G. Burns, *Solid State Physics*, Academic Press, Boston, 1995.

8. C. Kittel, *An Introduction to Solid State Physics*, John Wiley & Sons, 8th Edition, 2004.

9. W. J. Parak, L. Manna, F. C. Simmel, D. Gerion and P. Alivisatos, *Nanoparticles*, Wiley-VCH, 2004.

10. P. R. Sajanlal, T. S. Sreeprasad, A. K. Samal and T. Pradeep, *Nano Rev.*, 2011, **2**, 1-62.

11. Y. Wang and N. Herron, *J. Phys. Chem.*, 1991, **95**, 525-532.

12. H. Weller, *Angew. Chem. Int. Ed. Engl.*, 1993, **32**, 41-53.

13. U. Woggon, *Optical properties of semiconductor quantum dots*, Springer Berlin Heidelberg, 1997.

14. C. B. Murray, C. R. Kagan and M. G. Bawendi, *Annu. Rev. Mater. Sci.*, 2000, **30**, 545-610.

15. S. Sapra and D. D. Sarma, *The Chemistry of Nanomaterials: Synthesis, Properties and Applications*, Wiley-VCH:Weinheim, 2004.

16. M. L. Steigerwald and L. E. Brus, *Accounts. Chem. Res.*, 1990, **23**, 183-188.

17. A. P. Alivisatos, *J. Phys. Chem.*, 1996, **100**, 13226-13239.

18. M. R. Bockstaller, *Nanoparticles: From Theory to Nanoparticles*, John Wiley & Sons, 2005.

19. R. G. Xie, M. Rutherford and X. G. Peng, *J. Am. Chem. Soc.*, 2009, **131**, 5691-5697.

20. L. Li, A. Pandey, D. J. Werder, B. P. Khanal, J. M. Pietryga and V. I. Klimov, *J. Am. Chem. Soc.*, 2011, **133**, 1176-1179.

21. H. Zhang, M. S. Jin, J. G. Wang, M. J. Kim, D. R. Yang and Y. N. Xia, *J. Am. Chem. Soc.*, 2011, **133**, 10422-10425.

22. S. T. Connor, C. M. Hsu, B. D. Weil, S. Aloni and Y. Cui, *J. Am. Chem. Soc.*, 2009, **131**, 4962-4966.

23. A. T. Fafarman, W. K. Koh, B. T. Diroll, D. K. Kim, D. K. Ko, S. J. Oh, X. C. Ye, V. Doan-Nguyen, M. R. Crump, D. C. Reifsnyder, C. B. Murray and C. R. Kagan, *J. Am. Chem. Soc.*, 2011, **133**, 15753-15761.

24. G. S. H. Lee, D. C. Craig, I. Ma, M. L. Scudder, T. D. Bailey and I. G. Dance, *J. Am. Chem. Soc.*, 1988, **110**, 4863-4864.

25. A. Eichhoefer and D. Fenske, *J. Chem. Soc. Dalton. Trans.*, 2000, **6**, 941-944.

26. R. Ahlrichs, N. R. M. Crawford, A. Eichhoefer, D. Fenske, O. Hampe, M. M. Kappes and J. Olkowska-Oetzel, *Eur. J. Inorg. Chem.*, 2006, **2**, 345-350.

27. M. Williams, R. M. Okasha, J. Nairn, B. Twamley, T. H. Afifi and P. J. Shapiro, *Chem. Commun.*, 2007, **30**, 3177-3179.

28. N. F. Zheng, X. H. Bu, J. Lauda and P. Y. Feng, *Chem. Mater.*, 2006, **18**, 4307-4311.

29. H. Morkoç and Ü. Özgür, *Zinc Oxide: Fundamentals, Materials and Device Technology*, Wiley-VCH, 2009.

30. M. Kruszynska, H. Borchert, J. Parisi and J. Kolny-Olesiak, *J. Nanopart. Res.*, 2011, **13**, 5815-5824.

31. I. Kriegel, C. Y. Jiang, J. Rodriguez-Fernandez, R. D. Schaller, D. V. Talapin, E. da Como and J. Feldmann, *J. Am. Chem. Soc.*, 2012, **134**, 1583-1590.

32. M. P. Suryawanshi, G. L. Agawane, S. M. Bhosale, S. W. Shin, P. S. Patil, J. H. Kim and A. V. Moholkar, *Mater. Technol.*, 2013, **28**, 98-109.

33. L. Krusin-Elbaum, D. M. Newns, H. Zeng, V. Derycke, J. Z. Sun and R. Sandstrom, *Nature*, 2004, **431**, 672-676.

34. J. Chang, *Controlled Synthesis of Inorganic Semiconductor Nanocrystals and Their Applications*, Doctoral dissertation, Queensland University of Technology, 2013.

35.   H. Z. Zhong, Z. L. Bai and B. S. Zou, *J. Phys. Chem. Lett.*, 2012, **3**, 3167-3175.

36.   T. Saga, *NPG Asia Mater.*, 2010, **2**, 96-102.

37.   N. V. Soloviev, A. Eichhofer, D. Fenske and U. Banin, *J. Am. Chem. Soc.*, 2001, **123**, 2354-2364.

38.   A. Nag, M. V. Kovalenko, J. S. Lee, W. Y. Liu, B. Spokoyny and D. V. Talapin, *J. Am. Chem. Soc.*, 2011, **133**, 10612-10620.

39.   E. Wahlstrom, E. K. Vestergaard, R. Schaub, A. Ronnau, M. Vestergaard, E. Laegsgaard, I. Stensgaard and F. Besenbacher, *Science*, 2004, **303**, 511-513.

40.   J. Dvorak, T. Jirsak and J. A. Rodriguez, *Surf. Sci.*, 2001, **479**, 155-168.

41.   J. Tang, K. W. Kemp, S. Hoogland, K. S. Jeong, H. Liu, L. Levina, M. Furukawa, X. H. Wang, R. Debnath, D. K. Cha, K. W. Chou, A. Fischer, A. Amassian, J. B. Asbury and E. H. Sargent, *Nature Mater.*, 2011, **10**, 765-771.

42.   Z. A. Peng and X. G. Peng, *J. Am. Chem. Soc.*, 2001, **123**, 1389-1395.

43.   W. W. Yu and X. G. Peng, *Angew. Chem. Int. Ed.*, 2002, **41**, 2368-2371.

44.   W. W. Yu, L. H. Qu, W. Z. Guo and X. G. Peng, *Chem. Mater.*, 2003, **15**, 2854-2860.

45.   A. Zunger, *Int. J. Quantum Chem.*, 1985, **28**, 629-653.

46.   C. Ferekides and J. Britt, *7th International Photovoltaic Science and Engineering Conference, Technical Digest*, 1993, 509-511.

47.   C. B. Murray, D. J. Norris and M. G. Bawendi, *J. Am. Chem. Soc.*, 1993, **115**, 8706-8715.

48.   J. Q. Peng, L. Lu and H. X. Yang, *Renew. Sust. Energ. Rev*, 2013, **19**, 255-274.

49.   K. J. Choi and H. W. Jang, *Sensors*, 2010, **10**, 4083-4099.

50.   A. Forleo, L. Francioso, S. Capone, P. Siciliano, P. Lommens and Z. Hens, *Sensor Actuat. B-chem*, 2010, **146**, 111-115.

51.   J. A. Anta, E. Guillen and R. Tena-Zaera, *J. Phys. Chem. C*, 2012, **116**, 11413-11425.

52.   T. Inoue, A. Fujishima, S. Konishi and K. Honda, *Nature*, 1979, **277**, 637-638.

53.   F. Y. Shen, W. X. Que, Y. C. He, Y. Yuan, X. T. Yin and G. F. Wang, *Acs Appl. Mater. Interfaces*, 2012, **4**, 4087-4092.

54. W. E. Devaney, W. S. Chen, J. M. Stewart and R. A. Mickelsen, *Ieee. T. Electron Dev.*, 1990, **37**, 428-433.

55. A. Miller, A. Mackinnon and D. Weaire, *Solid State Phys.*, 1981, **36**, 119-175.

56. M. G. Panthani, V. Akhavan, B. Goodfellow, J. P. Schmidtke, L. Dunn, A. Dodabalapur, P. F. Barbara and B. A. Korgel, *J. Am. Chem. Soc.*, 2008, **130**, 16770-16777.

57. N. C. Greenham, X. G. Peng and A. P. Alivisatos, *Phys. Rev. B*, 1996, **54**, 17628-17637.

58. D. Scheunemann, S. Wilken, J. Parisi and H. Borchert, *Appl. Phys. Lett.*, 2013, **103**, 133902-133906.

59. D. L. Schulz, C. J. Curtis, R. A. Flitton, H. Wiesner, J. Keane, R. J. Matson, K. M. Jones, P. A. Parilla, R. Noufi and D. S. Ginley, *J. Electron. Mater.*, 1998, **27**, 433-437.

60. R. Kamada, W. N. Shafarman and R. W. Birkmire, *Sol. Energ. Mater. Sol. C.*, 2010, **94**, 451-456.

61. R. Po, C. Carbonera, A. Bernardi and N. Camaioni, *Energy & Environmental Science*, 2011, **4**, 285-310.

62. A. Romeo, A. Terheggen, D. Abou-Ras, D. L. Batzner, F. J. Haug, M. Kalin, D. Rudmann and A. N. Tiwari, *Prog. Photovoltaics*, 2004, **12**, 93-111.

63. W. J. Yue, S. K. Han, R. X. Peng, W. Shen, H. W. Geng, F. Wu, S. W. Tao and M. T. Wang, *J. Mater. Chem.*, 2010, **20**, 7570-7578.

64. B. Tell, J. L. Shay and H. M. Kasper, *Phys. Rev. B*, 1971, **4**, 2463-2471.

65. H. Hahn, *Angew. Chem.*, 1953, **65**, 538-538.

66. H. Neumann and R. D. Tomlinson, *Solid State Commun.*, 1986, **57**, 591-594.

67. K. Ramanathan, M. A. Contreras, C. L. Perkins, S. Asher, F. S. Hasoon, J. Keane, D. Young, M. Romero, W. Metzger, R. Noufi, J. Ward and A. Duda, *Prog. Photovoltaics*, 2003, **11**, 225-230.

68. J. L. Shay and B. Tell, *Surf. Sci.*, 1973, **37**, 748-762.

69. Y. Akaki, K. Yamashita, T. Yoshitake, S. Nakamura, S. Seto, T. Tokuda and K. Yoshino, *Physica B Condens. Matter*, 2012, **407**, 2858-2860.

70. X. S. Tang, W. B. A. Ho and J. M. Xue, *J. Phys. Chem. C*, 2012, **116**, 9769-9773.

71. J. H. Jung, J. H. Kim, T. W. Kim, M. S. Song, Y. H. Kim and S. Jin, *Appl. Phys. Lett.*, 2006, **89**, 122110-122113.

72. M. Q. Zhu, L. Y. Zhu, J. J. Han, W. W. Wu, J. K. Hurst and A. D. Q. Li, *J. Am. Chem. Soc.*, 2006, **128**, 4303-4309.

73. I. I. Slowing, B. G. Trewyn, S. Giri and V. S. Y. Lin, *Adv. Funct. Mater.*, 2007, **17**, 1225-1236.

74. X. Y. Xing, K. B. Zheng, H. H. Xu, F. Fang, H. T. Shen, J. Zhang, J. Zhu, C. N. Ye, G. Y. Cao, D. L. Sun and G. R. Chen, *Micron*, 2006, **37**, 370-373.

75. G. Jimenez-Cadena, E. Comini, M. Ferroni, A. Vomiero and G. Sberveglieri, *Mater. Chem. Phys.*, 2010, **124**, 694-698.

76. Y. Jouane, S. Colis, G. Schmerber, P. Kern, A. Dinia, T. Heiser and Y. A. Chapuis, *J. Mater. Chem.*, 2011, **21**, 1953-1958.

77. U. Pal, J. G. Serrano, N. Koshizaki and T. Sasaki, *Mat. Sci. Eng. B-Solid*, 2004, **113**, 24-29.

78. S. L. Castro, S. G. Bailey, R. P. Raffaelle, K. K. Banger and A. F. Hepp, *Chem. Mater.*, 2003, **15**, 3142-3147.

79. P. Dutta, A. Manivannan, M. S. Seehra, N. Shah and G. P. Huffman, *J. Appl. Phys.*, 2006, **99**, 122110-122113.

80. Z. Q. Yang, W. W. Chen, Z. Q. Zu, Z. G. Zang, Y. C. Yang and X. S. Tang, *Mater. Lett.*, 2015, **151**, 89-92.

81. Y. Jiang, Y. Wu, X. Mo, W. C. Yu, Y. Xie and Y. T. Qian, *Inorg. Chem.*, 2000, **39**, 2964-2965.

82. J. P. Xiao, Y. Xie, R. Tang and Y. T. Qian, *J. Solid State Chem.*, 2001, **161**, 179-183.

83. Q. Li, L. L. Zhai, C. Zou, X. S. Huang, L. J. Zhang, Y. Yang, X. Chen and S. M. Huang, *Nanoscale*, 2013, **5**, 1638-1648.

84. W. M. Du, X. F. Qian, J. Yin and Q. Gong, *Chem. Eur. J.*, 2007, **13**, 8840-8846.

85. F. Long, W. M. Wang, H. C. Tao, T. K. Jia, X. M. Li, Z. G. Zou and Z. Y. Fu, *Mater. Lett.*, 2010, **64**, 195-198.

86. J. S. Gardner, E. Shurdha, C. M. Wang, L. D. Lau, R. G. Rodriguez and J. J. Pak, *J. Nanopart. Res.*, 2008, **10**, 633-641.

87. M. Capka, *Chem. Listy*, 1973, **67**, 1104-1108.

25

88.   T. T. Tidwell, *Angew. Chem. Int. Ed.*, 2001, **40**, 331-337.

89.   D. C. Pan, L. J. An, Z. M. Sun, W. Hou, Y. Yang, Z. Z. Yang and Y. F. Lu, *J. Am. Chem. Soc.*, 2008, **130**, 5620-5621.

90.   K. K. Banger, J. Cowen and A. F. Hepp, *Chem. Mater.*, 2001, **13**, 3827-3828.

91.   R. I. Walton, *Chem. Soc. Rev.*, 2002, **31**, 230-238.

92.   D. Gatteschi and R. Sessoli, *Angew. Chem.* , 2003, **115**, 278-309.

93.   M. Zeng, H. Liang, W. X. Zhang, X. M. and B. D. Chen, *Angew. Chem.*, 2007, **119**, 1864-1867.

94.   W. H. Bragg and W. L. Bragg, *Proc R. Soc. Lond. A*, 1913, **88** 428-438.

95.   A. L. Patterson, *Phys. Rev.*, 1939, **56**, 978-982.

96.   D. B. Williams and C. Barry Carter, *Transmission electron microscopy: a textbook for materials science*, Spinger New York, 2009.

97.   M. Grabolle, M. Spieles, V. Lesnyak, N. Gaponik, A. Eychmuller and U. Resch-Genger, *Anal. Chem.*, 2009, **81**, 6285-6294.

98.   A. M. Brouwer, *Pure Appl. Chem.*, 2011, **83**, 2213-2228.

99.   E. H. Sargent, *Nat*. *Photonics.*, 2009, **3**, 325-331.

100.   W. S. Song and H. Yang, *Chem. Mater.*, 2012, **24**, 1961-1967.

CHAPTER 2. Wurtzite CuInS₂ Nanoparticles

2.1 Introduction

From the first studies of quantum dot solar cell devices, the materials most heavily explored as the absorber layers have been silicon nanocrystals, TiO_2, ZnO and cadmium chalcogenides (CdS and CdSe). As mentioned in Chapter 1, although some of these materials have already been commercialized, they have disadvantages that cannot be ignored. Nanocrystalline silicon is an indirect band gap semiconductor; TiO_2 and ZnO have very large band gap energy and cadmium chalcogenides (CdS and CdSe) as well as PbS present a health concern.[1] With this in mind, $CuInS_2$ is believed to be a viable replacement material, especially for industrial-scale manufacture.[2]

$CuInS_2$ has a direct band gap, which results in a high molar absorptivity of about 5.0×10^5 cm^{-1},[3] meaning the material can take full advantage of incident photons.[3, 4] The band gap energy of bulk chalcopyrite $CuInS_2$ is 1.53 eV,[5] which corresponds to a minimum wavelength of light of ~810 nm for exciton pair generation. This means that $CuInS_2$ will form an exciton pair under exposure to visible light, and will thus match the solar spectrum and is efficient in utilizing the broadband visible light emission of sunlight. Furthermore, because of the high efficiency, when fabricating the $CuInS_2$ only a thin light-absorbing layer is required to satisfy the requirements in a photovoltaic device, unlike when traditional materials such as silicon are used. Large and pristine crystals of $CuInS_2$ are not needed for this process, and this could decrease the expense of production as well as simplify the procedure of fabrication significantly. Additionally, $CuInS_2$ does not contain any highly toxic elements, and the component elements are relatively more abundant.[6] Finally, compared to cadmium chalcogenides, $CuInS_2$ exhibits improved photo-stability and thermal stability with a decomposition temperature above 845 K.[7]

Among the different morphologies of $CuInS_2$ materials, nanoparticles or quantum dots are of most interest for alternative energy applications. Bulk $CuInS_2$ or thin films have been studied for some time and explored for the use in photovoltaic devices,[4, 8] but recently much attention has shifted towards nanoscale materials.[2, 9] Because $CuInS_2$ synthesized at

the nanoscale is relatively new, there is a lack of the comprehensive understanding and development associated with the other, more established materials such as CdS.

$CuInS_2$ is the ternary derivative of the binary ZnS material; thus like the crystal structures of ZnS, it has cubic and hexagonal polymorphs.[10] By substituting copper and indium into the cation positions that would be filled by zinc in ZnS, the structures may exhibit three different types of structural polymorphs.[11] A stable phase with a tetragonal chalcopyrite structure was first synthesized by Hahn *et al.*[12] and exists from room temperature to 1253K, as shown in Fig. 2.1 (a). A cubic zinc-blende structure can be found from 1253 K to 1318 K as a metastable phase (Fig. 2.1 (b)) and is synthesized more commonly,[10] $CuInS_2$ assumes a hexagonal wurtzite structure from 1318 K up to the melting point of 1383 K, as shown in Fig 2.1 (c); this was first reported by Lu *et al.* in 2008.[13] Recently, Zhou *et al.* synthesized a new type of $CuInS_2$ crystal with a spinel structure (Fig. 2.1 (d)), and they also successfully synthesized $CuInS_2$ with wurtzite and zinc blende structures by using different reaction conditions in a similar synthesis route.[14]
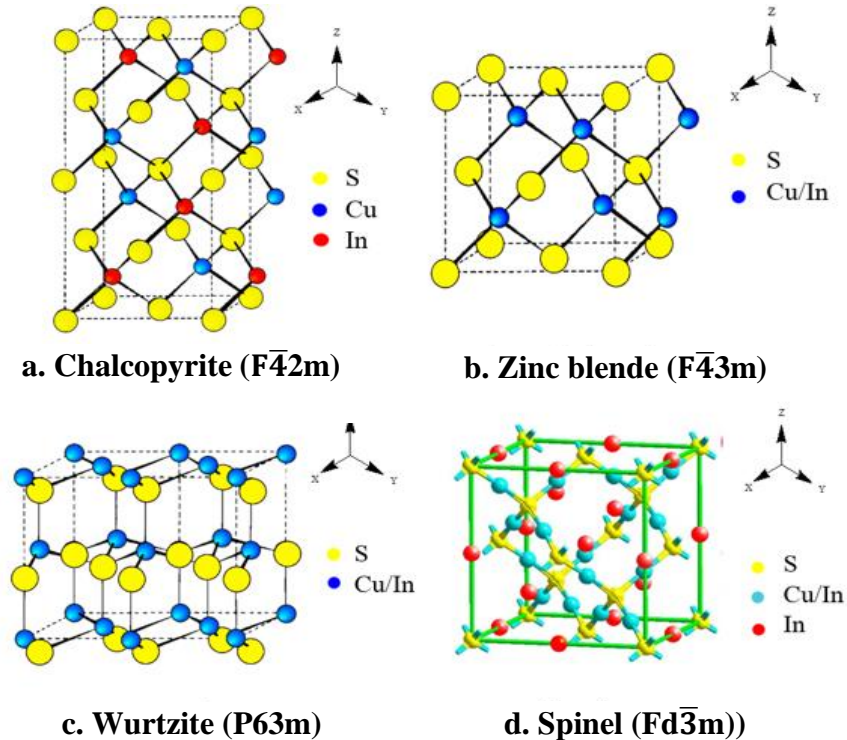

a. Chalcopyrite ($F\bar{4}2m$)   **b. Zinc blende ($F\bar{4}3m$)**

c. Wurtzite (P63m)   **d. Spinel ($Fd\bar{3}m$))**

Fig. 2.1 Different structures of $CuInS_2$ crystals
(d: reproduced with permission from ref. 14.
Copyright © 2013 American Chemical Society)

28

Although the zinc blende structure of $CuInS_2$ is tetragonal, and the chalcopyrite structure is nearly cubic, these two structures are largely identical and only differentiated by how the cations (Cu^+ and In^{3+}) are positioned in the structure.[10] In the chalcopyrite phase, the Cu and In atoms are ordered in the cation lattice sites, and this is the predominant phase of bulk material at room temperature. In contrast, the zinc blende and wurtzite modifications are much more stable at higher temperatures or in the nanoscale, with the Cu and In atoms being randomly distributed over the cation sites of the lattice.[15]

To date, $CuInS_2$ nanoparticles with the chalcopyrite structure have been the most explored. A large number of synthetic routes and various applications have been published for synthesizing quantum-confined chalcopyrite nanoparticles with tunable sizes and shapes.[16] However, chalcopyrite $CuInS_2$ does not exhibit the most desirable properties of these four different morphologies.[17]

From previous research, it is known that by increasing the density of copper vacancies in the crystals, quantum yields of emission can be raised up to 90 %.[18-20] This offers a route to enhance quantum yields in wurtzite $CuInS_2$, since the wurtzite structure is known to contain a random distribution of Cu and In atoms. This distribution of Cu and In should result in more copper vacancies compared to the chalcopyrite and zinc blende structure. In addition, wurtzite $CuInS_2$ possesses almost all of the desirable properties of the chalcopyrite structure, and its calculated band gap is 1.48 eV, 0.05 eV lower than that of chalcopyrite.[21] It also possesses a flexible stoichiometry and a wider range for tuning the Fermi energy, which is an essential requirement for nano-device fabrication.[22] The anisotropic structure of wurtzite $CuInS_2$ permits fabrication of asymmetric nanostructures, such as nanorods or nanowires.[23] Such an asymmetric structure could find applications as an antennae for absorbing light and performing conduction through orthogonal charge carriers. As a result, wurtzite $CuInS_2$ is a particularly desirable material for photovoltaic and photocatalytic applications.

In a similar manner to chalcopyrite $CuInS_2$ nanoparticles, nanosized wurtzite $CuInS_2$ also shows a significant Stokes shift in photoluminescence to a lower energy region.[17] It is hypothesized that development of nanoparticles of uniform size should

29

improve the optical efficiency of the material dramatically and reduce their Stokes shift. However, the drawback of this wurtzite material is the lack of a known synthesis that provides size control. Hence, the second goal of this study is to find a simplified route to form size-controlled $CuInS_2$ nanoparticles. This chapter will illustrate a feasible method for fabricating wurtzite $CuInS_2$ nanoparticles in a controlled size and phase by using single source precursors as building blocks and solvothermal methods.

2.2 Experimental Descriptions

2.2.1 Materials

Sodium methoxide, tert-butylthiol, ethanethiol, thiophenol, indium (III) chloride, copper (I) chloride, thiourea and sulfur powder were purchased from Aldrich or VWR and used as received. Triphenylphosphine was purchased from Sigma and vacuum dried for 4 hours at room temperature, then stored under inert atmosphere. Solvents such as toluene, tetrahydrofuran (THF) and hexane were dried by passage through packed columns of activated alumina using a commercially available MBraun MB-SP Series solvent purification system. Methanol and CH_2Cl_2 were distilled and dried over CaH_2 and P_2O_5, respectively. Solvents such as dimethylformamide (DMF) and acetonitrile were degassed under N_2 flow for 30 minutes and stored under inert atmosphere conditions. The solvent for ^{1}H NMR spectroscopy was chloroform-d, which was purchased from Aldrich and distilled over P_2O_5.

All synthetic and handling procedures were carried out under an atmosphere of high purity dried nitrogen using standard double manifold Schlenk line techniques and an MBraun Labmaster 130 glovebox. For the solvothermal synthesis, stainless steel autoclaves and disposable glass bottles (30 mL) with Teflon caps were used.

2.2.2 Syntheses

2.2.2.1 Synthesis of [(Ph₃P)₂CuIn(SPh)₄] 1

[(Ph₃P)₂CuIn(SPh)₄] **1** was synthesized by slight modification of the published procedure:[24] NaSPh was prepared by adding phenylthiol (0.48 mL) into a methanol solution (15 mL) of NaOCH₃ (0.242 g, 4.48 mmol) and stirring for 30 min. InCl₃ (0.230 g,

30

1.04 mmol) dissolved in 5 mL of methanol was added, stirring for another 1.5 hours to form $Na[In(SPh)_4]$. PPh_3 (0.574 g, 2.19 mmol) and CuCl (0.114 g, 1.15 mmol) were then combined in 15 ml of CH_2Cl_2 and the mixture was added dropwise to $Na[In(SPh)_4]$. The reaction mixture was stirred overnight, affording a slight yellow solution with a pale yellow precipitate. The solvent volume was reduced under vacuum to half and 20 mL of methanol was added to fully precipitate the product rather than NaCl (by-product). The pale yellow precipitate was collected by filtration and washed with methanol twice, then the solid was dried for 2 h, affording **1** as a pale yellow solid. Yield, 0.87g, 74 %; ^{1}H NMR (400 MHz; $CDCl_3$, 23 °C): δ 6.88 (s, 5H); δ 7.13 (d, J = 7.4 Hz, 4H); δ 7.22 (br d, J = 6.6 Hz, 10H), δ 7.37 (m, 3H); ^{31}P NMR $CDCl_3$; δ -1.4. The data match those from a previous published report.[24]

2.2.2.2 **Synthesis of $[(Ph_3P)_2CuIn(SR)_4]$ (2, R= ^tBu ; 3, R=Et)**

$[(Ph_3P)_2CuIn(SR)_4]$ (**2,** R=^tBu; **3**, R= Et) was synthesized in a similar method as described for $[(Ph_3P)_2CuIn(SPh)_4]$. A white precipitate was collected and redissolved in 20 mL CH_2Cl_2 and filtered through Celite™ to remove residual NaCl. The solvent was removed under vacuum, affording either $[(Ph_3P)_2CuIn(S^tBu)_4]$ **2** and $[(Ph_3P)_2CuIn(SEt)_4]$ **3** as a white solid. For **2**, yield, 0.45g, 42 %; ^{1}H NMR (400 MHz; $CDCl_3$, 23 °C): δ 7.42-7.35 (br m, 30H, $P(C_6H_5)_3$); δ 1.47 (s, 36H, $SC(CH_3)_3$); ^{13}C NMR (100.5Hz, $CDCl_3$): δ 134.7 (d, J = 17 Hz, $P(C_6H_5)_3$), 130.4 (s, $P(C_6H_5)_3$), 129.5(d, J = 8.5 Hz, $P(C_6H_5)_3$), 47.6 (s, $SC(CH_3)_3$); ^{31}P NMR $CDCl_3$; δ -1.9. For **3**, yield, 0.63g, 66 %; ^{1}H NMR (400 MHz; $CDCl_3$, 23 °C);   δ 1.24 (t, J = 7.4 Hz, 12H, CH_3); δ 2.67 (q, J = 7.4 Hz, 8H, SCH_2); δ 7.33 (m, 30H, $P(C_6H_5)_3$); ^{31}P NMR $CDCl_3$; δ -4.4. The NMR data match the published data.[24]

2.2.2.3 **Synthesis of $[(CuInS_2)_x]$ nanoparticles**

Syntheses were performed in a sealed reactor at a controlled temperature and increased pressure using polar organic solvents (solvothermal conditions). A typical procedure for the preparation of $[(CuInS_2)_x]$ nanoparticles was as follows: an appropriate amount of precursor (0.1 ~ 0.2 mmol) was combined with a solvent (typically THF, 10-15 mL) in a 30 mL glass bottle with Teflon cap. For some samples, a sulfur source (4 ~ 8 mg thiourea or S_8) was added and mixed thoroughly for about 15 min until a clear solution was

31

obtained. The bottle was sealed in a stainless steel autoclave and heated in an oven for a various time at a selected temperature. The autoclave was cooled to room temperature naturally. The solid material was collected by centrifugation at 4000 rpm for 15 min, washed several times by the solvent used for the reaction and finally by methanol, and dried under vacuum for 4-6 h.

2.2.3 Characterization

Nuclear magnetic resonance (NMR) spectroscopy. Solution NMR spectra were obtained on a Varian Mercury 400 spectrometer using standard settings. ^{1}H and ^{13}C{^{1}H} NMR spectra were referenced internally to SiMe$_4$ using the residual proton and carbon signal of deuterated solvents at operating frequencies of 400.08 and 100.61 MHz. ^{31}P chemical shifts are referenced to 85% H$_3$PO$_4$.

Powder X-ray Diffraction (PXRD). PXRD patterns were obtained using a Rigaku diffractometer with a Co Kα radiation source (λ = 1.79926 Å). The samples were placed on a standard glass holder and measured with sampling interval 0.02 ° and scan speed 10 ° /min with the 2θ values ranging from 2 ° to 82 °.

Optical Measurements. UV-Vis absorption spectra of suspensions of samples were acquired using a Varian Cary 300 BioUV-Vis spectrometer at 25 ℃ in 1.00 cm quartz cells. Spectra of the pure solvent were subtracted. Photoluminescence (PL) spectra were taken from a PTI QuantaMaster™ 300 fluorimeter. Fluorescence quantum yields were estimated by the comparison of the fluorescence intensity with standard dye solutions with the same optical intensity at the excitation wavelength and similar fluorescence wavelength.[25]

Scanning Electron Microscopy (SEM). SEM images were obtained by using a LEO (Zeiss) 1540XB FIB/SEM instrument with a field emission gun of 3 kV, and measured by Dr. Tim Goldhawk.

Energy-Dispersive Spectroscopy (EDS). For elemental analysis, the same SEM instrument was used, but with a field emission gun operated at 10 kV.

Transmission Electron Microscopy (TEM) and High-Resolution TEM (HR-TEM). The low-resolution TEM images were obtained from a Philips CM10 transmission microscope with an acceleration voltage of 100 kV. Carbon-coated copper grids were dipped in isopropanol to deposit nanoparticles onto the film. HR-TEM images were taken on a JEOL 2010F TEM/STEM instrument with an acceleration voltage of 200 kV. Selected Area Diffraction (SAD) patterns were also obtained along with HR-TEM measurements.

Thermal Gravimetric Analysis (TGA). TGA analysis were performed on a TA SDT Q600 device. The heating rate was controlled at a rate of 10 ℃ / min between 20-600 ℃ under the nitrogen flow.

2.3 **Results and Discussion**

Three precursors $[(Ph_3P)_2CuIn(SR)_4]$ (**1**, R = Ph; **2**, R = ^tBu; **3**, R = Et) were investigated for conversion to $[(CuInS_2)_x]$ nanoparticles by varying several reaction parameters. Due to the different bond enthalpies between sulfur and the R groups ($\Delta H_{f\,(S-^tBu)}$ = 69 kcal/mol; $\Delta H_{f\,(S-ET)}$ = 72 kcal/mol; $\Delta H_{f\,(S-Ph)}$ = 87 kcal/mol),[26] different precursors are associated with different particle sizes, although their structures are similar (line structures are shown in Fig. 2.2). The thermal decomposition of **1**, **2**, **3** and subsequent growth of CuInS$_2$ nanoparticles have been studied previously,[22, 27, 28] however, the formation of nanosized copper indium sulfide materials under solvothermal conditions has not been systematically explored.
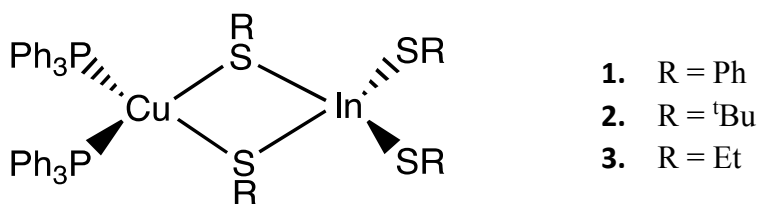
Fig. 2.2 The structures of precursors 1, 2 and 3.

To probe the chemical reactions of different precursors under solvothermal conditions, the process was investigated using ^{1}H NMR spectroscopy by monitoring the presence and disappearance of signals associated with the $[(Ph_3P)_2CuIn(SR)_4]$ precursors. By changing the reaction conditions, the optimized syntheses of these small monodispersed

33

nanomaterials were determined. Additionally, as introduced previously, "colour" is a valid guide to investigate the size of particles when synthesizing semiconductor nanomaterials, so it is also possible to select the optimized synthetic conditions by examining the colours of the reaction products.

2.3.1 Variations in conversion from [(Ph₃P)₂CuIn(SPh)₄] **1** to [(CuInS₂)ₓ]

2.3.1.1 **Temperature**

Precursor [(Ph₃P)₂CuIn(SPh)₄] **1** was examined first and reactions were performed in THF at different temperatures of 100 ℃, 140 ℃ and 170 ℃ respectively. After 24 h, the reactions under each temperature setting generated similar products. Two species of products were observed; a yellow precipitate surrounded by colourless crystals. Acetone, hexane and methanol were used in attempts to separate the two species due to their different solubilities, but large amount of colourless needles were still mixed in with the yellow precipitate after washing (10 X). By removing the colourless crystals manually, the PXRD patterns of products under 140 ℃ (Sample 1-1A) before and after separation were obtained (as shown in Fig. 2.3).
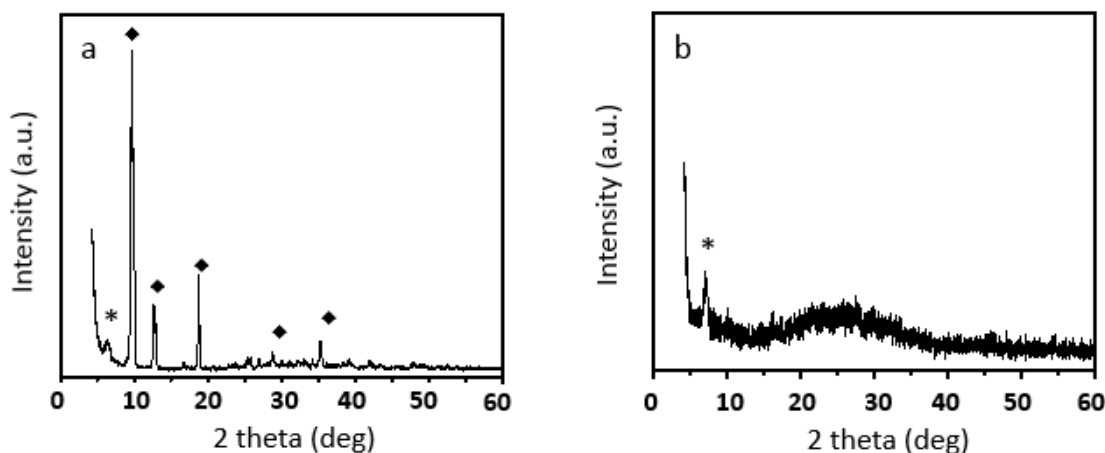
Fig. 2.3 PXRD patterns of sample 1-1A before (a) and after (b) separation
(symbol * : the phase from yellow precipitate;
symbol ♦: the phase from colourless crystals)

34

As shown in Fig. 2.3 (a), several sharp peaks (shown as ♦) present in the PXRD pattern before separation were found to correspond to the colourless crystalline material. An additional low angle peak (marked with *) indicates the formation of a layered structure, which likely corresponds to the yellow precipitate. This is confirmed by the pattern obtained after removing the colourless crystals manually; only the low angle peak (Fig. 2.3 (b)) was left. Additionally, there is a broad peak located at 2θ values ranging from 16 °to 38 °, which might result from nanosized materials since broadening is expected due the random orientations of small particles. There was no perfect match of structure to the PXRD pattern of colourless crystals in Fig. 2.3 (a), and it is difficult to obtain impurity-free products efficiently at large scales. Additionally, no tunable colour (size control) could be achieved by changing the reaction temperature. Thus, precursor $[(Ph_3P)_2CuIn(SPh)_4]$ **1** was not used for further research.

2.3.2 Variations in conversion of $[(Ph_3P)_2CuIn(S^tBu)_4]$ **2** to $[(CuInS_2)_x]$

2.3.2.1 **Temperature**

The conversion of $[(Ph_3P)_2CuIn(S^tBu)_4]$ **2** proceeds from a low temperature (80 °C). When reaction temperatures were changed between 80 °C and 120 °C (Table 2.1), the resultant solutions varied from colourless to brown without any noticeable precipitate. At a temperature of 160 °C (sample 1-2D), a red brown precipitate synthesized and a black

Table 2.1 Temperature and sulfur source variations for precursor 2

Sample	T/°C	Additional Sulfur Source	Solution	Precipitate	Colour
1-2A	80	-	✓		colourless
1-2B	100	-	✓		slight brown
1-2C	120	-	✓		brown
1-2D	160	-		✓	red brown
1-2E	180	-		✓	black
1-2F	140	thiourea		✓	black (film)
1-2G	120	S_8		✓	white
1-2H	140	S_8		✓	brown

35

precipitate was observed for reaction temperatures of 180 ℃ (sample 1-2E). UV-Vis absorption spectroscopy was used to monitor any changes of species in the reaction solution, but no clear absorption maximum was obtained. Powder X-ray diffraction patterns were measured to probe the structure of the solids obtained from different reactions.

As shown in Fig. 2.4 (a), it is clear that the product obtained at a higher temperature (sample 1-2E) results in sharper peaks with higher intensity in PXRD patterns, which are in accordance with the previously reported wurtzite $CuInS_2$ (ICCD 01-077-9459). There are also several additional peaks for sample 1-2E, which are labelled as • (shown in Fig. 2.4 (a)). These peaks match with the PXRD patterns of Cu_2S as an impurity formed in the
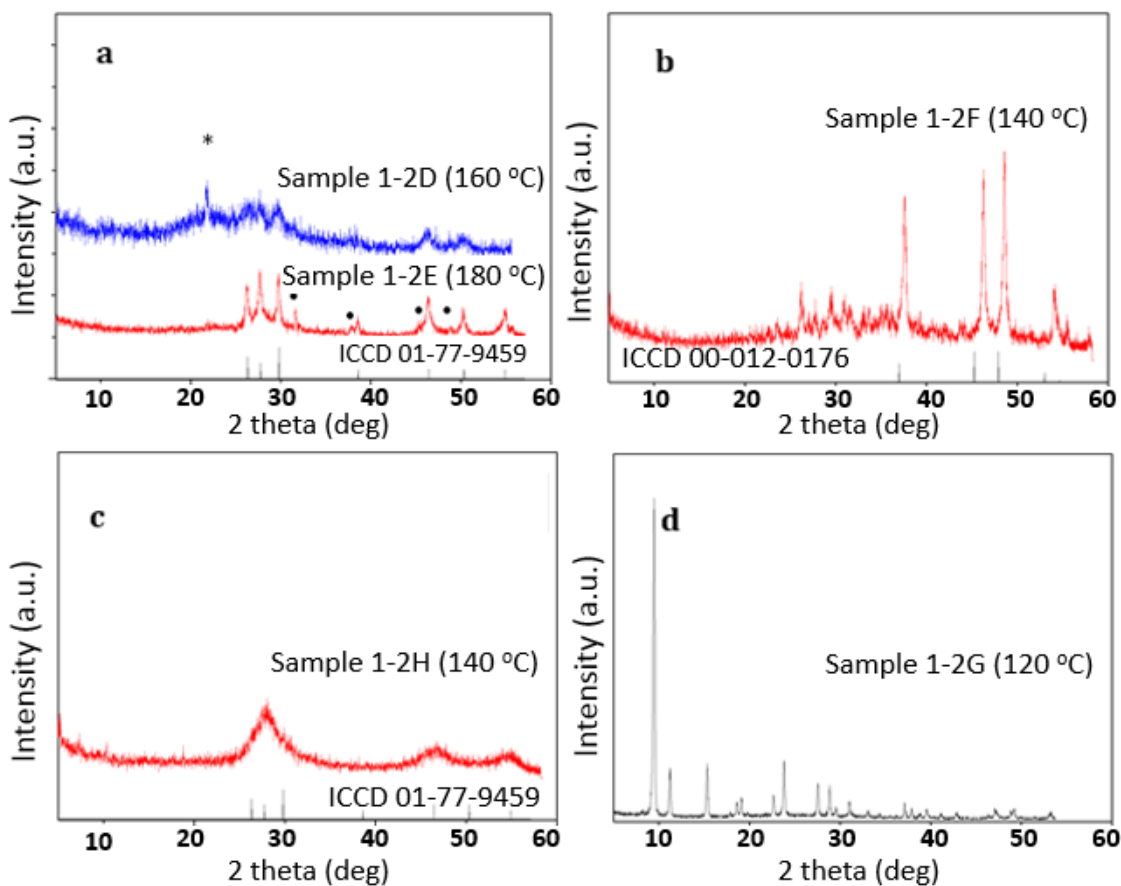
Fig. 2.4 Powder X-ray diffraction patterns of samples 1-2D to 1-2H (see Table 2.1)
(a) temperature variations (b) thiourea as a secondary sulfur source
(c, d) S_8 as a secondary sulfur source
(symbol •: the phases from impurity; symbol ∗ :the phase from precursor 2)

reaction. Compared to sample 1-2E, sample 1-2D (160 °C) has broad peaks, and this is due to that lower temperatures result in smaller particles with lower crystallinity. The PXRD pattern for sample 1-2D also displays one extra peak (shown as *), which can be assigned to precursor **2**, indicating that under these conditions, the conversion of **2** was incomplete.

2.3.2.2 **Sulfur sources**

The addition of a secondary sulfur source to reactions was investigated in order to decrease the synthesis temperature and provide a better control of particle size.[29] Thiourea ($SC(NH_2)_2$, 1 equivalent amount) was used at a reaction temperature of 140 °C (Table 2.1: 1-2F). These reactions yielded colourless solutions with a black thin film on the side of the reaction glass bottles. From the PXRD patterns of the black film, Cu_2S was identified as the principal component (Fig. 2.4 (b)). However, there were also multiple peaks around 2θ ~ 30 ° which indicated the possibility of the formation of a second species, possibly $CuInS_2$ nanoparticles. The formation of two type of solids might be because the fact that thiourea can react with the precursor rather than acting as a simple source of sulfur. As such, S_8 was also investigated as a sulfur source, and a red brown precipitate was formed after 24 h of reaction at 140 °C (sample 1-2H). In comparison with the PXRD pattern of 1-2D and 1-2E (as shown in Fig. 2.4 (a)), peaks in Fig. 2.4 (c) are significantly broader but still match previously reported $CuInS_2$. Interestingly, reactions at 120 °C yielded a white precipitate. The white solid showed a high crystallinity from both visual observation through an optical microscope and PXRD (as shown in Fig. 2.4 (d)). The PXRD pattern suggests that this new phase is likely a layered material, as judged from the high intensity peaks in low angle region around 8 °. Single crystals of this material were also isolated by recrystallization from THF, the reaction solvent. Layering the THF solution with hexane yielded colourless single crystals, which were further identified as $Ph_3P=S$ by single crystal X-ray diffraction. More detailed characterization will be needed in the future to probe the components of this system. Overall, although relatively pure products can be obtained from reactions using **2** as a precursor, size control of $CuInS_2$ was difficult at low temperature.

37

2.3.3 Variations in conversion from [(Ph$_3$P)$_2$CuIn(SEt)$_4$] 3 to [(CuInS$_2$)$_x$]

2.3.3.1 **Temperature and Time**

The size of particles obtained from [(Ph$_3$P)$_2$CuIn(S^{t}Bu)$_4$] **2** was difficult to control, possibly due to the small dissociation energy of the S-C bond that makes it easier for particles to aggregate to large sizes. Thus, precursor [(Ph$_3$P)$_2$CuIn(SEt)$_4$] **3** was probed since the bond energy of S-Et is 72 kcal/mol, which is stronger than S-^{t}Bu but weaker than S-Ph.[30] In order to pinpoint the best conditions, variations in temperature and time were investigated.

By using **3** as the precursor, a number of control experiments were conducted under different temperatures from 80 ℃ to 200 ℃. When the reaction temperatures were lower than 120 ℃, no precipitate was observed, but the colour of the reaction solution changed from colourless (80 ℃) to yellow (100 ℃). Thus, 120 ℃ seems to be the lowest temperature to trigger precipitate formation; all reactions which yielded a precipitate are listed in Table 2.2. The product colour darkened with increasing temperatures. As shown in Table 2.2, the mother liquor for sample 1-3A was colourless and ^{1}H NMR data indicated the presence of unconsumed **3**. Sample 1-3B, which was prepared at 140 ℃, displayed no

Table 2.2   Reaction conditions for precursor 2 (l: mother liquor; s: precipitate)

Sample	T/ ℃	t/h	Solvent	Colour
1-3A	120	24	THF	colourless (l), white(s)
1-3B	140	24	THF	yellow (l), pale yellow(s)
1-3C	160	24	THF	red brown(s)
1-3D	180	24	THF	dark brown(s)
1-3E	180	96	THF	black(s)
1-3F	160	24	DMF	brown(s)
1-3G	160	24	CH$_3$CN	brown(s)

38

evidence for precursor **3** in the ^{1}H NMR spectrum and produced a pale yellow precipitate along with a yellow coloured mother liquor. At higher temperatures, for example 160 °C and 180 °C, red-brown and dark brown precipitates were observed in sample 1-3C and sample 1-3D respectively. Increasing reaction times to 4 days (96 h) at 180 °C (sample 1-3E) yielded a black precipitate. These solids were isolated and characterized by PXRD.

Fig. 2.5 shows the PXRD patterns of sample 1-3C, 1-3D, 1-3E. It can be concluded that changes in the reaction time showed a more significant influence on the formation of wurtzite CuInS$_2$ versus the change in temperature. One low angle peak appears (2θ = 6 °) for sample 1-3C, which is not observed clearly from any other reactions using **3** as a precursor, indicating the possibility of a repeating superlattice present in the structure. In the higher angle region, there are several broad peaks around 2θ = 30 °. For sample 1-3D, the intensity of these peaks is enhanced, but the peak at low angle is not pronounced, suggesting that the size of small particles is increased compared to sample 1-3C; it is difficult to assign these peaks to CuInS$_2$ nanoparticles with much certainty. However, when the reaction time was increased to 96 h (sample 1-3E), well-defined peaks that match those of standard wurtzite CuInS$_2$ (ICCD 01-77-9459) were observed. The sharpness of reflections shown for sample 1-3E indicates that the material synthesized under this condition is in bulk form.
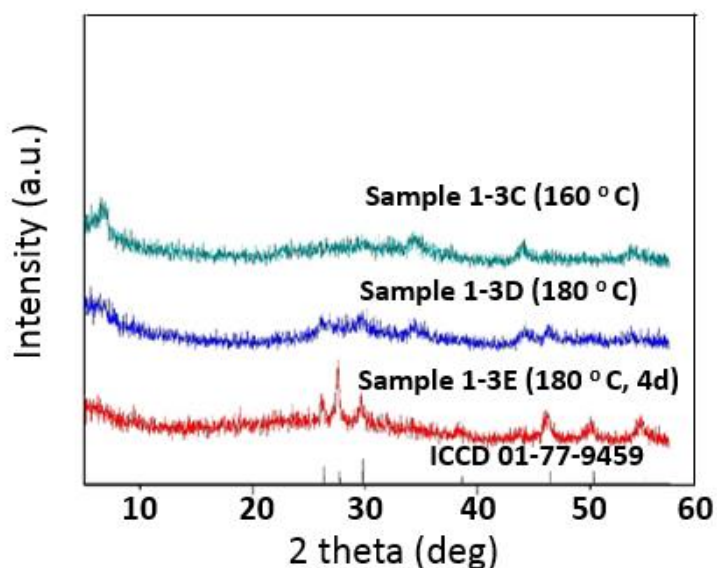
Fig. 2.5 PXRD patterns of samples 1-3C, 1-3D and 1-3E (see Table 2.2)

39

2.3.3.2 **Solvents**

The reaction solvent was another parameter explored for this synthesis. DMF and CH₃CN were used to make a comparison with THF. However, under the conditions as shown in Table 2.2, the products showed a similar brown colour under the same conditions as samples 1-3A to 1-D, even at lower temperatures such as 120 °C and 140 °C. By comparing the PXRD patterns as shown in Fig. 2.6 (patterns of samples 1-3F and 1-3G as examples), it is obvious that the patterns roughly resemble the reference pattern of the CuInS₂ wurtzite nanoparticles. However, from the limitation of the change in colour along with particle size, it is believed that the solvents CH₃CN and DMF are not suitable to control the particle size.
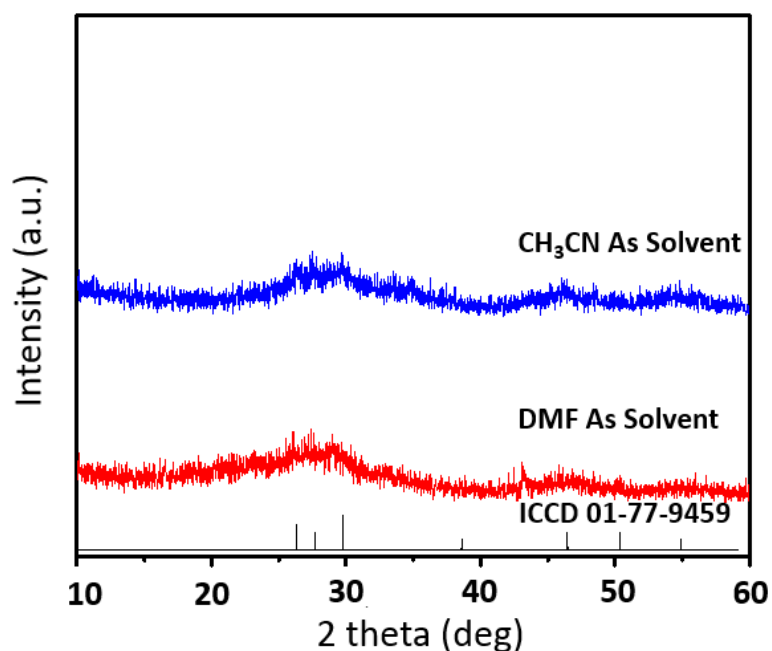
Fig. 2.6 PXRD patterns of sample 1-3F (DMF) and sample 1-3G (CH₃CN)

2.3.3.3 **Sulfur source**

For samples 1-3H to 1-3M, S₈ was used as a source of inorganic sulfur when using **3** as a precursor under solvothermal conditions, in order to further control the size of particles. By changing the reaction conditions, products with different colours were obtained after 24 h, as summarized in Table 2.3. With the increase in reaction temperature from 140 °C to 200 °C, the colour of precipitate formed changed from yellow → orange →

40

red $\rightarrow$ brown $\rightarrow$ black, suggesting the formation of nanoparticles with increased sizes. At the same time, the colour of mother liquors changed from yellow to orange for sample 1-2H and 1-3I, but higher temperature reactions yielded colourless solutions (samples 1-3J to 1-3M). Sample 1-3J contained two different types of precipitate; one was a red, amorphous-looking solid and the second had the form of brown cubic crystals dispersed in the dominant red solid. Although these two materials can be partially separated by centrifuge, it was difficult to control the purity of the products. Increased reaction times also yielded those two moieties. However, by varying the amount of S_8 (doubling the amount for samples 1-3L and halving the amount for sample 1-3M), the two materials could be prepared selectively.

Table 2.3 S_8 addition for synthesis from precursor 3
(l: mother liquor; s: precipitate)

Sample	T °C	c(S_8) molL^{-1}	Solvent	Colour s	Colour l	
1-3H	140	0.017	THF	yellow	yellow	
1-3I	160	0.017	THF	bright red	orange	
1-3J	180	0.017	THF	red + brown	colourless	
1-3K	180	0.009	THF	brown	colourless	
1-3L	180	0.035	THF	red	colourless	
1-3M	200	0.017	THF	black	colourless	1-3H 1-3I 1-3K 1-3L
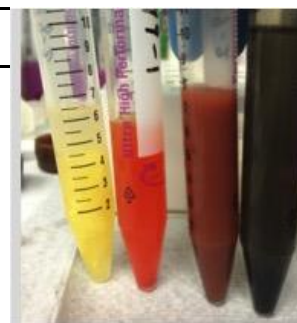
Based on the colours of the different samples, this serie of materials shows a great tunability in the colour and size of the nanoparticles synthesized. Furthermore, using the solvothermal route, the size tunability can be achieved by simply varying the temperature, reaction time and amount of sulfur source, which is very promising for large-scale syntheses.

The PXRD patterns of samples 1-3H, 1-3I, 1-3K and 1-3M were plotted in Fig. 2.7. From the figure, it is clear that with the increase of reaction temperatures, the PXRD patterns changed from broad and overlapping peaks to sharp and individual reflections (sample 1-3H to sample 1-3M). Generally, the broadening of the peaks corresponds to the

41

small size of the nanoparticles and for the bulk materials, they usually have sharp, resolved reflections. Thus, by comparing the patterns, the size should be growing with reaction temperature increase from 140 ℃ to 200 ℃. Compared to the standard $CuInS_2$ wurtzite structure (ICCD 01-77-9459), the peaks of all the samples have a good match to this reference. The peaks assigned to reflections (100) and (101) can be seen clearly even when lower temperatures are used, while the peaks for (110), (103) and (112) sharpened and the peak for (002) was better-resolved when the reaction temperature was 180 ℃. When the temperature was increased to 200 ℃, the last reflection assigned for (102) is resolved and all the sharp and well-defined peaks in the PXRD pattern suggest that bulk $CuInS_2$ materials were formed. This conclusion is also consistent with the black colour of this sample.
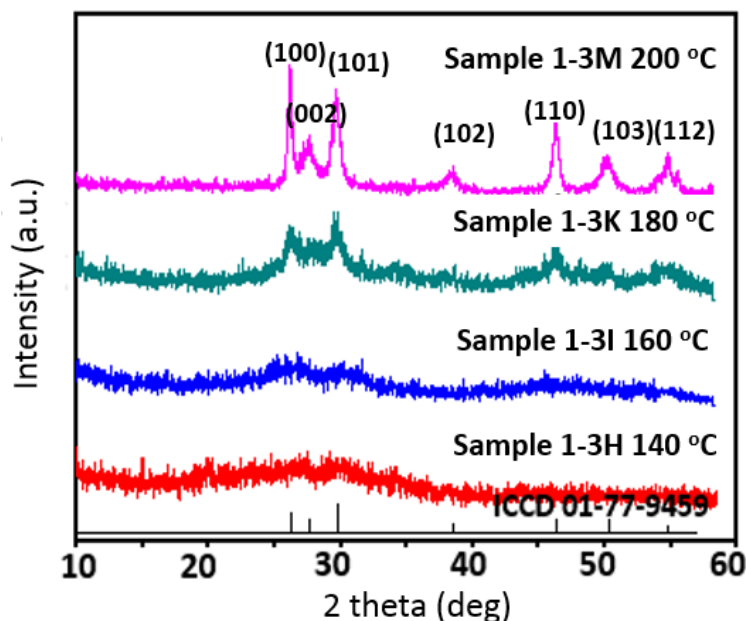
Fig. 2.7 PXRD patterns of samples 1-3H, 1-3I, 1-3K, 1-3M (see Table 2.3)

2.3.4 Characterizations of $[(CuInS_2)_x]$ from precursor **3** $[(Ph_3P)_2CuIn(SEt)_4]$

2.3.4.1 **Absorption Spectroscopy and Band Gap**

Spectra were measured by UV-vis absorption spectra and diffuse reflectance. For the absorption spectra, all samples were suspended in THF, which is the reference solvent. For diffuse reflectance spectra, all samples were diluted to 5 % in mass percentage by mixing with $BaSO_4$ thoroughly.

42
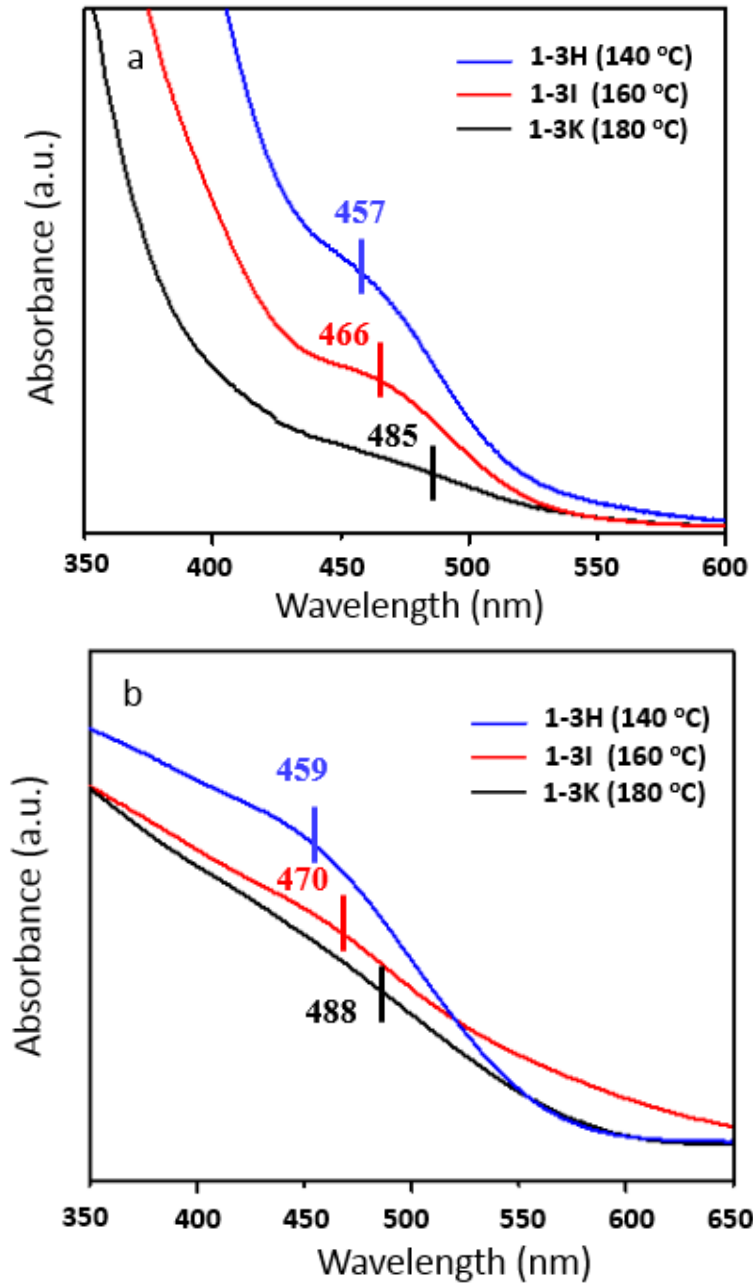
**Fig. 2.8 (a) UV-vis absorption spectra of samples 1-3H, 1-3I, 1-3K (suspended in THF)
(b) Absorption spectra derived from diffuse reflectance data of samples 1-3H, 1-3I, 1-3K**

The UV-vis absorption spectra for samples 1-3H, 1-3I and 1-3K are illustrated in Fig. 2.8 (a). A broad yet resolved peak was observed at different wavelengths for each of the samples. For sample 1-3K (180 °C), the peak is very broad with a maximum at 485 nm (see also Fig. S2-1). Samples 1-3H (140 °C) and 1-3I (160 °C) absorb at 466 nm and 457

43

nm, respectively. This trend is consistent with the phenomenon of a blue shift in the excitonic absorption band with decreasing particle size.[31] Additionally, it is worth noting that the mother liquor of the samples 1-3H (140 ℃) and 1-3I (160 ℃) had a similar colour to the corresponding precipitate, while the mother liquor in sample 1-3K (180 ℃) was colourless. One assumption is that the relatively small particles can partially dissolve in solvent, but the larger particles aggregate and precipitate. Diffuse reflectance spectra were also obtained for sample 1-3H, 1-3I and 1-3K. Generally, the reflectance percentage (R) was collected, but through the Kubelka-Munk equation: A= -lg (R), the absorption spectrum can be viewed, which is shown in Fig. 2.8 (b). As shown, the samples also show a red shift with increased reaction temperatures.

From the absorption spectra, the band gap energy can be calculated. By using Equation 1.3 and 1.4 (as introduced in Chapter 1), a tangent line of curve *(αhν)²* vs *hν* can be plotted, and the value at *(αhν)²* = 0 is the band gap energy of different samples. Fig. 2.9 displays the band gap curves of sample 1-3H, 1-3I and 1-3K transferred from the solid state absorption data. As is shown in the figure, the trend in *E* is consistent with increased particle size of samples prepared at higher temperature:

1.61 eV (1-3K, 180 ℃) < 1.68 eV (1-3I, 160 ℃) < 1.90 eV (1-3H, 140 ℃)
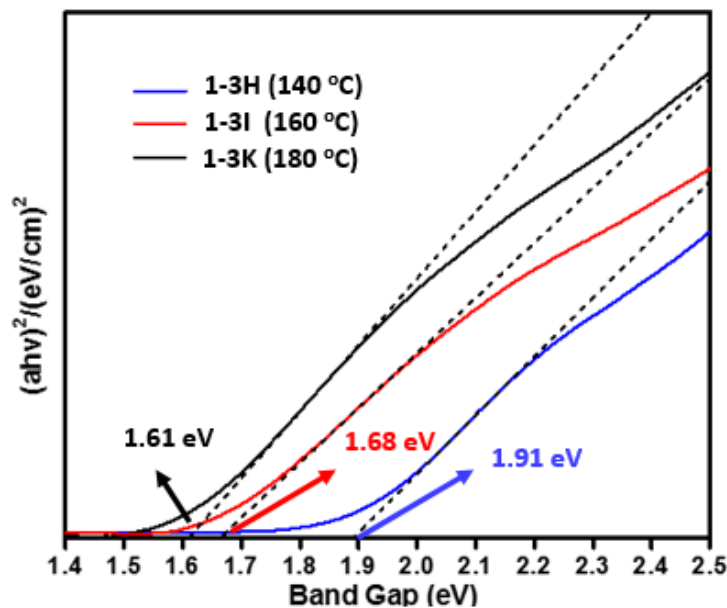
Fig. 2.9 Calculated band gap curves from absorption spectra (Fig. 2.8 (b))

44

It is well known that when the size of particles decrease into the nanoscale range, the band gap will increase due to quantum confinement effects (introduced in Chapter 1), which means that smaller size leads to a larger band gap energy. The Brus Equation (Equation 1.1):

$$E = E_{gap} + \frac{h^2}{8r^2} \left(\frac{1}{m_{e*}} + \frac{1}{m_{h*}} \right)$$

is commonly used to calculate the size of particles. For the wurtzite $CuInS_2$ material, E_{gap} is 1.48 eV;[21] m_e* and m_h* are 0.16 m_e and 1.3 m_e, respectively (where the m_e is the mass of a single electron which is 9.09 $\times 10^{-31}$ kg). From this calculation, the size of $CuInS_2$ nanoparticles in sample 1-3H, sample 1-3I and sample 1-3K are calculated to be 2.4 nm, 3.6 nm and 4.7 nm, consistent with electron microscopy data (see below). Band gap energy curves and size calculation for the samples 1-3F and 1-3G are also plotted and calculated as shown in Fig. S2-2.

2.3.4.2   **Electron Microscopy**

Scanning Electron Microscopy (SEM) measurements for samples 1-3H, 1-3I and 1-3K were obtained along with Energy-Dispersive X-ray (EDX) analyses. From the SEM images (Fig. 2.10) all samples appear as spherical particles at lower resolution. At higher resolution, the diameter of spherical balls were measured and labeled inside the figures. Since the sizes are not uniform, 50 to 100 particles were chosen and an average diameter of particles was obtained. Particles in sample 1-3H (140 ℃) show the smallest size with diameters of ~18 ± 2 nm, and for sample 1-3I (160 ℃), larger spherical sizes of ~25 ± 2 nm were observed. From the EDX analysis, the ratio of Cu : In : S of sample 1-3H and 1-3I are 1.19 : 0.90 : 2.59 and 1.05 : 0.94 : 2.51, respectively, both of which are close to 1 : 1 : 2.5 instead of the expected 1 : 1 : 2 for $CuInS_2$. This is likely due to the formation of $CuInS_{2-X}(SEt)_{2X}$ particles at lower temperatures; TGA analysis supports this hypothesis (Fig. S2-3 and Fig. S2-4). However, sample 1-3K (180 ℃) displayed a Cu : In : S ratio of 0.96 : 1.04 : 1.84 which is very close to the expected 1 : 1 : 2, and the SEM image (inserted figure in Fig. 2.10 (e)) of this sample shows that spheres with diameters around 600 nm were observed under low resolution, while under higher resolution, the particle diameter

was measured to be ~28 $\pm$ 4 nm. Although the trend of particle size is consistent with the colour change and absorption maximum shift, the particle size is much larger than the calculated particle sizes from spectroscopic data, all of which are smaller than 10 nm.
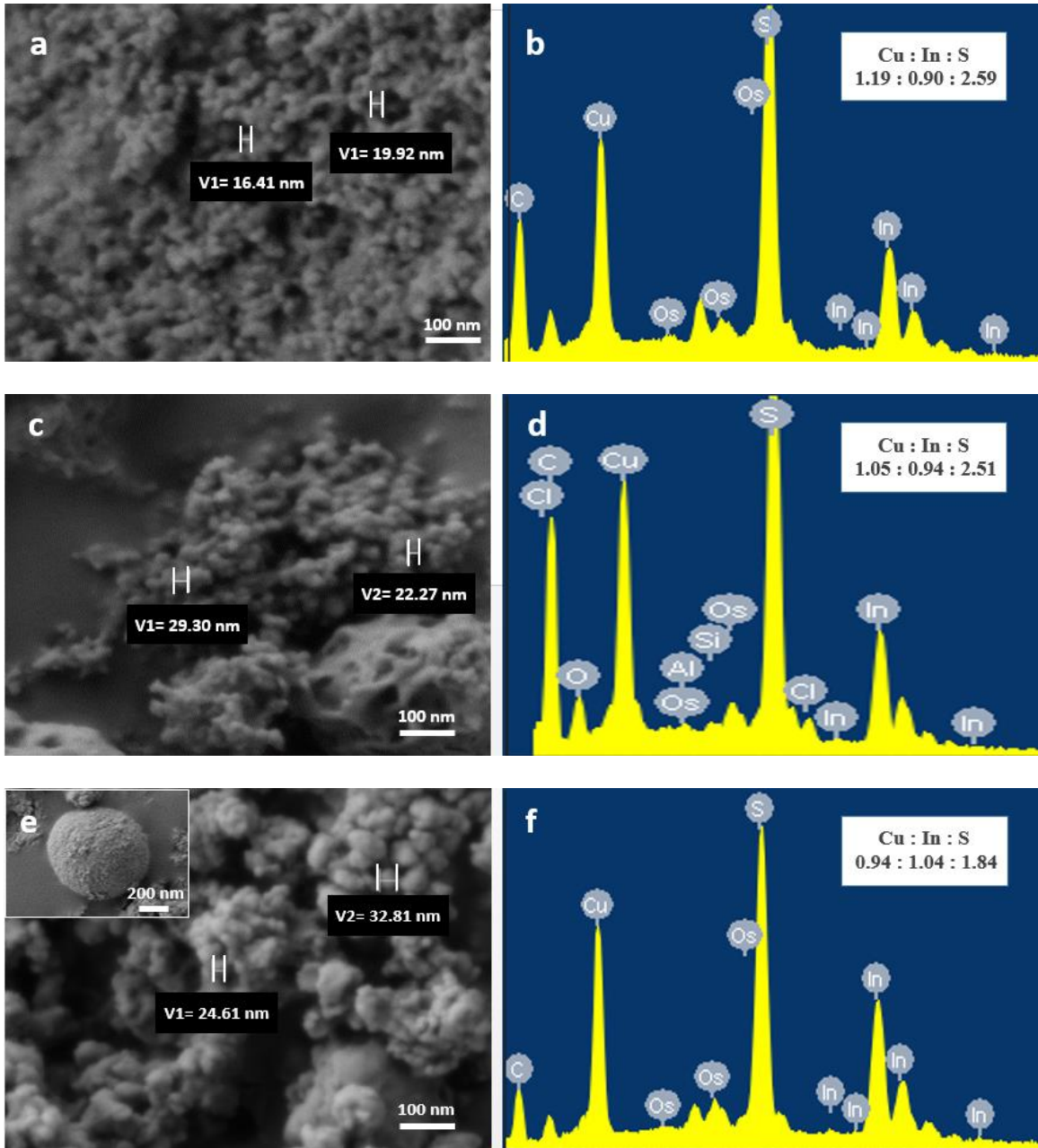
Fig. 2.10 SEM images and EDX analysis for sample 1-3H (a) (b),
1-3I (c) (d), 1-3M (e) (f)
(inset figure in e: spherical shape of particles under low resolution)

46

TEM was used to further resolve the size of individual particles. From Fig. 2.11, it is obvious that all the small particles were still aggregated and overlapping. However, from the outside edges of big aggregation spheres, individual particles can be observed.
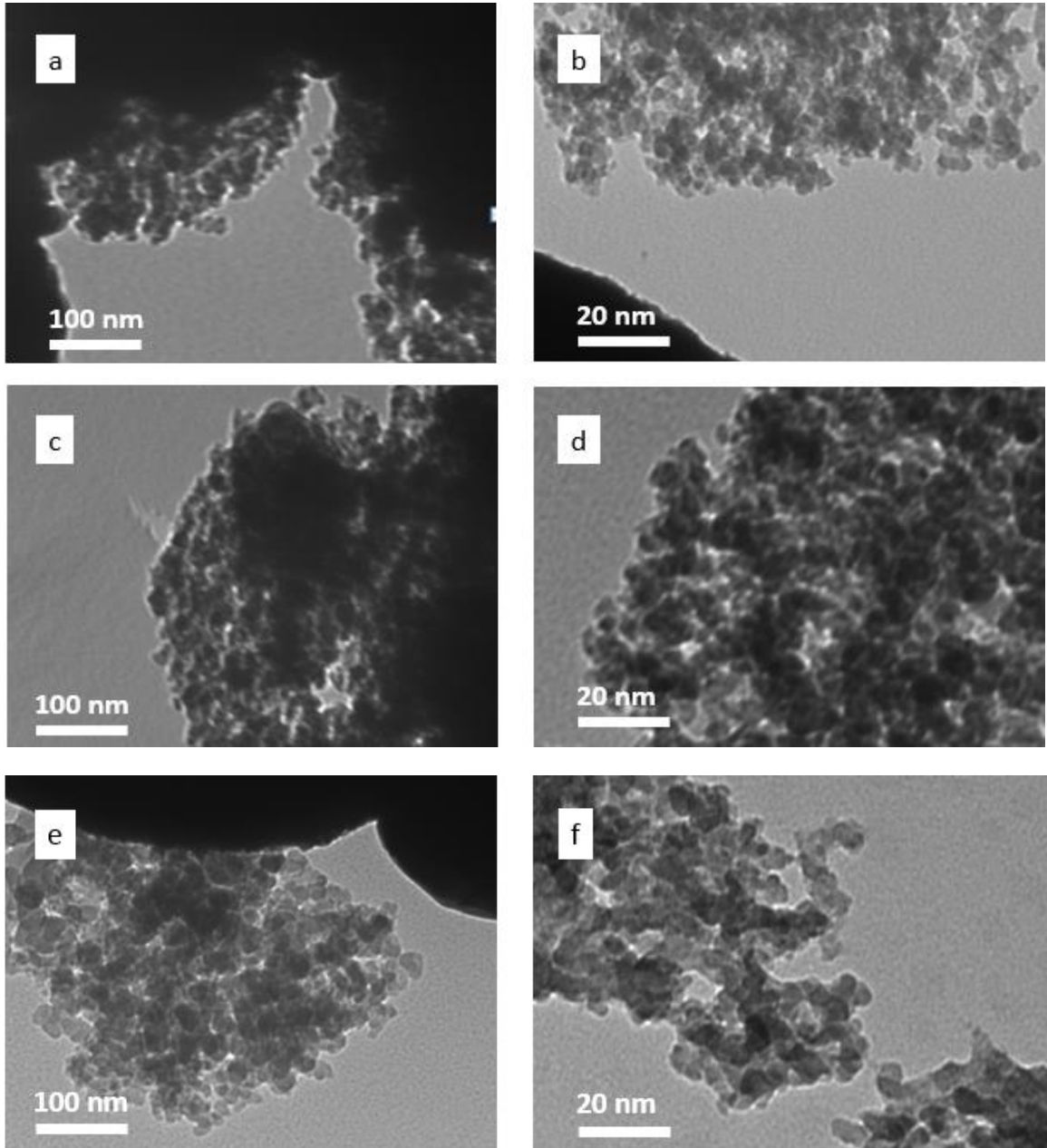
Fig. 2.11 Low resolution TEM images for sample 1-3H (a) (b),
1-3I (c) (d), 1-3M (e) (f)

47

As shown in the HR-TEM images of sample 1-3H (Fig. 2.12), the whole area of image was covered by regular lattices of nanoparticles, and a large amount of crosses were observed due to the different orientations the nanoparticles. From the image, two clear individual particles were circled with a particle size of 2.22 nm and 2.75 nm, respectively. The average diameter of this sample obtained from HR-TEM images is 2.4 ±0.5 nm which agrees with the calculated size of 2.4 nm. The inset image (a) of Fig. 2.12 illustrates clear lattice fringes with spacing of 3.4 Å, which is consistent with the distance of the (100) plane of the wurtzite $CuInS_2$. The fast Fourier Transition (FFT) image (Fig. 2.12 inset (b)) illustrates a highly crystalline material with resolved reflections along with faint rings, which corresponded to (100) and (101) planes. SAED patterns were also measured to obtain an overview within a relatively large area. A selected area is shown in Fig. S2-5 and, unlike the FFT image, SAED patterns (Fig. 2.12 inset (c)) merely displayed faint rings. This is a sign that the nanoparticles are not arranged into a larger superlattice. When this datum is compared to that of the standard wurtzite $CuInS_2$ lattice (ICCD 01-77-9459), all the rings can be assigned to relative crystal lattices as labelled.
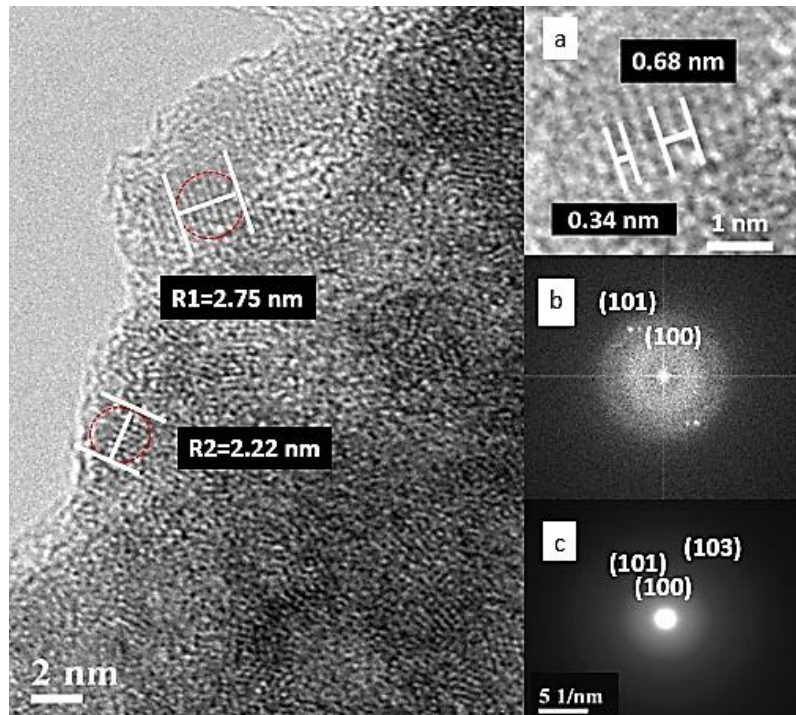
Fig. 2.12 HR-TEM images and FFT for sample 1-3H (inset: a. enlarge area of R1; b. FFT image of this area; c. SAD of low resolution area 0.25 μm^2)

48

Similar measurements were performed on the other two samples, sample 1-3I and sample 1-3K. As shown in Fig. 2.13, the most significant difference for sample 1-3I (160 °C) is that the diameter of the nanoparticles increased to 3.3 ± 0.3 nm. This result is in agreement with the particle sizes calculated from the band gap energy, which is 3.6 nm. From the HR-TEM images, the lattice plane can be measured from the inset image (a) with a fringe of 3.4 Å, consistent with the (100) plane of wurtzite $CuInS_2$ nanoparticles. Unlike the previous sample, the FFT (Fig. 2.14 inset (b)) presents more obvious reflections along with clearer rings; this datum corresponds to the reflections (101) and (100) as labelled. SAED patterns were obtained within the area shown in Fig. S2-6 and displayed in Fig. 2.13 inset (c). The patterns with clear dots and rings show that the crystallinity of this sample is apparently higher than sample 1-3H. However, for both samples, only the (100) lattice plane can be distinguished clearly from the HR-TEM images and this is on account of the small diameter of particles and the limitation of the instrument.
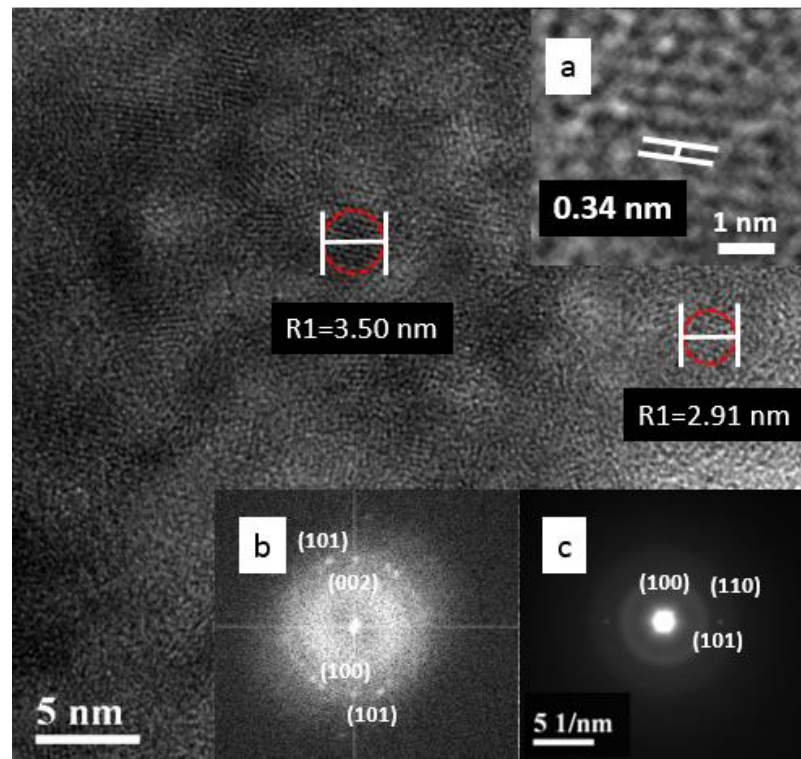
Fig. 2.13 HR-TEM images and FFT for sample 1-3I
(inset: a. enlarge area of R1; b. FFT image of this area;
c. SAD of low resolution area 0.25 μm^2)

49

For sample 1-3K (180 ℃), the HR-TEM images demonstrate some interesting features. As shown in Fig. 2.14, the diameters of nanoparticles are 4.4 ±0.3 nm, which is consistent with the calculated diameter of 4.7 nm. In contrast with samples 1-3H and 1-3I, the HR-TEM images of 1-3K display two different lattice planes. From the Fig. 2.14 inset (a), two different planes with an angle of 69 °were measured as 3.4 Å and 3.0 Å for the fringe distances, which correspond to the (100) and (101) planes, respectively. The FFT image was also obtained and is shown as Fig. 2.14 inset (b). The crystallinity of this sample is improved significantly, and all the diffractions from the patterns can be assigned to planes (100), (101) and (002) respectively.
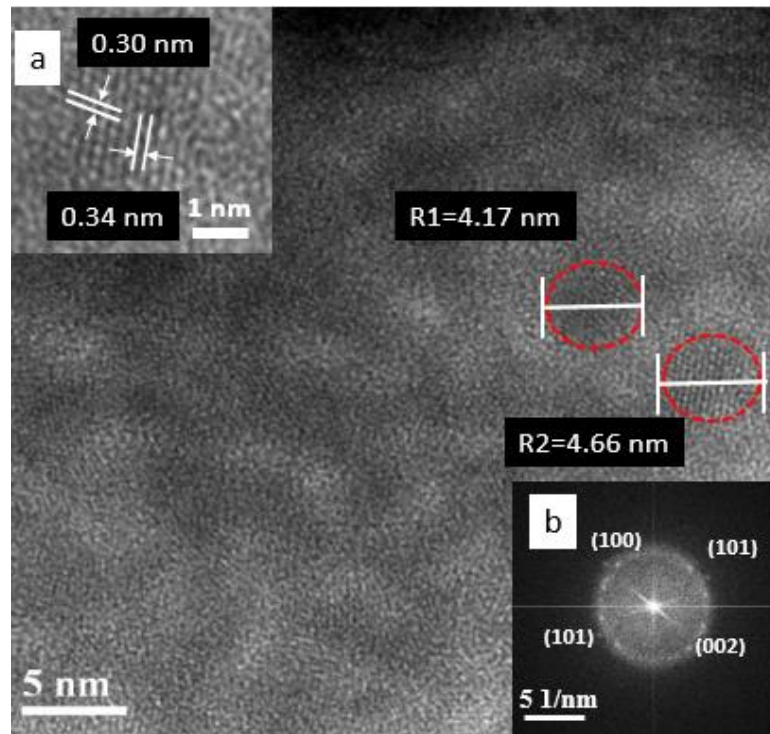
Fig. 2.14 HR-TEM images and FFT for sample 1-3K (nanoparticle)
(inset: a. enlarge area of R1; b. FFT image of whole area)

A second, much larger, product was also observed within sample 1-3K, as shown in Fig. 2.15. From the measurement of the fringe as shown Fig. 2.15 inset (a), the lattice distance is 3.0 Å, corresponding to the (110) plane of $CuInS_2$. The FFT image inset provides evidence of a highly crystalline material with strong reflections; all reflections are assigned to all the main planes of wurtzite $CuInS_2$ including the (100), (002), (101), (102)

50

and (110) planes. Together with EDX analysis, this component is believed to be small wurtzite $CuInS_2$ single crystals. This is also consistent with the higher reaction temperature (180 ℃). From the observed TEM images, the amount of this component is less than 5% of the overall sample.
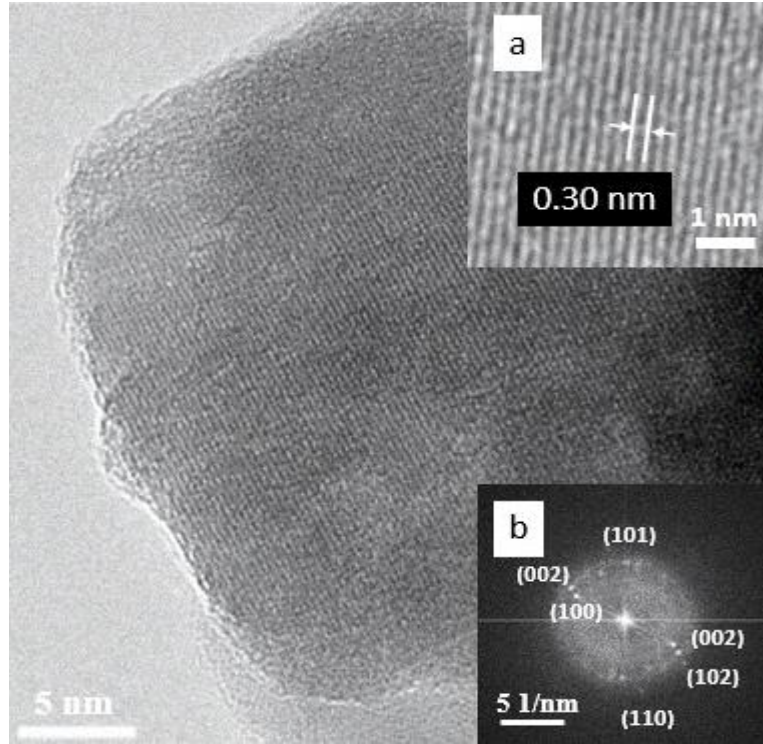
Fig. 2.15 HR-TEM images and FFT for sample 1-3K (single crystal)
(inset: a. enlarge area; b. FFT image of one single crystal)

2.3.4.3　Emission Spectra and Quantum Yield

The emission spectra of samples 1-3H, 1-3I and 1-3K were measured from ethanol suspensions of the samples. As shown in Fig. 2.16 (a), the wavelength of the emission maximum shifted from 648 nm (sample 1-3H, 140 ℃) to 740 nm (sample 1-3K, 180 ℃), consistent with the red shift observed in the absorption spectra. Excitation spectra were measured under the maximum wavelength of emission spectra to compare with absorption spectra. An additional spectrum was also obtained from the mother liquor of the reaction at 125 ℃ (shown in Table 2.4), which is the lowest temperature at which the reaction proceeds to completion after 24 h. Unfortunately, only a small amount of solid can be precipitated and further characterizations were hardly proceed. However, it shows an

51

Table 2.4　Additional reaction conditions for emission spectra (l: mother liquor; s: precipitate)

Sample	T/ °C	t/h	Solvent	Colour
1-3N	125	24	THF	pale yellow (l)
1-3O	160	12	THF	red-brown (s)
1-3P	160	36	THF	brown (s)

obvious emission with a peak at 580 nm. Compared with the size and emissions of other samples, the current sample should have a diameter even smaller than 2.4 nm (sample 1-3H). By comparing the emission spectra of additional samples 1-3O and 1-3P (reaction times are shown in Table 2.4) with sample 1-3I (24 h), it can be observed that the emission intensity could be improved via longer reaction times (Fig. 2.16).
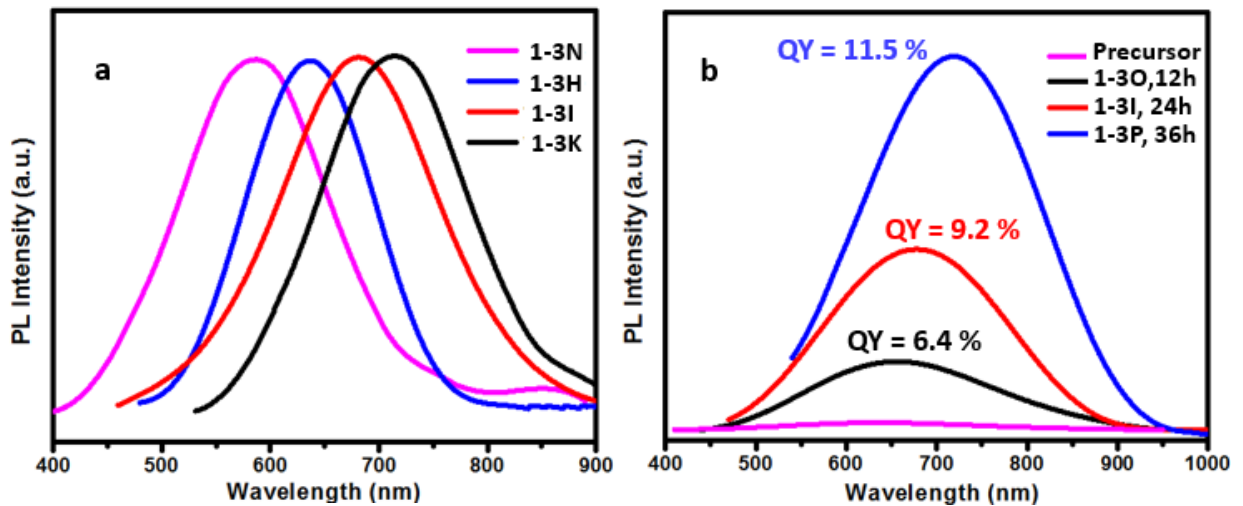
Fig. 2.16 Emission spectrum of sample 1-3H to 1-3P
a. Various of temperatures in 24h reaction;
b. Various of reaction times under 160 ºC

In order to calculate the quantum yield of the samples, a reference solution of Rhodamine B was prepared, which has a known quantum yield of 89 % at excitation wavelength between 450 nm to 500 nm.[32] According to Equation 1.6:

$$\Phi_f^s = \frac{F^s f_i n_s^2}{F^i f_s n_i^2} \Phi_f^i$$

The quantum yield of samples 1-3N, 1-3H, 1-3I and 1-3K were 2.1 %, 4.7 %, 9.1 % and 10.4 %. However, a significant improvement in quantum yields was observed with extended reaction times. As shown in Fig. 2.16 (b), sample 1-3P (160 °C, 36 h) exhibited the highest quantum yield (11.5 %) of all the samples with a reaction time of 36 h, while a reaction time of 12 h let to a drastic reduction in quantum yield to 6.5 % (sample 1-3O).

2.4 **Conclusions**

Due to the suitable bond enthalpy ($\Delta H_{f\ (S-Et)}$ = 72 kcal/mol), precursor **3** [(Ph$_3$P)$_2$CuIn(SEt)$_4$] is the best precursor for fabrication of [(CuInS$_2$)$_x$] nanoparticles. When S$_8$ was used as a second sulfur source, the nanoparticle products from this precursor exhibited a controllable sample colour, which is directly related to the size of the nanoparticles. Three significant diameters of particles were obtained with fine size control: 2.4 ±0.5 nm, 3.3 ±0.4 nm and 4.4 ±0.3 nm. Both the absorption and emission spectra of these nanoparticles exhibited a red shift with growth of particle size, and the quantum yields of emission were improved by adjusting either the reaction temperature or the reaction time. Among all of the synthetic trials, the highest quantum yield (11.5 %) was obtained at 160 °C for 36 h, which was a slight improvement in comparison to previously published quantum yields of CuInS$_2$.[18, 25] This single source precursor synthesis via solvothermal methods provides a facile route to fabricate CuInS$_2$ materials in a tunable size within one step, and this method holds promise for the fabrication of similar ternary semiconductors.

53

References

1. P. Rivera Gil, G. Oberdorster, A. Elder, V. Puntes and W. J. Parak, *Acs Nano*, 2010, **4**, 5527-5531.

2. M. G. Panthani, V. Akhavan, B. Goodfellow, J. P. Schmidtke, L. Dunn, A. Dodabalapur, P. F. Barbara and B. A. Korgel, *J. Am. Chem. Soc.*, 2008, **130**, 16770-16777.

3. W. J. Yue, S. K. Han, R. X. Peng, W. Shen, H. W. Geng, F. Wu, S. W. Tao and M. T. Wang, *J. Mater. Chem.*, 2010, **20**, 7570-7578.

4. B. Tell, J. L. Shay and H. M. Kasper, *Phys. Rev. B*, 1971, **4**, 2463-2471.

5. A. Pein, M. Baghbanzadeh, T. Rath, W. Haas, E. Maier, H. Amenitsch, F. Hofer, C. O. Kappe and G. Trimmel, *Inorg. Chem.*, 2011, **50**, 193-200.

6. N. T. Nassar, R. Barr, M. Browning, Z. W. Diao, E. Friedlander, E. M. Harper, C. Henly, G. Kavlak, S. Kwatra, C. Jun, S. Warren, M. Y. Yang and T. E. Graedel, *Environ. Sci. Technol.*, 2012, **46**, 1071-1078.

7. S. H. Chaki, *Front. Mater. Sci. China*, 2008, **2**, 322-325.

8. D. C. Look and J. C. Manthuruthil, *J. Phys. Chem. Solids*, 1976, **37**, 173-180.

9. F. Y. Shen, W. X. Que, Y. C. He, Y. Yuan, X. T. Yin and G. F. Wang, *Acs Appl. Mater. Interfaces*, 2012, **4**, 4087-4092.

10. J. J. M. Binsma, L. J. Giling and J. J. Bloem, *Cryst. Growth* 1980, **50**, 429-436.

11. A. R. Barron and C. Smith, OpenStax-CNX, 2010.

12. H. Hahn, G. Frank, A. D. Meyer and Z. Storger, *Anorg.Chem*, 1953, **271**, 153-155.

13. D. C. Pan, L. J. An, Z. M. Sun, W. Hou, Y. Yang, Z. Z. Yang and Y. F. Lu, *J. Am. Chem. Soc.*, 2008, **130**, 5620-5621.

14. S. J. Lei, C. Y. Wang, L. Liu, D. H. Guo, C. N. Wang, Q. L. Tang, B. C. Cheng, Y. H. Xiao and L. Zhou, *Chem. Mater.*, 2013, **25**, 2991-2997.

15. Y. X. Qi, Q. C. Liu, K. B. Tang, Z. H. Liang, Z. B. Ren and X. M. Liu, *J. Phys. Chem. C*, 2009, **113**, 3939-3944.

16. H. Z. Zhong, Z. L. Bai and B. S. Zou, *J. Phys. Chem. Lett.*, 2012, **3**, 3167-3175.

17. K. Nose, Y. Soma, T. Omata and S. Otsuka-Yao-Matsuo, *Chem. Mater.*, 2009, **21**, 2607-2613.

18. L. Li, A. Pandey, D. J. Werder, B. P. Khanal, J. M. Pietryga and V. I. Klimov, *J. Am. Chem. Soc.*, 2011, **133**, 1176-1179.

19. L. De Trizio, M. Prato, A. Genovese, A. Casu, M. Povia, R. Simonutti, M. J. P. Alcocer, C. D'Andrea, F. Tassone and L. Manna, *Chem. Mater.*, 2012, **24**, 2400-2406.

20. J. Kolny-Olesiak and H. Weller, *Acs Appl. Mater. Interfaces*, 2013, **5**, 12221-12237.

21. X. Shen, E. A. Hernandez-Pagan, W. Zhou, Y. S. Puzyrev, J. C. Idrobo, J. E. Macdonald, S. J. Pennycook and S. T. Pantelides, *Nature Communications*, 2014, **5**, 5431 .

22. S. T. Connor, C. M. Hsu, B. D. Weil, S. Aloni and Y. Cui, *J. Am. Chem. Soc.*, 2009, **131**, 4962-4966.

23. A. R. Tao, S. Habas and P. D. Yang, *Small*, 2008, **4**, 310-325.

24. M. Williams, R. M. Okasha, J. Nairn, B. Twamley, T. H. Afifi and P. J. Shapiro, *Chem. Commun.*, 2007, **30**, 3177-3179.

25. W. S. Song and H. Yang, *Chem. Mater.*, 2012, **24**, 1961-1967.

26. W. B. Sidney, *J. Am. Chem. Soc.*, 1978, **1**, 23-35.

27. K. K. Banger, Y. Yamashita, K. Mori, R. L. Peterson, T. Leedham, J. Rickard and H. Sirringhaus, *Nature Mater.*, 2011, **10**, 45-50.

28. K. K. Banger, M. H. C. Jin, J. D. Harris, P. E. Fanwick and A. F. Hepp, *Inorg. Chem.*, 2003, **42**, 7713-7715.

29. K. K. Banger, J. Cowen and A. F. Hepp, *Chem. Mater.*, 2001, **13**, 3827-3828.

30. S. W. Benson, *Chem. Rev.*, 1978, **78**, 23-35.

31. I. Tsuji, H. Kato, H. Kobayashi and A. Kudo, *J. Am. Chem. Soc.*, 2004, **126**, 13406-13413.

32. M. Grabolle, M. Spieles, V. Lesnyak, N. Gaponik, A. Eychmuller and U. Resch-Genger, *Anal. Chem.*, 2009, **81**, 6285-6294.

CHAPTER 3. CuInSe$_2$ and AgInS$_2$ Nanoparticles

3.1 Introduction

Based on the successful exploration of the ternary CuInS$_2$ nanoparticles through solvothermal routes with the use of single source precursors, this chapter describes the synthesis and characterization of the related semiconductor materials CuInSe$_2$ and AgInS$_2$. In contrast to CuInS$_2$ nanoparticles, the CuInSe$_2$ and AgInS$_2$ materials are commonly studied in bulk as potential materials for absorber layers in solar cells.

3.1.1 CuInSe$_2$ Nanoparticles

At the same time when CuInS$_2$ was synthesized, copper indium diselenide (CuInSe$_2$) was also synthesized and characterized by Hahn in 1953.[1] The first solar cell made of bulk CuInSe$_2$ was fabricated in 1974 by Wagner, in which CuInSe$_2$ was used in absorber layer as the p-type part, and cadmium sulfide (CdS) was casted on the surface as the n-type part.[2] The studies regarding this new solar cell began to be popular and by the end of 1975, the reported devices had already exhibited an efficiency of 12 %.[3] However, the complicated fabrication procedures as well as the difficulties involved with growing high quality single crystals cooled down the enthusiasm. Although efforts were made, such as moving the key points towards the fabrication of CuInSe$_2$/CdS thin films by Kazmerski [4] and applying a co-evaporation method to fabricate CuInSe$_2$ films on ceramic substrates coated with molybdenum by Clark,[5, 6] the disadvantages of this kind of solar cell were still significant in terms of commercialization, including the limited efficiency, the high cost of the fabrication procedure and the high probability of defects. Consequently, studies regarding this material stood still for decades until the early 90s, when advancements in nanotechnology brought CuInSe$_2$ back to the spotlight in solar cells based on the exploration of CuInS$_2$ nanoparticles. To date, the efficiency of the solar cells based on CuInSe$_2$ has increased to 15 %,[7] and with modern fabrication techniques such as doping and coating, CuInSe$_2$ has a wider composition which further improved the conversion efficiency and optical properties. For instance, incorporating Ga into CuInSe$_2$ gives rise to the Cu(In,Ga)Se$_2$ material, which shows a significantly enhanced efficiency in solar cells. Presently, the highest reported efficiency of Cu(In,Ga)Se$_2$ cells is 20.3 %.[8, 9]

59

Similar to the crystal structures of $CuInS_2$, $CuInSe_2$ also has several different morphologies such as chalcopyrite, zinc blende and wurtzite. Chalcopyrite is the most stable structure at room temperature, while the zinc blende and wurtzite structures are more commonly observed in nanoscale $CuInSe_2$. It is noteworthy that for each morphology of $CuInSe_2$, it prefers to form a CuAu ordered structure, which has a small energy of formation (ΔE_{form} = - 2.05 meV/atom).[10] An illustration of the CuAu-type structure is given in Fig. 3.1 (b).[11] In comparison to a regular chalcopyrite structure (Fig. 3.1 (a)), more Cu atoms exist in the CuAu-like ordering lattice, which decreases the Cu vacancies.[12] However, this small change has no significant influence on the properties compared to the regular chalcopyrite structure. The CuAu-like ordering also exists in the zinc blende and wurtzite structures. Compared to the chalcopyrite structure, $CuInSe_2$ in the wurtzite structure is preferable for fabrication since it can provide higher copper vacancies, which yields a higher efficiency when $CuInSe_2$ is used as an absorber layer.[13] Thus, this project focuses on the synthesis and characterization of $CuInSe_2$ nanoparticles with the wurtzite structure.
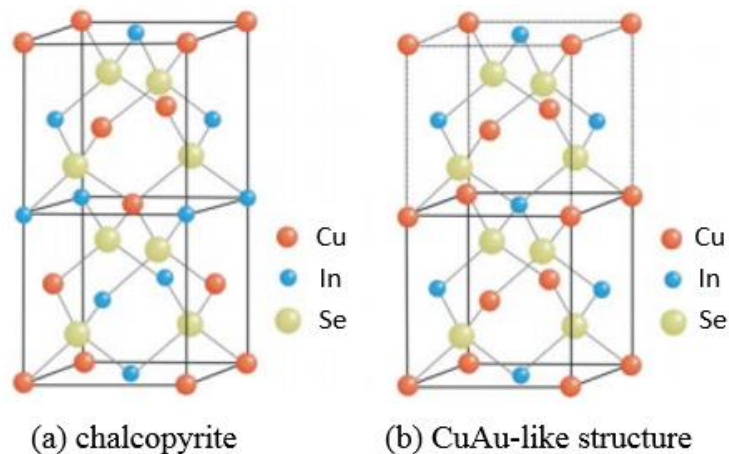
**Fig. 3.1 (a) Regular chalcopyrite structure and
(b) CuAu-like chalcopyrite structure of CuInSe₂ crystals**

The absorption coefficient of bulk $CuInSe_2$ is $3 - 6 \times 10^5$ cm^{-1}, which is the highest value reported among the ternary semiconductor materials.[14] This value is due to a direct band energy that allows effective transitions without any momentum shift. Another important parameters in producing solar cells is the band gap energy. In $CuInSe_2$ bulk material, the reported band gap energy varies from 0.81 to 1.04 eV, but 1.04 eV is the

generally accepted value and widely used for the calculation of the particle size.[15, 16] Because of the fact that the optimum band energy matched with the solar spectrum is 1.4 ~ 1.5 eV, it limits further improvements in efficiencies for this material, especially in the bulk form. To date, most of the $CuInSe_2$-based solar cells which have efficiencies greater than 14 % are generally prepared with the addition of Ga.[17, 18] However, the procedure of doping increases the complexity of synthesis route and makes it challenging to obtain a uniform morphology.[19] Thus, aside from doping, another promising method to explore is to tune the band gap energy by decreasing the size of $CuInSe_2$ to the nanoscale based on the quantum confinement effect.

3.1.2 $AgInS_2$ Nanoparticles

In a similar manner to $CuInSe_2$, $AgInS_2$ also exists in three different morphologies: chalcopyrite, zinc blende and wurtzite.[20, 21] Because the band gap of $AgInS_2$ is around 1.87 - 2.03 eV, it has a prominent absorption in the visible and near infrared region.[22, 23] This band gap, along with its large absorption coefficient ($\sim 10^5$ cm^{-1}), makes $AgInS_2$ a good candidate for inclusion in solar cells.

In addition to the application as an absorber layer in solar cells, $AgInS_2$ nanoparticles are also attractive due to the fact that their optical properties are suitable for the fabrication of optoelectronic devices. Nanosized $AgInS_2$ is a good candidate for this application, since it exhibits a large optical nonlinearity due to the quantum size and interfacial effects. One related ternary semiconductor nanomaterial, $AgGaS_2$, has been reported as a useful non-linear optical material,[24, 25] and this has triggered interest in $AgInS_2$, which is assumed to have similar structure and composition. For $AgInS_2$, doping is also a common method to tune the band gap and generate a wide photoluminescence range. For example, as shown in Fig. 3.2, by doping Zn inside $AgInS_2$, the photoluminescence colour can be tuned from green to red (Fig. 3.2 (a)). From the emission spectrum (Fig. 3.2 (b)), it is clear that the wavelength of the emission peak shifts from 775 to 540 nm when the x value of $(AgIn)_xZn_{2(1-x)}S_2$ is decreased from 1.0 to 0.4.[26] Without doping, it is also possible to obtain those properties by tuning the $AgInS_2$ particles sizes to nanoscale, however, few investigations have been reported up until now.
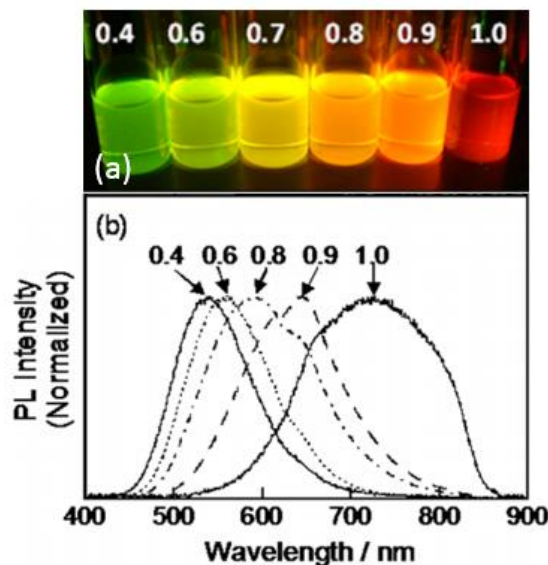
61

Fig. 3.2 The (a) photoluminescence colours and (b) emission spectra of AIS doped with Zn. The value of x in $(AgIn)_xZn_{2(1-x)}(S_2CN(C_2H_5)_2)_4$ ranges from 0.4 to 1.0.
(Reproduced with permission of ref. 26. Copyright © 2014 American Chemical Society)

3.1.3 Synthesis Routes for CuInSe$_2$ and AgInS$_2$

Various methods have been studied for the preparation of CuInSe$_2$ and AgInS$_2$ nanoparticles, such as single source decomposition,[27] hot injection method,[28] powder metallurgy and solvothermal method.[29-31] Recently, colloidal nanoparticles prepared by hot injection have been extensively explored. However, this route is limited to the fabrication of binary nanoparticles in good quality, such as CdS, InAs and PbSe.[32-34] The synthesis of more complex semiconductor materials such as ternary sulfides is rarely performed by using this method due to the reduced crystallinity and purity of the final products. For traditional routes for ternary materials such as powder metallurgy, high temperatures are required to yield thermodynamically stable structures, but offer little control over size and morphology.[35] In contrast, low temperatures can protect the ternary core because the solvent can help kinetically trap metastable materials with more complex structures and compositions.[36, 37] Thus, the solvothermal method is the most suitable one. The solvothermal method can be performed under relatively low temperatures, and it is also convenient and relatively environmental friendly. When using single precursors as starting materials, this method can be used for industrial-scale production. In this project, a procedure similar to that developed for CuInS$_2$ in Chapter 2 will be used to synthesize CuInSe$_2$ and AgInS$_2$ nanoparticles.

62

3.2 Experimental Descriptions

3.2.1 Materials

Sodium methoxide, sodium metal, diphenyl diselenide, ethanethiol, indium (III) chloride, copper (I) chloride, silver (I) chloride and naphthalene were purchased from Aldrich or VWR and used as received. Triphenylphosphine was purchased from Aldrich and vacuum dried for 4 hours at room temperature, then stored under inert atmosphere. Solvents such as toluene, tetrahydrofuran (THF) and hexane were dried by passage through packed columns of activated alumina using a commercially available MBraun MB-SP Series solvent purification system. Methanol and dichloromethane (CH_2Cl_2) were distilled and dried over CaH_2 and P_2O_5, respectively. Solvents such as dimethylformamide (DMF) and acetonitrile (CH_3CN) were degassed under N_2 flow for 30 minutes and stored under inert atmosphere. For ^1H NMR spectroscopy solvents, chloroform-d was purchased from Aldrich and distilled over P_2O_5 while dmso-d_6 was purchased from Aldrich and used directly without further purification.

All synthesis and handling procedures were carried out under an atmosphere of high purity dried nitrogen, using standard double manifold Schlenk line techniques and an MBraun Labmaster 130 glovebox. For the solvothermal synthesis, stainless steal autoclaves and disposable glass bottles (30 mL) with Teflon caps were used.

3.2.2 Syntheses

3.2.2.1 **Synthesis of Na[SePh]**

Na[SePh] was prepared in a modification of a literature procedure.[38] A sodium lump (1.50 g, 65.2 mmol) was carefully removed from oil and wiped, then quickly cut into small pieces and placed into a Schlenk vessel under N_2. Ph_2Se_2 (10.6 g, 34.0 mmol) and a catalytic amount of naphthalene (1 g, 7.8 mmol) were dissolved in 50 mL of dry THF, producing a transparent bright orange solution. This solution was added to the sodium pieces under N_2 flow and the mixture was stirred overnight vigorously using a magnetic stirrer and stir bar. Upon the reaction initiation (about 15 min), the solution turned cloudy, progressively accumulating a large amount of fine white precipitate. The reaction came to

63

completion when the most of sodium pieces were gone, and the orange colour of solution faded considerably. The white precipitate of Na[SePh] was isolated by filtration of the mixture over Celite™ and dried under vacuum. Na[SePh] was then dissolved by running dry CH_3CN through the filter and collecting the filtrate. The volume of filtrate was then reduced under vacuum, resulting in crystallization of Na[SePh] as white needles. The product was isolated by vacuum filtration in the glove box and thoroughly dried. Yield = 52 %; ^{1}H NMR (400 MHz; dmso-d_6, 23 ℃): δ 7.29 (d, 2H, Ph), 6.58-6.64 (m, 3H, Ph). The ^{1}H NMR data match with those from a previously published report. [38]

3.2.2.2   Synthesis of [(Ph₃P)₂CuIn(SePh)₄]

[(Ph₃P)₂CuIn(SePh)₄] was synthesized by a slight modification of the published procedure:[27] Na[SePh] (0.71g, 4 mmol) was dissolved in 15 mL methanol. After stirring for 30 min, $InCl_3$ (0.230 g, 1 mmol) dissolved in 5 mL of methanol was added, and reacted for an additional 1.5 hours to form Na[In(SePh)₄]. PPh₃ (0.574 g, 2.19 mmol) and CuCl (0.114 g, 1.15 mmol) were then combined in 15 ml of CH_2Cl_2 and the mixture was added dropwise to Na[In(SePh)₄]. The reaction mixture was kept stirring overnight, affording a light yellow solution with a white precipitate. The solvent volume was reduced under vacuum to half and 20 mL of methanol was added to fully precipitate the product rather than the NaCl by-product. The white precipitate was collected by filtration and washed with methanol twice, then the solid was dried for 2 h, affording [(Ph₃P)₂CuIn(SePh)₄] as a white solid. Yield = 81 %; ^{1}H NMR (400 MHz; CDCl₃, 23 ℃): δ 6.85 (s, 8H); δ 7.00 (d, 4H); δ 7.23 (br d, 10H); δ 7.35 (m, 8H). The data are consistent with reported values.[39]

3.2.2.3   Synthesis of [(Ph₃P)₂AgIn(SCOCH₃)₄]

[(Ph₃P)₂AgIn(SCOCH₃)₄] was synthesized in a similar method as described for [(Ph₃P)₂CuIn(S)₄] in Chapter 2. A white precipitate was collected and redissolved in 20 mL CH_2Cl_2 and filtered through Celite™ to remove residual NaCl. The solvent was removed under vacuum, affording [(Ph₃P)₂AgIn(SCOCH₃)₄] as a white solid. Yield = 89 %; ^{1}H NMR (400 MHz; CDCl₃, 23 °C);   δ 2.23 (s, 12H, CH₃); δ 7.27-7.40 (m, 30H, P(C_6H_5)₃). The data are consistent with reported values.[40]

64

3.2.2.4 Synthesis of $[(CuInSe_2)_x]$ and $[(AgInS_2)_x]$ Nanoparticles

Reactions were performed under increased pressure in a sealed reactor at different solvothermal conditions for varying temperatures and times. A typical procedure for the preparation of $[(CuInSe_2)_x]$ and $[(AgInS_2)_x]$ nanoparticles was similar to the procedure of $[(CuInS_2)_x]$ introduced in Chapter 2. An appropriate amount of precursor (0.1mmol) was combined with THF (10-15 mL) in a 30 mL glass bottle with a Teflon cap. After all the starting materials were dissolved in the solvent, the bottle was sealed in a stainless steel autoclave and heated in an oven for several days at a selected temperature. The autoclave was cooled to room temperature gradually without external input after the solvothermal synthesis. If the products precipitated out directly from the reaction, the solid material was collected by centrifugation at 4000 rpm for 15 min, washed several times by the reaction solvent and finally by methanol to remove by-products, and then dried under vacuum for 4-6 h. If coloured solutions formed without any precipitate, 3 to 5 times the volume of methanol was added to precipitate the products, and this solid was also collected by centrifugation. Final samples were purified by using THF and methanol to wash 3 - 5 times. All the samples were stored inside a glovebox, and for the $[(AgInS_2)_x]$ nanoparticles, light exposure was avoided.

For the $AgInS_2$ samples in which the mother liquors had a gradual change in colour, the mother liquors were also separated and the precipitate was collected after the addition of methanol. Afterwards, the product was purified by using degassed acetone to wash 3 times. The samples were suspended in methanol to obtain the UV-vis absorption spectra.

3.2.3 Characterization

All the characterization methods and instrumentation are as found in Chapter 2.

3.3 **Results and Discussion**

In order to simplify the results and discussion, this chapter will be separated into two parts for clarity, aiming to explain the results of solvothermal synthesis for the formation of $[(CuInSe_2)_x]$ and $[(AgInS_2)_x]$ nanoparticles from single source precursors.

3.3.1 $[(CuInSe_2)_x]$ Nanoparticles

Following the synthesis procedure used for $CuInS_2$, various conditions for $CuInSe_2$ were explored. As shown in Table 3.1, both the temperature and reaction time were investigated for this material. One point that should be noted is the fact that, in contrast to $CuInS_2$ products, there was not any precipitate from $CuInSe_2$ samples that settled directly after the cooling procedure in the solvothermal route; only solutions of different colours were formed. Solid samples were obtained by collecting the precipitate that formed after the addition of methanol. After redissolving the precipitates in THF, the different colours of solutions are listed in Table 3.1 and Fig. 3.3, respectively.

Table 3.1   Various conditions for $[(CuInSe_2)x]$ synthesis
(l: solutions of precipitates redissolved in THF)

Sample	T/ °C	t/h	Solvent	Colour (l)
3A	100	24	THF	yellow
3B	120	24	THF	yellow-orange
3C	140	24	THF	orange
3D	160	24	THF	red
3E	160	36	THF	dark red
3F	160	48	THF	brown

66

The second chalcogen addition which was necessary to tune the colour and the size of CuInS$_2$ samples, is not required for CuInSe$_2$ samples (Table 3.1). Two variables, reaction temperature and time, were investigated. ^{1}H NMR spectroscopy was used to confirm reaction completion by the disappearance of precursor resonances. When the temperatures were lower than 100 ℃, the reactions were incomplete, as shown from the resonances of the precursor [(Ph$_3$P)$_2$CuIn(SePh)$_4$].

When the temperature was increased from 100 ℃ (sample 3A) to 160 ℃ (sample 3D), the trend of colour change was yellow → orange → red, which indicated the growth in particle sizes. By keeping the temperature at 160 ℃ and extending the reaction time from 24 h to 48 h (sample 3D to 3F), the colour was turned from red to brown gradually as shown Fig. 3.3. Thus, both the reaction temperature and reaction time can have a great influence on the growth of nanoparticle and the trend of colour change is similar to that found for CuInS$_2$ nanoparticles.
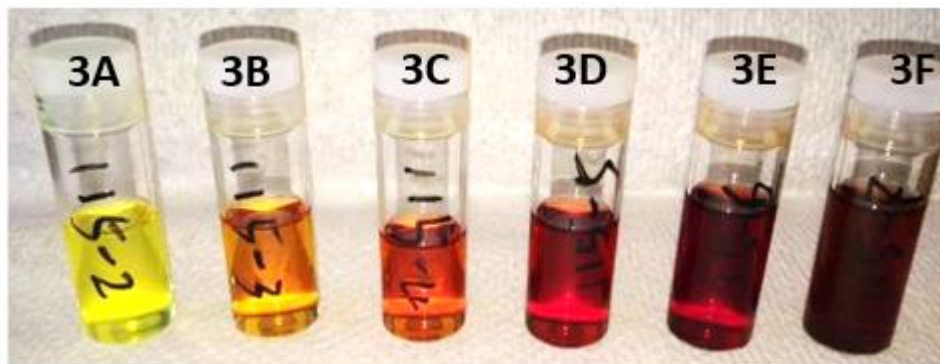
Fig. 3.3 The various colours of CuInSe$_2$ products (see Table 3.1)
(samples were precipitate out by adding methanol and then redissolved in THF)

3.3.1.1 **Powder X-ray Diffraction (PXRD)**

PXRD patterns for samples 3A to 3E were obtained and significant changes could be observed. However, all of them showed the patterns consistent with that of standard wurtzite structural CuInSe$_2$ PXRD patterns (ICCD 01-078-5190). Although reflection positions of all the samples match with the identical peaks, the broadening and overlapping of some reflections made interpretation challenging. As shown in Fig. 3.4, the peaks which are assigned to the reflections (100), (002) and (101) are overlapping at the reaction

67

temperatures lower than 140 ℃ and tend to separate at high temperatures. For the samples prepared at 160 ℃, the peaks (110), (103) and (112) are sharp and narrow due to the regular orientations for the larger particle sizes, although not all peaks are resolved. The reaction time is the second factor which can have an influence on particle size. When the reaction time was extended to 36 h (sample 3E), all reflections are resolved, and the further increment of time will form bulk $CuInSe_2$ materials rather than $CuInSe_2$ nanoparticles.
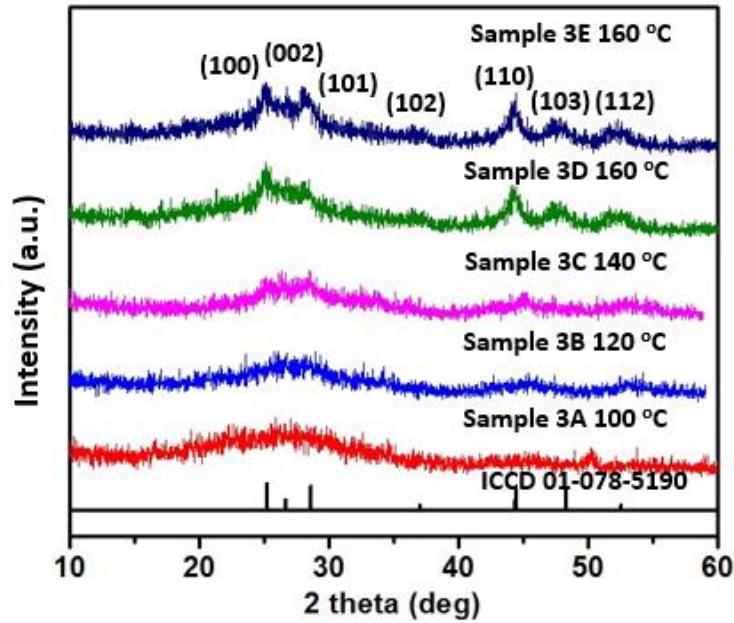
Fig. 3.4   PXRD patterns of samples 3A to 3E (see Table 3.1)

3.3.1.2   **Absorption Spectroscopy and Band Gap Energy**

Both UV-vis solution absorption spectra and diffuse reflectance were obtained for $CuInSe_2$ samples. Fig. 3.5 (a) illustrates the absorption spectra measured from solution $CuInSe_2$ by dissolving the precipitates in THF. Matching with the colour of solutions, which were yellow (sample 3A, 100 ℃), yellow-orange (sample 3B, 120 ℃), orange (sample 3C, 140 ℃) and red (sample 3D, 160 ℃) respectively, the absorption peak shows a red shift that can be assigned to the increased band gap of the nanoparticles. Due to this red shift, the size change is comparable to the colour observed, both of which can confirm that higher synthesis temperatures result in larger particles. The solid state absorption spectra also demonstrate this trend. Fig. 3.5 (b) is the absorption sepctrum conversed from diffuse reflectance data. As shown in Fig. 3.5 (b), the peak of each spectrum matches with the one in Fig. 3.5 (a), and a clear red shift can be observed with increasing temperatures.

68
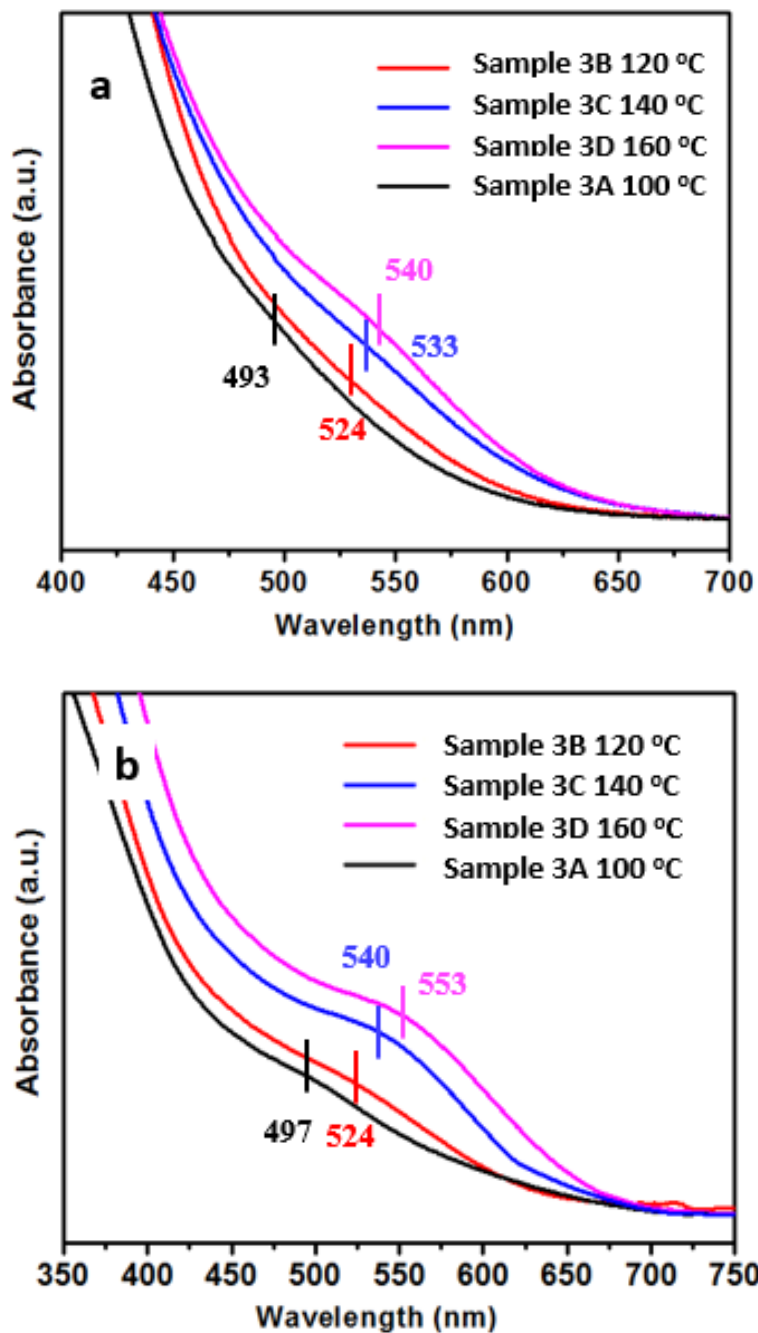
Fig. 3.5 (a) UV-vis absorption spectra of samples 3A to 3D solution (THF as solvent) (b) Absorption spectrum conversed from diffuse reflectance of samples 3A to 3D

The band gap energies of the samples were calculated through the Kubelka-Munk Formula and Tauc Relation (Equation 1.3 and 1.4), that is, by plotting the tangent line of curve $(\alpha h\nu)^2$ vs $h\nu$, the band gap is the x value where $(\alpha h\nu)^2$ equals 0. As shown in Fig. 3.6 which utilized absorption maximum in Fig. 3.5 (a), the largest band gap (1.62 eV) belongs to sample 3A, which was prepared at 100 ℃. When the reaction temperatures increased to 120 ℃, 140 ℃ and 160 ℃, the band gaps of those samples have a gradually reduction from 1.48 eV (sample 3B), to 1.45 eV (sample 3C) and further to 1.37 eV (sample 3D). Compared to bulk wurtzite CuInSe$_2$ with a band gap energy of 1.04 eV (Eg), all samples exhibited a significant increase in band gap energy. Based on the larger energy difference between the band gap ($Eg = 1.04$ eV) of bulk material and the band gap (E) obtained from these samples, it is suggested that the size should be controlled in smaller diameter than CuInS$_2$ nanoparticles due to the application of the Brus Equation (Equation 1.5). However, the size of CuInSe$_2$ nanoparticles are calculated as 2.8 nm, 3.4 nm, 3.5 nm and 4.0 nm for sample 3A, 3B, 3C and 3D, respectively. These diameters are quite similar to the sizes of CuInS$_2$ nanoparticles due to the small value of m_e^* and m_h^* of CuInSe$_2$, which are 0.082 m_e and 0.71 m_e, respectively.
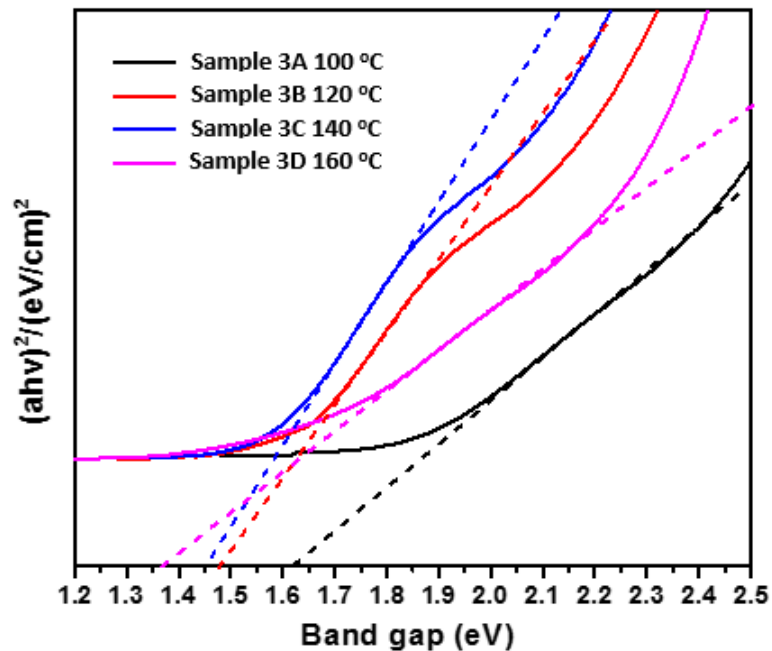
Fig. 3.6 Band gap curves of samples 3A to 3D (see Table 3.1)
(All curves were conversed from relative absorption spectra shown in Fig. 3.5 (b))

3.3.1.3 **Emission Spectroscopy and Quantum Yield**

Two series of emission spectra were recorded: Fig. 3.7 (a) contains the emission spectra obtained from the samples synthesized under different temperatures (100 ℃ and 160 ℃) and Fig. 3.7 (b) displays the emission spectra of samples synthesized at 120 ℃ but with various reaction times (from 18 h to 48 h).

As shown in Fig. 3.7 (a), all four samples have strong emission, and the shift in emission maxima is comparable to the trend of absorption maxima. Although the shift is not as large as the one observed for $CuInS_2$ (~ 200 nm) introduced in Chapter 2, a red shift of 130 nm is still observed. In the emission spectra, the emission maximum shifts from 691 nm (sample 3A, 100 ℃) to 824 nm (sample 3D, 160 ℃). Each peak has a broad width with $W_{1/2}$ (width at half-maximum) $\approx$ 150-190 nm. This is quite common for semiconductor nanomaterials, and especially for 11-13-15 materials.[41] According to previous studies, the broadened emission spectra are not related to size inhomogeneity but to the distribution of vibrational states.[42] This is also apparent for the $CuInS_2$ samples, which have a width of $W_{1/2} \approx$ 160-200 nm, as shown in Fig. 2.16.

The influence of reaction time was also investigated through emission spectroscopy. Three samples were synthesized with reaction times of 18 h, 36 h and 48 h at a temperature of 120 ℃, which is identical to sample 3B. As shown in Fig. 3.7 (b), although the colour of these four samples only change slightly from orange to red, the emission spectra of these samples indicate that both the intensity and the position of the emission are affected by the reaction time. Similar to the $CuInS_2$ samples in Chapter 2, a higher quantum yield is observed after a longer reaction time for these $CuInSe_2$ samples. The extended reaction time contributes to the formation of more perfect structures and leads to a decrease of defects inside the quantum dots, which contributes to a higher quantum yield. $CuInSe_2$ showed an improvement in quantum yield from 5.8 % (18 h reaction) up to 19 % (48 h reaction). However, the enhancement of quantum yield through the extension of reaction time is limited in scope, since excessive reaction times will lead to the formation of bulk materials instead of nanomaterials. The $CuInSe_2$ synthesized at 120 ℃ and for 48 h achieved the highest quantum yield, but is still not efficient enough

71

for industrial applications. However, it should be possible to obtain a better yield when coating CuInSe$_2$ with a CdS or ZnS shell.[42]
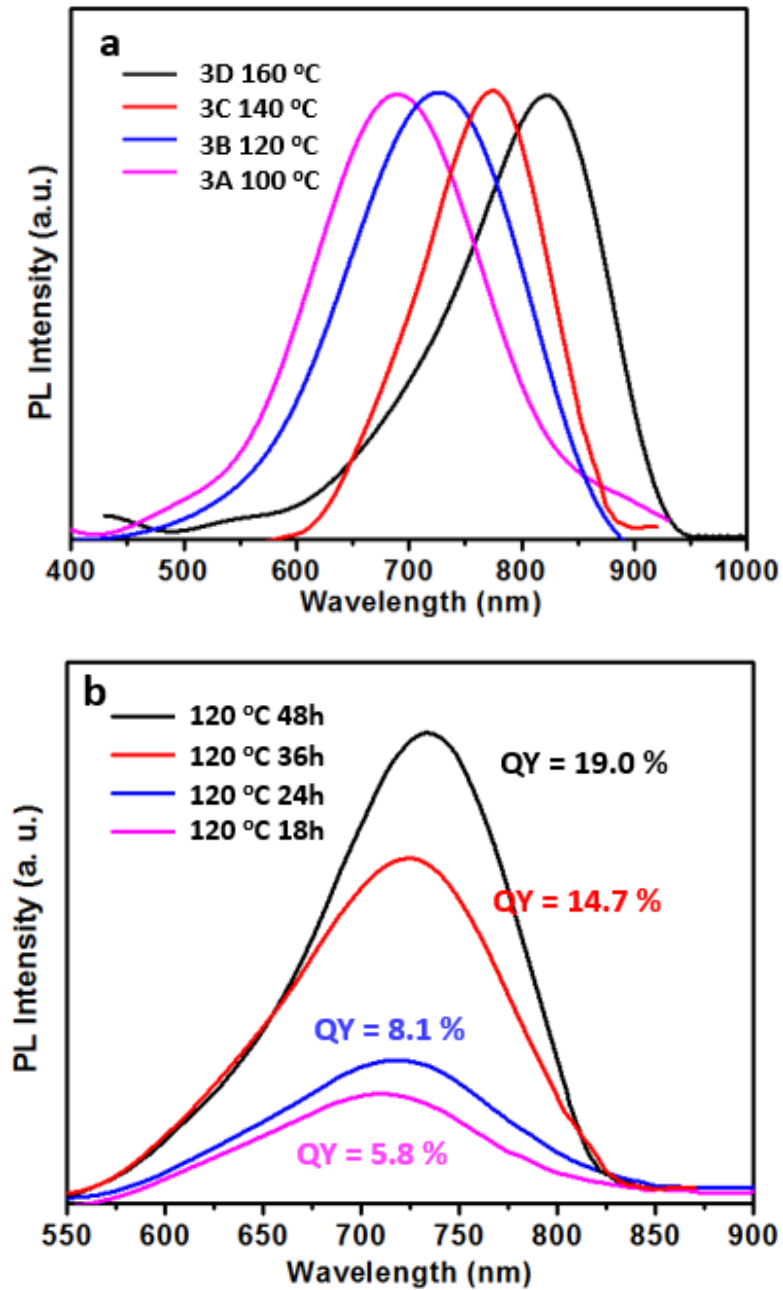
Fig. 3.7 Emission spectra of CuInSe$_2$ solutions under different synthesis conditions
a. different temperatures for 24 h reactions; b. various of reaction times at 120 ° C

3.3.1.4 **Electron Microscopy**

SEM images and EDX analyses were obtained for sample 3A, 3B and 3D. As shown in Table 3.2, all the samples showed a ratio of Cu : In : Se, close to 1:1:2. The In content of all the samples was always higher than that of Cu, which indicates the material synthesized belonging to In-rich material and this accounts for the emission properties.[43] Fig. S3-1 displays the SEM images for sample 3A, 3B and 3D. From the images, it is obvious that all the samples possessed a spherical morphology, however, the particle sizes were ~ 35 $\pm$ 8 nm, 46 $\pm$ 3 and 60 $\pm$ 11 nm as measured. All of these were at least 10 times larger compared to the calculated diameters (as shown in section 3.3.1.2) for individual nanoparticles from spectroscopic data. Similar to $CuInS_2$, this is due to the aggregation that occurred and it is hard to separate the individual particles when preparing SEM samples.

Table 3.2 Particle average diameters and Cu : In : Se ratio from SEM and EDX

Sample	T/ ℃	Diameter / nm	Cu : In : Se
3A	100	34.1 $\pm$ 8	1.0 : 1.11 : 2.03
3B	120	45.7 $\pm$ 3	1.0 : 1.18 : 2.01
3D	160	60.1 $\pm$ 11	1.0 : 1.05 : 1.77

Thus, TEM images and HR-TEM images were obtained to measure the diameter of individual $CuInSe_2$ nanoparticles (Figs. 3.8, 3.9 and 3.10). The TEM images of all these three samples demonstrate a relatively low crystallinity compared to $CuInS_2$, especially for sample 3A (Fig. 3.8). There are almost no well-resolved particle edges that can be observed. The size of the particles exhibited in TEM images are still larger than calculated values, which may be due to the failure to separate individual particles when preparing the TEM grids. HR-TEM images do, however, demonstrate that small particles are present. In order to determine the particle size, the particles on the most outside edge were measured as shown in inset (a) of Figs. 3.8, 3.9 and 3.10. The particle diameters of samples 3A, 3B and 3D are 2.4 $\pm$ 0.4 nm, 3.4 $\pm$ 0.2 nm and 3.9 $\pm$ 0.2 nm respectively, which match the expected values calculated from band gap energy (Fig. 3.6).

73
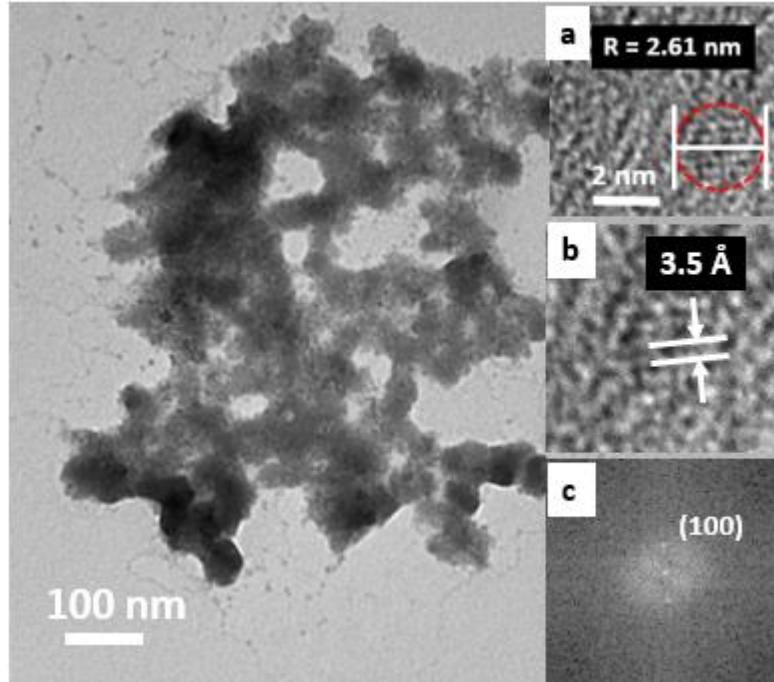
**Fig. 3.8　TEM, HR-TEM images and FFT for sample 3A
(Inset: a. HR-TEM image; b. Enlarge area of R1;
c. FFT image of this area)**
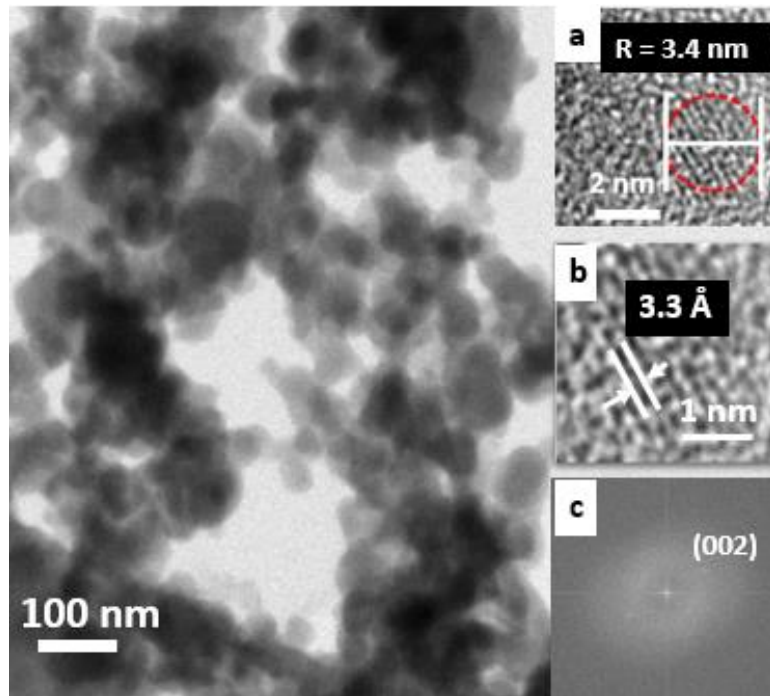
**Fig. 3.9　TEM, HR-TEM images and FFT for sample 3B
(Inset: a. HR-TEM image; b. Enlarge area of R1;
c. FFT image of this area)**
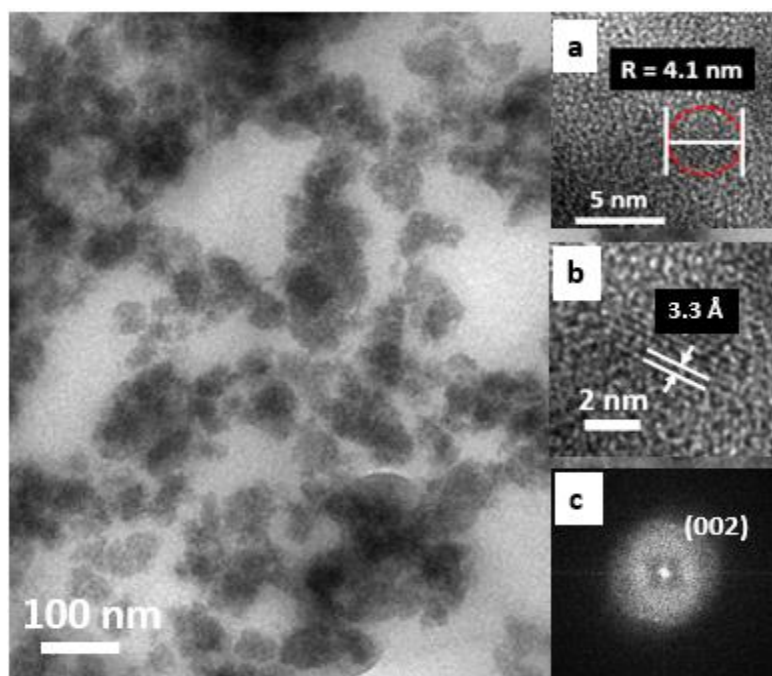
Fig. 3.10 TEM, HR-TEM images and FFT for sample 3D
(Inset: a. HR-TEM image; b. Enlarge area of R1;
c. FFT image of this area)

In addition, in each of the figures, inset figure (b) is the HR-TEM image which is presented to acknowledge the phases of particles by zooming inside the area R. For instance, the particle in sample 3A is shown to have clear lattice fringes with spacing of 3.5 Å, which corresponds to the distance of the (100) plane of the standard wurtzite $CuInSe_2$ (ICCD 01-078-5190). At the same time, the spaces between lattice fringes of both sample 3B and 3D is 3.3 Å, which is consistent with the distance of (002) plane. Also, the fast Fourier Transition (FFT) images of each sample are inserted as image (c). It is clear that no single crystals was formed due to the fuzzy light spots, but apparently, polycrystalline materials exists in all these samples. Further analysis through FFT images assigned the light dots to (100), (002) and (002) phases of wurtzite $CuInSe_2$ as labelled, and these results are consistent with the phases exhibited from lattice fringes. SAED patterns were also measured to obtain an overview within a large area, which is unlike FFT images showing the crystallinity of small area. The selected area is shown in Fig. S3-2. Due to the low crystallinity of samples, the SAED patterns were observed as very faint rings. After comparing to the standard wurtzite $CuInSe_2$ lattice data, all the phase rings belong to the expected crystal lattice (labelled in Fig. S3-3).

75

3.3.2 [(AgInS$_2$)$_x$] Nanoparticles

Various conditions for AgInS$_2$ synthesis were explored as summarized in Table 3.3. The addition of a second sulfur source was investigated, but few differences were observed between samples with and those without; as a result all further samples were synthesized without any second sulfur source. Different temperatures, reaction times and solvents were then explored as shown in Table 3.3.

Table 3.3   Various conditions for [(AgInS$_2$)$_x$] synthesis
(l: mother liquor; s: precipitate)

Sample	T/ °C	t/h	Solvent	Colour	
				s	l
4A	80	24	THF	brown	pale yellow
4B	100	24	THF	brown	yellow
4C	120	24	THF	brown	red
4D	120	48	THF	brown	brown
4E	80	24	DMF	black	colourless
4F	120	24	DMF	black	colourless

Similar to CuInS$_2$, coloured solids were precipitated directly from reaction solvents of AgInS$_2$ samples after cooling to room temperature. After separating the solid from the mother liquor, both the solid and mother liquors were gathered and analyzed. In comparison to the previous two series of samples (CuInS$_2$ and CuInSe$_2$), all the AgInS$_2$ precipitates from different reactions appeared as a red-brown solid even when synthesized at low temperature (sample 4A, 80 °C). When the reaction temperature was increased to above 120 °C, the solid products were black. Thus, using the reaction temperature to control the particle size is challenging for AgInS$_2$ system. Different reaction times were explored but it also had limited influence on tuning the product size (Table 3.3). For sample 4E and 4F, DMF was used as an alternate solvent, but both resulted in a black solid, which likely correspond to bulk materials.

76

However, there was one significant change: in contrast to $CuInS_2$ and $CuInSe_2$ samples, the colours of mother liquors changed from colourless to yellow and then to red with the increased reaction temperatures. This trend is completely opposite to that of $CuInSe_2$ discussed previously. One hypothesis is that at higher temperatures, the $AgInS_2$ products can be dissolved in the solvents, or, possibly, that this is due to the formation of a minor, secondary production.

3.3.2.1 **Powder X-ray Diffraction (PXRD)**

Due to the similar solid colours, two samples prepared under the most different reaction conditions (samples 4A and 4D) were chosen to investigate whether any changes were present in the PXRD patterns. Sharp reflections in the PXRD patterns of sample 4A and 4D are illustrated in Fig. 3.11, both of which display a wurtzite structure of $AgInS_2$ (ICCD 00-025-1328). The well-defined reflections indicate that both samples were bulk materials and the samples synthesized at "moderate" temperatures and times (sample 4B and sample 4C) would also have similar morphologies.
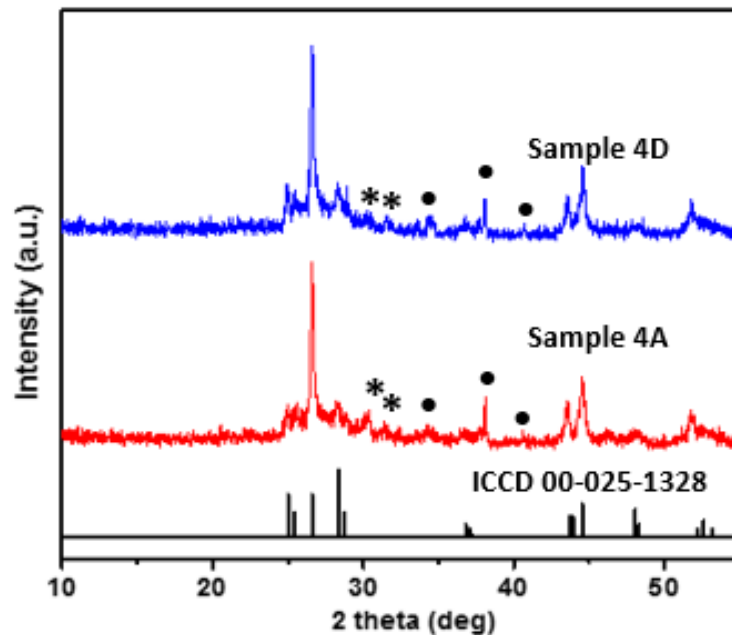
Fig. 3.11 PXRD patterns of sample 4A and 4D in Table 3.3

(symbol ∗: the peaks from chalcopyrite $AgInS_2$; symbol • : the peaks from Ag_2S)

77

As shown in Fig. 3.11, more than one impurity existed in both samples 3A and 3D. By matching the patterns with related products, the extra peaks are found to correspond to chalcopyrite $AgInS_2$ and Ag_2S, respectively (labelled as * and • in Fig. 3.11). The PXRD patterns of chalcopyrite $AgInS_2$ and Ag_2S are shown in Fig. S3-4. To date, for $AgInS_2$ samples, it is challenging to separate wurtzite products from impurities, and also it is not quite successful to control particle size.

3.3.2.2 **Optical Spectroscopy and Band Gap Energy**

Diffuse reflectance and suspension UV-vis absorption spectra were measured for the solid products from reaction and the secondary precipitates from mother liquors. All the absorption spectra were converted from diffuse reflectance data of the solid samples. In contrast to the $CuInS_2$ and $CuInSe_2$ samples discussed previously, there is no obvious shift of absorption maximum for $AgInS_2$, which is consistent with the colour observed. The spectrum of sample 4D is shown in Fig. 3.12 as an example. As shown in the spectrum, one obvious maximum can be resolved at ∼ 600 nm, which corresponds to a band gap energy of 1.88 eV as shown in the inset figure of Fig. 3.12. And band gap energy of bulk
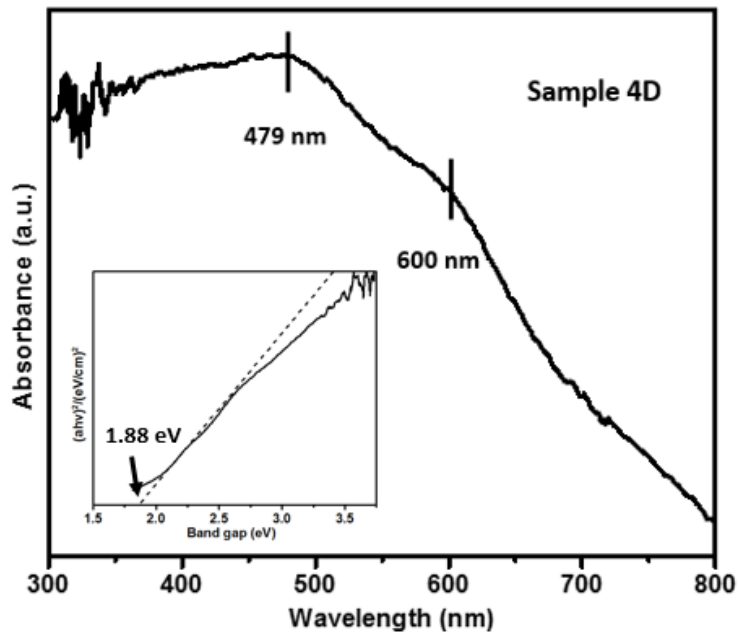
Fig. 3.12 Absorption spectrum from diffuse reflectance of sample 4D (see Table 3.3) (inset image: the band gap curve converted from the diffuse reflectance)

78

$AgInS_2$ is 1.87 eV, thus, the synthesized samples are very close to the bulk material rather than the nanoparticles. Interestingly, another peak is observed at a wavelength ~ 479 nm, and the plotted band gap curve also shows two peaks (the inset figure in Fig. 3.12). This probably indicates the formation of a secondary component of samples, however, more characterization needs to be performed to confirm the composition of this unknown component.
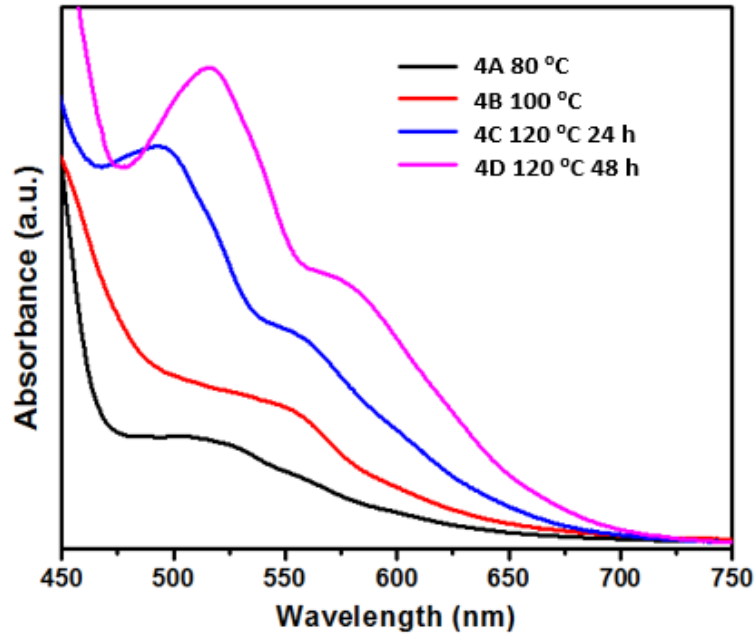
Fig. 3.13   UV-vis absorption spectra of the precipitate from sample 4A-4D (see Table 3.3)

As mentioned previously, unlike $CuInS_2$ and $CuInSe_2$, the colours of mother liquors of $AgInS_2$ samples exhibited a gradual change when the reaction temperature and time were changed. The UV-vis absorption spectra of the precipitates from the mother liquors are shown in Fig. 3.13. In agreement with the change of colour, which turned from yellow (sample 4A) to red brown (sample 4D), the absorption maximum has a red shift (520 nm → 557 nm) along with the increasing temperatures applied for the reactions. For sample 4D (120 ℃; 48 h) the peak shifted to 590 nm. This trend is consistent with the observed colour change, which is probably due to the growth of the particle size of the solute. And it is surprising that for samples 4C and 4D, another low energy peak appears, which also has a red shift. When the absorption spectra of sample 4D from solid sample (Fig. 3.12) and the secondary precipitate from the mother liquor (Fig. 3.13) are compared, it becomes

79

apparent that both peaks are positioned at a similar wavelength. This means that under these conditions, the particle size of both the solid and the precipitate are quite similar. One hypothesis is that when increasing the reaction temperature and time, it is possible that the $AgInS_2$ can redissolve inside solvents, and the $AgInS_2$ in particle size can also formed. This can be partially confirmed by the absorption spectra as shown in Fig. 3.13. However, this hypothesis needs to be confirmed in the future with more work.

3.3.2.3 **Electron Microscopy**

All solid samples were further characterized by electron microscopy. SEM images were obtained. Unlike $CuInS_2$ and $CuInSe_2$, most of the $AgInS_2$ products display a hexagonal morphology as shown in Fig. 3.14 (a). Hundreds of small, thin hexagonal plates were aggregated together with different orientations, and most of them had a thickness below ~ 5 nm. This morphology was further confirmed by TEM images (Fig. 3.14 (b)). The hexagonal plate shown in Fig. 3.14 (b) is relatively large and well defined, but most planes are within a diameter of 200 nm, similar to the two small planes overlapping together in the top left of Fig. 3.14. Along with EDX analysis that shows the ratio of Ag : In : S is 1 : 1 : 2, both images suggest that ~ 90 % of the $AgInS_2$ products are thin plates. Nanorods were also observed, as shown in Figs. 3.14 (c) and (d). Interestingly, the size of nanorods increases with reaction temperature (~ 55 $\pm$ 5 nm $\rightarrow$ 180 $\pm$ 20 nm in length). Although the amount of sample with this nanorod morphology is only ~ 5 % of the solid samples, this phenomenon provides an explanation of the colour change observed for the mother liquor. With increased temperature or time, the size of nanorods can be tuned to become larger. Also, as mentioned previouly, the colours of the mother liquors changed from pale yellow to brown (samples 4A to 4D) and this is probably due to the fact that the nanorods which have different sizes can be partially dissolved inside solvents. However, further experiments are required to confirm this hypothesis.
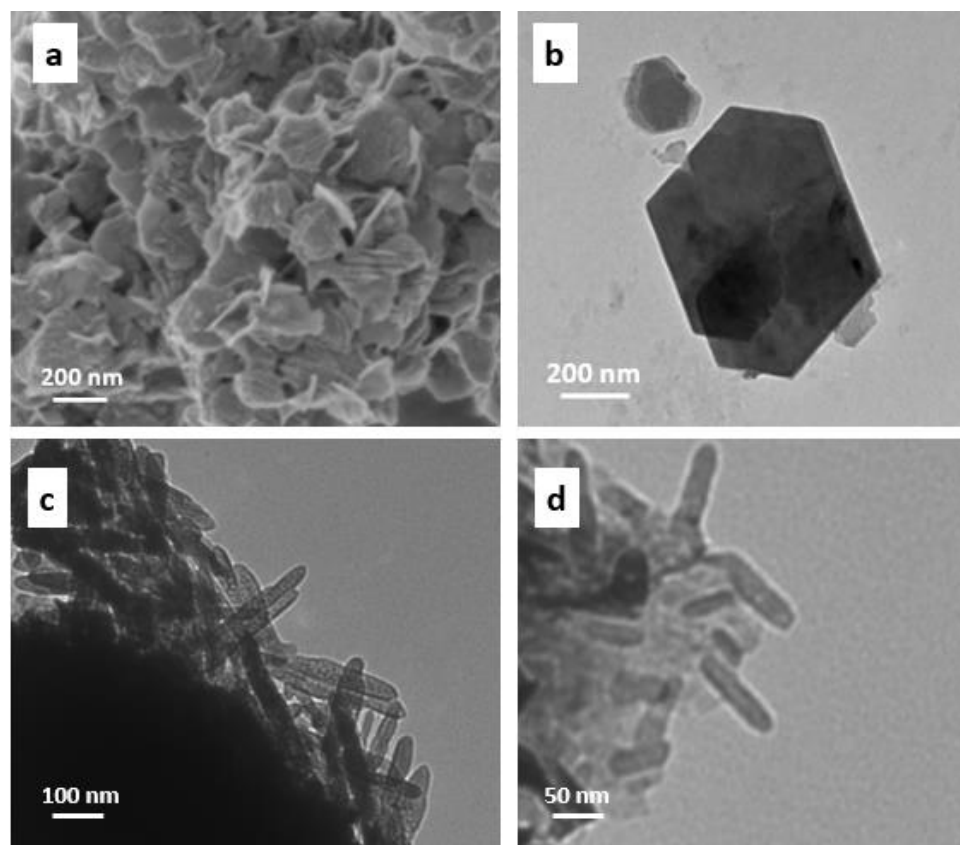
**Fig. 3.14   SEM image (a) and TEM images (b, c) of the solid sample 4D;
TEM image (d) of the solid sample 4A (see Table 3.3)**

3.4   Conclusions

Similar to $CuInS_2$, $CuInSe_2$ samples with tunable particle sizes can be obtained by using the solvothermal method with single source precursors. Without any secondary chalcogen source, the size of materials, noticeable as the colour of sample solutions, can be controlled (yellow, orange, red, dark red) by changing the reaction temperature and time. The particle sizes of three significant samples were found to be 2.4 ± 0.4 nm, 3.4 ± 0.2 nm and 3.9 ± 0.2 nm, which were convinced by the calculated diameters from absorption spectra. When decreasing the particle size, the band energy was improved to 1.62 eV from 1.04 eV, which is more suitable for the absorption of solar energy. Compared to $CuInS_2$ and $CuInSe_2$, $AgInS_2$ samples are more difficult to fabricate in a size controlled manner through the single precursor solvothermal method. The nanorods observed inside the products are exciting, but more experiments are required to understand the principles behind nanorod formation in this system.

81

References

1.   H. Hahn, *Angew. Chem.*, 1953, **65**, 538-538.

2.   S. Wagner, J. L. Shay, Migliora.P and H. M. Kasper, *Appl. Phys. Lett.*, 1974, **25**, 434-435.

3.   J. L. Shay, S. Wagner and H. M. Kasper, *Appl. Phys. Lett.*, 1975, **27**, 89-90.

4.   L. L. Kazmerski, G. A. Sanborn, F. R. White and A. J. Merrill, *B. Am. Physi. Soc.*, 1976, **21**, 430-430.

5.   L. L. Kazmerski, O. Jamjoum, P. J. Ireland, R. A. Mickelsen and W. S. Chen, *J. Vac. Sci. Technol.*, 1982, **21**, 486-490.

6.   L. L. Kazmerski, P. J. Ireland, O. Jamjoum, R. A. Mickelsen, W. Chen and A. H. Clark, *J. Vac. Sci. Technol.*, 1982, **20**, 308-309.

7.   L. Stolt, J. Hedstrom, J. Kessler, M. Ruckh, K. O. Velthaus and H. W. Schock, *Appl. Phys. Lett.*, 1993, **62**, 597-599.

8.   K. Ramanathan, M. A. Contreras, C. L. Perkins, S. Asher, F. S. Hasoon, J. Keane, D. Young, M. Romero, W. Metzger, R. Noufi, J. Ward and A. Duda, *Prog. Photovoltaics*, 2003, **11**, 225-230.

9.   K. Ramanathan, F. S. Hasoon, S. Smith, D. L. Young, M. A. Contreras, P. K. Johnson, A. O. Pudov and J. R. Sites, *J. Phys. Chem. Solids*, 2003, **64**, 1495-1498.

10.   Y. He, *CuInS2 Thin Films for Photovoltaic: Reactive Sputter Deposition and Characterization*, Master thesis, Justus Liebig University Giessen, 2003.

11.   S.-H. Wei, S. B. Zhang and A. Zunger, *Phys. Rev. B*, 1999, **59**, 2478-2481.

12.   D. S. Su and S. H. Wei, *Appl. Phys. Lett.*, 1999, **74**, 2483-2485.

13.   S. T. Connor, C. M. Hsu, B. D. Weil, S. Aloni and Y. Cui, *J. Am. Chem. Soc.*, 2009, **131**, 4962-4966.

14.   O. P. Agnihotri, P. R. Ram, R. Thangaraj, A. K. Sharma and A. Raturi, *Thin Solid Films*, 1983, **102**, 291-297.

15.   J. L. Shay, B. Tell, H. M. Kasper and Schiavon.Lm, *Phys. Rev. B*, 1973, **7**, 4485-4490.

16.   A. Rockett and R. W. Birkmire, *J. Appl. Phys.*, 1991, **70**, 81-97.

82

17. I. Repins, M. A. Contreras, B. Egaas, C. DeHart, J. Scharf, C. L. Perkins, B. To and R. Noufi, *Prog. Photovoltaics*, 2008, **16**, 235-239.

18. P. Jackson, D. Hariskos, E. Lotter, S. Paetel, R. Wuerz, R. Menner, W. Wischmann and M. Powalla, *Prog. Photovoltaics*, 2011, **19**, 894-897.

19. C. Guillen, E. Galiano and J. Herrero, *Thin Solid Films*, 1991, **195**, 137-146.

20. R. S. Roth, H. S. Parker and W. S. Brower, *Mater. Res. Bull.*, 1973, **8**, 333-338.

21. I. V. Bodnar, L. V. Yasyukevich, B. V. Korzoun and A. G. Karoza, *J. Mater. Sci.*, 1998, **33**, 183-188.

22. K. J. Hong, J. W. Jeong, T. S. Jeong, C. J. Youn, W. S. Lee, J. S. Park and D. C. Shin, *J. Phys. Chem. Solids*, 2003, **64**, 1119-1124.

23. M. Ortega-Lopez, O. Vigil-Galan, F. C. Gandarilla and O. Solorza-Feria, *Mater. Res. Bull.*, 2003, **38**, 55-61.

24. S. C. Abrahams and B. J., *J. Chem. Phys.*, 1973, **59**, 1625-1629.

25. I. Yonenaga, K. Sumino, E. Niwa and K. Masumoto, *J. Cryst. Growth*, 1996, **167**, 616-620.

26. T. Torimoto, T. Kameyama and S. Kuwabata, *J. Phys. Chem. Lett.*, 2014, **5**, 336-347.

27. M. Williams, R. M. Okasha, J. Nairn, B. Twamley, T. H. Afifi and P. J. Shapiro, *Chem. Commun.*, 2007, **30**, 3177-3179.

28. H. C. Yoon, J. H. Oh, M. Ko, H. Yoo and Y. R. Do, *Acs Appl. Mater. Interfaces*, 2015, **7**, 7342-7350.

29. C. H. Lee, C. H. Wu and C. H. Lu, *J. Am. Ceram. Soc.*, 2010, **93**, 1879-1883.

30. H. Y. Chen, S. M. Yu, D. W. Shin and J. B. Yoo, *Inec: 2010 3rd International Nanoelectronics Conference*, 2010, **1**, 406-407.

31. Y. H. Yang and Y. T. Chen, *J. Phys. Chem. B*, 2006, **110**, 17370-17374.

32. S. M. Lee, Y. W. Jun, S. N. Cho and J. Cheon, *J. Am. Chem. Soc.*, 2002, **124**, 11244-11245.

33. J. Joo, H. B. Na, T. Yu, J. H. Yu, Y. W. Kim, F. X. Wu, J. Z. Zhang and T. Hyeon, *J. Am. Chem. Soc.*, 2003, **125**, 11100-11105.

34. B. L. Wehrenberg and P. Guyot-Sionnest, *J. Am. Chem. Soc.*, 2003, **125**, 7806-7807.

83

35. T. J. Coutts and J. D. Meakin, *Current topics in photovoltaics*, Academic Press, London, 1985.

36. B. M. Leonard and R. E. Schaak, *J. Am. Chem. Soc.*, 2006, **128**, 11475-11482.

37. H. Nakamura, W. Kato, M. Uehara, K. Nose, T. Omata, S. Otsuka-Yao-Matsuo, M. Miyazaki and H. Maeda, *Chem. Mater.*, 2006, **18**, 3330-3335.

38. S. V. Ley, I. A. Oneil and C. M. R. Low, *Tetrahedron*, 1986, **42**, 5363-5368.

39. K. K. Banger, M. H. C. Jin, J. D. Harris, P. E. Fanwick and A. F. Hepp, *Inorg. Chem.*, 2003, **42**, 7713-7715.

40. T. C. Deivaraj, J.-H. Park, M. Afzaal, P. Obrien and J. J. Vittal, *Chem. Commun.*, 2001, **22**, 2304-2305.

41. W. G. J. H. M. van Sark, P. L. T. M. Frederix, A. A. Bol, H. C. Gerritsen and A. Meijerink, *Chemphyschem.*, 2002, **3**, 871-879.

42. H. Z. Zhong, Z. L. Bai and B. S. Zou, *J. Phys. Chem. Lett.*, 2012, **3**, 3167-3175.

43. B. K. Chen, H. Z. Zhong, W. Q. Zhang, Z. A. Tan, Y. F. Li, C. R. Yu, T. Y. Zhai, Y. S. Bando, S. Y. Yang and B. S. Zou, *Adv. Funct. Mater.*, 2012, **22**, 2081-2088.

CHAPTER 4. Conclusions and Future Work

A new synthetic route which is clean, facile and efficient was developed for the preparation of wurtzite based ternary semiconductor nanoparticles with controllable sizes. By using solvothermal methods and single source precursors, three sets of samples ($CuInS_2$, $CuInSe_2$ and $AgInS_2$) were examined in this thesis.

As mentioned in Chapter 2, the effort to develop $CuInS_2$ nanoparticles with tunable sizes and optical properties through various precursors, reaction times and temperatures, together with varying the amount of a secondary sulfur source resulted in an effective and straightforward synthetic route. It was found that the choice of single source precursor was crucial if low temperature reactions were required to control the size of nanoparticles synthesized. Three precursors, $[(Ph_3P)_2CuIn(SR)_4]$ (**1**, R = Ph; **2**, R = ^tBu; **3**, R = Et), were probed at reaction temperatures from 80 ℃ to 200 ℃. Due to the suitable S-C bond enthalpy, precursor **3** exhibited the best tunability of size. The experimental results indicate that the samples synthesized from precursor **3** possessed a wurtzite structure and exhibited increased particle size with increasing reaction temperature and time. Three different sizes of $CuInS_2$ nanoparticles were prepared with fine control: 2.4 ± 0.5 nm, 3.3 ± 0.4 nm and 4.4 ± 0.3 nm. In addition, the optical properties displayed via absorption and emission spectra were probed and both exhibited remarkable trends that were linked to particle size. The quantum yields of emission for these samples were partially improved by increasing the reaction temperature or reaction time due to the formation of better defined structures. $CuInS_2$ nanoparticles synthesized at 160 ℃ for 36 h showed the highest quantum yield (11.5 %) among all samples in this set, and compared to previously published quantum yields of $CuInS_2$, a slight improvement was obtained.[1, 2] However, compared to other nanomaterials, this quantum yield was relatively low, and further improvement is required. For example, surrounding $CuInS_2$ nanoparticle cores with a ZnS or CdS overcoating shell could be one way to avoid non-radiative relaxation pathways and achieve a higher quantum yield.[3, 4] Also, by adapting the nucleation and diffusion controlled alloying strategies, incorporation of Zn or Ga into $CuInS_2$ nanoparticles is also a promising way to further improve the quantum yield of emission.[4-6]

A similar exploration of solvothermal conditions was performed on $CuInSe_2$ and $AgInS_2$ samples. As discussed in Chapter 3, $[(Ph_3P)_2CuIn(SePh)_4]$ was used as the single source precursor for $CuInSe_2$ preparation. Unlike $CuInS_2$ samples, the tunability of color was achieved simply by a change of reaction temperature, even without the addition of an ancillary source of selenium. Thus, this is the first successful exploration of real "single source" synthesis by using solvothermal method and this "greener" approach provides this method to be competitive in the future. Without the addition of secondary chalcogen source, $CuInSe_2$ nanoparticles formed directly from one-step solvothermal reactions. The particle sizes of the synthesized wurtzite $CuInSe_2$ samples were 2.4 ± 0.4 nm, 3.4 ± 0.2 nm and 3.9 ± 0.2 nm, respectively. The band gap was improved dramatically from 1.04 eV (bulk) to 1.62 eV (Sample 3A, 2.4 ± 0.4 nm), which corresponds to a minimum wavelength of light at ~765 nm for exciton pair generation. This means that the tuned $CuInSe_2$ nanoparticles will form an exciton pair under exposure to visible light, and thus will be more efficient in utilizing the broadband visible light emission of sunlight than $CuInSe_2$ bulk materials which can only absorb the infrared light. For the optical properties, similar shifts of absorption and emission maximum were observed. The $CuInSe_2$ samples showed a higher quantum yield of 19 % when the reaction time was extended to 48 h at a temperature of 120 °C. The next step is to obtain a higher quantum yield for this material, following a similar modification method as outlined for $CuInS_2$ such as surface modification (core/shell structure) and composition modification (Zn alloying). Such materials can be further applied for the fabrication of solar cells to explore the conversion efficiency. An alternate approach to make these samples through a solvothermal method could be to use other single source precursors such as $[(n-Bu_3P)_2CuIn(SePh)_4]$ and $[(Ph_3P)_2CuIn(SeEt)_4]$, which have already been prepared and used in literatures to synthesize $CuInSe_2$.[7-9] Moreover, it is interesting that all samples of $CuInSe_2$ displayed modest solubility. As a result, it may be possible to obtain single crystals with clearly defined structures: currently very few reports have discussed the structures of ternary semiconductor nanoclusters.

The preparation of $AgInS_2$ samples was proved to be more challenging than originally expected and was an interesting contrast to the previously discussed sets. All

89

AgInS$_2$ samples were prepared by using [(Ph$_3$P)$_2$AgIn(SOCH$_3$)$_4$] as precursor. However, unlike the previous two sets, using this precursor material failed to exert appreciable control over the particle size. The solid state absorption spectra of the samples synthesized under different temperatures shared a similar maximum around 600 nm: the samples were confirmed to be bulk material rather than in nanoparticle form. Interestingly, there was also a small amount of nanorods observed within each sample. The size of these nanorods showed an increase when the reaction temperature was changed from 80 °C to 120 °C. In contrast to solid samples that precipitated directly, the samples precipitated from mother liquors showed a distinguishable absorption that was consistent with observed colours. One hypothesis is that for AgInS$_2$ samples, the products can be partially redissolved in reaction solvent and form a second set of products at higher temperatures and longer reaction times. To date, it was found that it is quite challenging to fabricate AgInS$_2$ quantum dots in this manner. Future work will include more detailed characterization of the AgInS$_2$ samples, especially for the precipitations from mother liquor.

Overall, both the CuInS$_2$ and CuInSe$_2$ samples can be prepared successfully with controllable particle sizes below 10 nm through solvothermal method and single source precursors, while this synthetic route is much more challenging for AgInS$_2$. All of the samples were shown to adopt the wurtzite structure and this structure contributes to the higher conversion efficiency due to a flexible stoichiometry. It was found that by decreasing the particle size, the nanoparticle band gaps can be tuned to better match with solar spectrum, and especially for CuInSe$_2$, which was tuned to take full advantage of visible light from infrared region which is available for bulk CuInSe$_2$. This might enhance the conversion efficiency dramatically when fabricated in the solar cells in the future. Using this synthetic method, the quantum yield of both CuInS$_2$ and CuInSe$_2$ had a slight improvement compared to previous reports, but was still relatively low compared to other nanomaterials such as CdS.[10] There remain some uncertainties about this new synthetic system, such as the single crystal structures of these materials, the mechanism of synthesis and the phase control procedure. Although it is challenging to explore these intricacies, answering these questions will improve the understanding of these materials.

References

1. L. Li, A. Pandey, D. J. Werder, B. P. Khanal, J. M. Pietryga and V. I. Klimov, *J. Am. Chem. Soc.*, 2011, **133**, 1176-1179.

2. W. S. Song and H. Yang, *Chem. Mater.*, 2012, **24**, 1961-1967.

3. R. G. Xie, M. Rutherford and X. G. Peng, *J. Am. Chem. Soc.*, 2009, **131**, 5691-5697.

4. H. Z. Zhong, Z. L. Bai and B. S. Zou, *J. Phys. Chem. Lett.*, 2012, **3**, 3167-3175.

5. J. Zhang, R. G. Xie and W. S. Yang, *Chem. Mater.*, 2011, **23**, 3357-3361.

6. W. J. Zhang and X. H. Zhong, *Inorg. Chem.*, 2011, **50**, 4065-4072.

7. K. K. Banger, J. Cowen and A. F. Hepp, *Chem. Mater.*, 2001, **13**, 3827-3828.

8. S. L. Castro, S. G. Bailey, R. P. Raffaelle, K. K. Banger and A. F. Hepp, *Chem. Mater.*, 2003, **15**, 3142-3147.

9. M. Williams, R. M. Okasha, J. Nairn, B. Twamley, T. H. Afifi and P. J. Shapiro, *Chem. Commun.*, 2007, **30**, 3177-3179.

10. N. Gaponik, D. V. Talapin, A. L. Rogach, K. Hoppe, E. V. Shevchenko, A. Kornowski, A. Eychmuller and H. Weller, *J. Phys. Chem. B*, 2002, **106**, 7177-7185.

Appendix
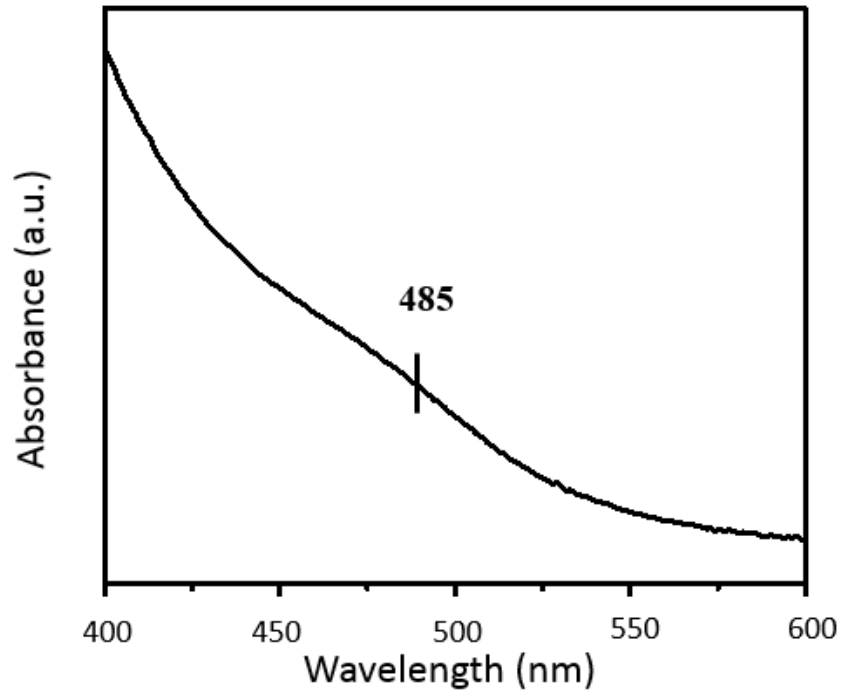
Fig. S2-1　Absorption spectrum of sample 1-3K (140 ℃)
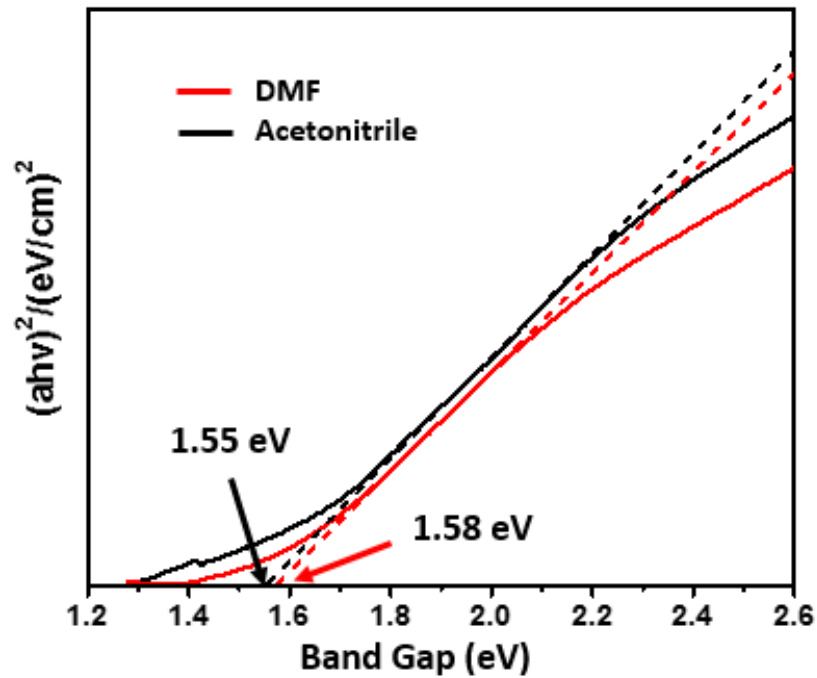
Fig. S2-2　Band gap curves of samples in Fig. 2.6

(size: sample from DMF: 5.1 nm; sample from acetonitrile: 6.1 nm)
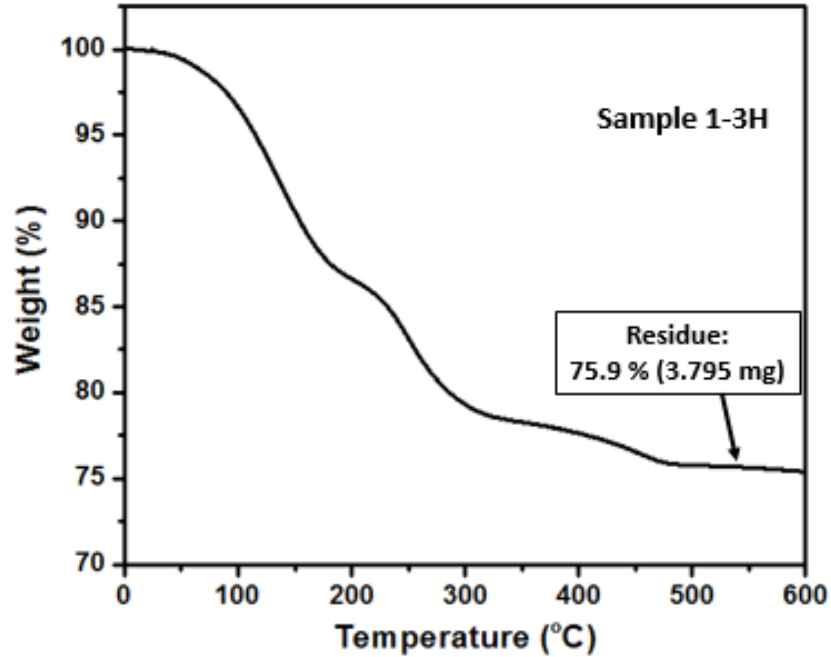
Fig. S2-3   TGA analysis for sample 1-3H
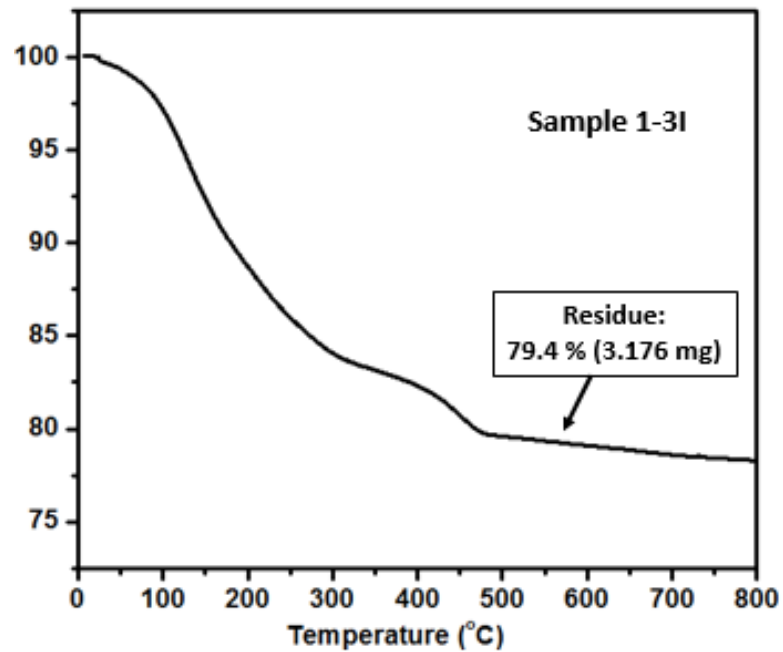
Fig. S2-4   TGA analysis for sample 1-3I

$CuInS_{2-X}(SEt)_{2X}$ is believe to be the formula of sample 1-3H and 1-3I. Based on the ratio of Cu:In:S, which is 1.19:0.90:2.59 and 1.05:0.94:2.51, after the thermal decomposition, the SEt group will evaporate as HSEt and leave $CuInS_{2-X}$ as residue. The calculated percentage of residue for sample 1-3H and 1-3I are 75.4 % and 78.5 %, respectively.

93
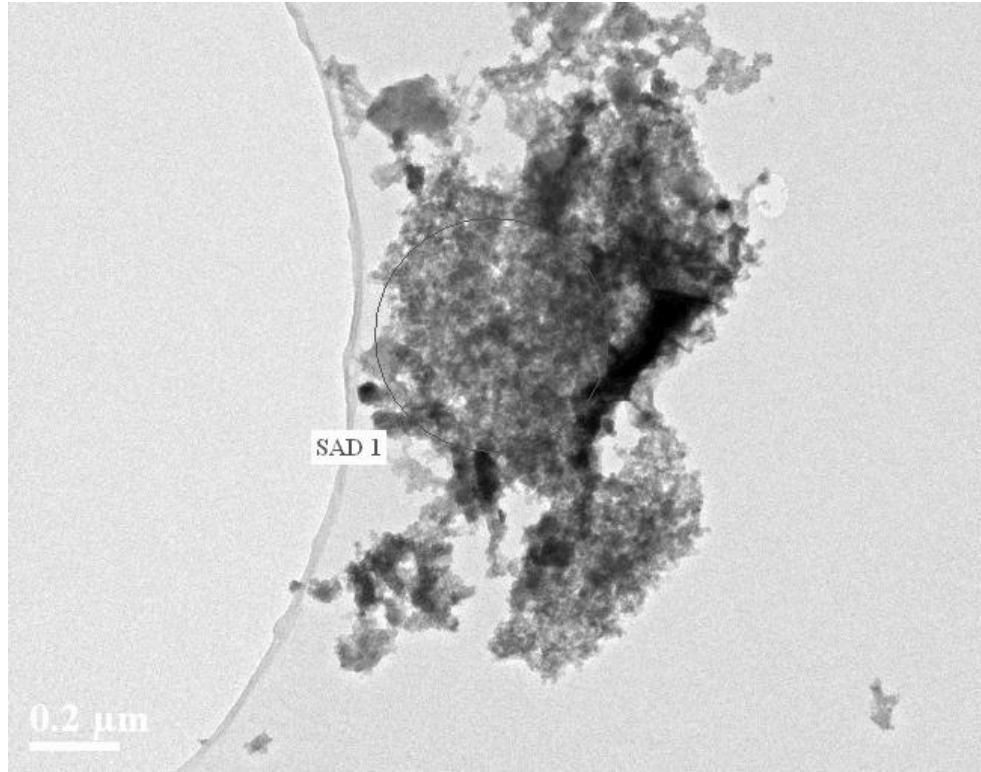
Fig. S2-5   Selected area for SAED pattern for Fig. 2.12
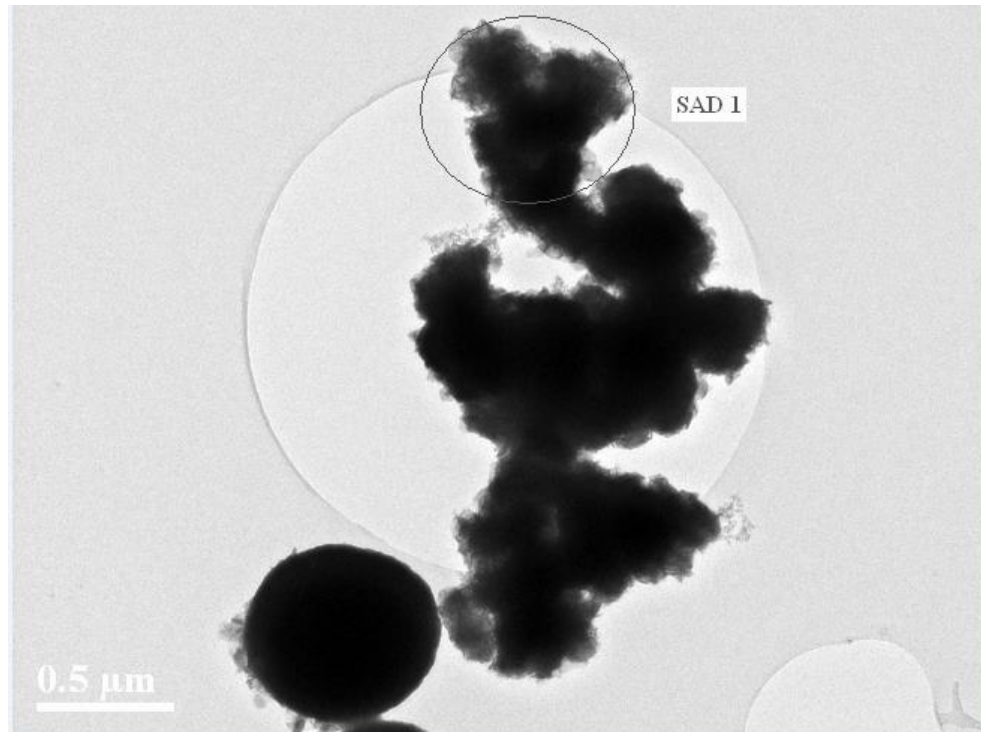
Fig. S2-6   Selected area for SAED pattern for Fig. 2.13

94
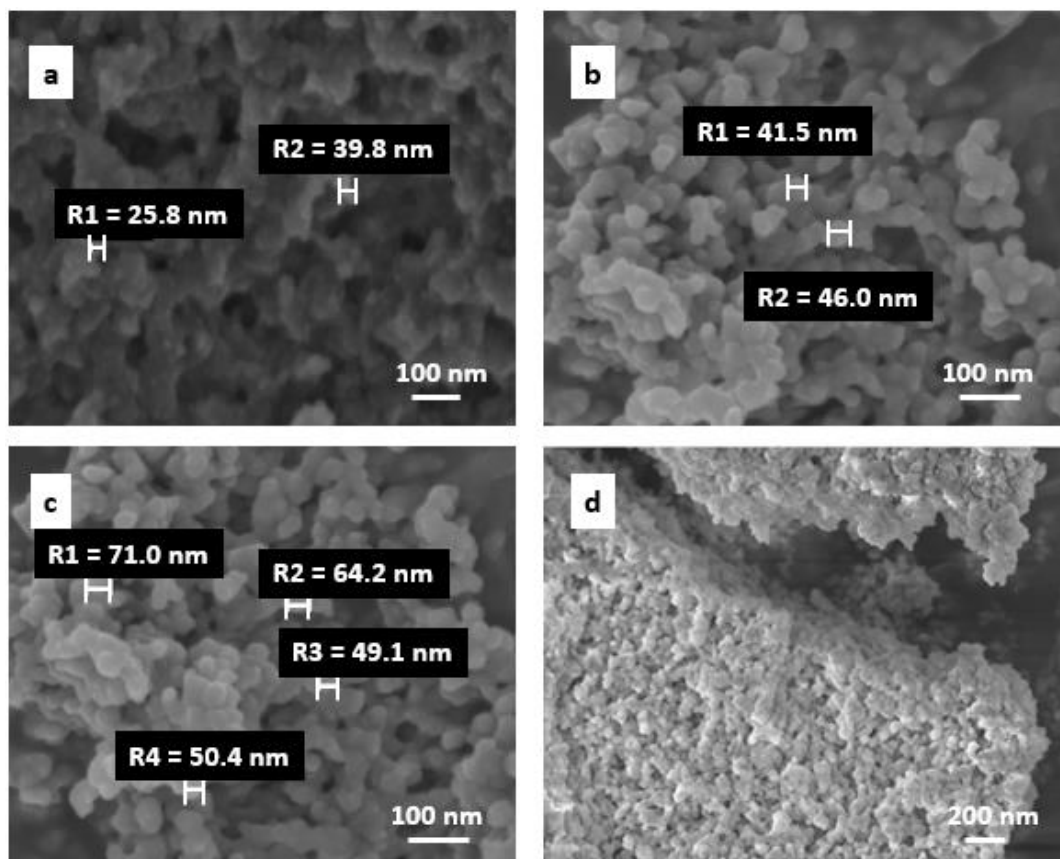
**Fig. S3-1   SEM images for samples 3A (a), 3B (b) and 3D (c)
low resolution of sample 3D (d)**
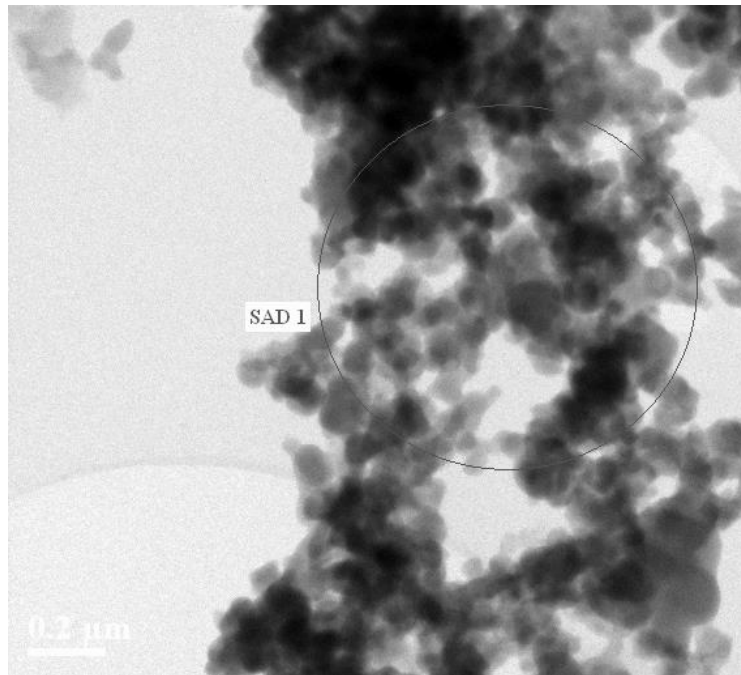
Fig. S3-2 Selected area for SAED pattern for sample 3D
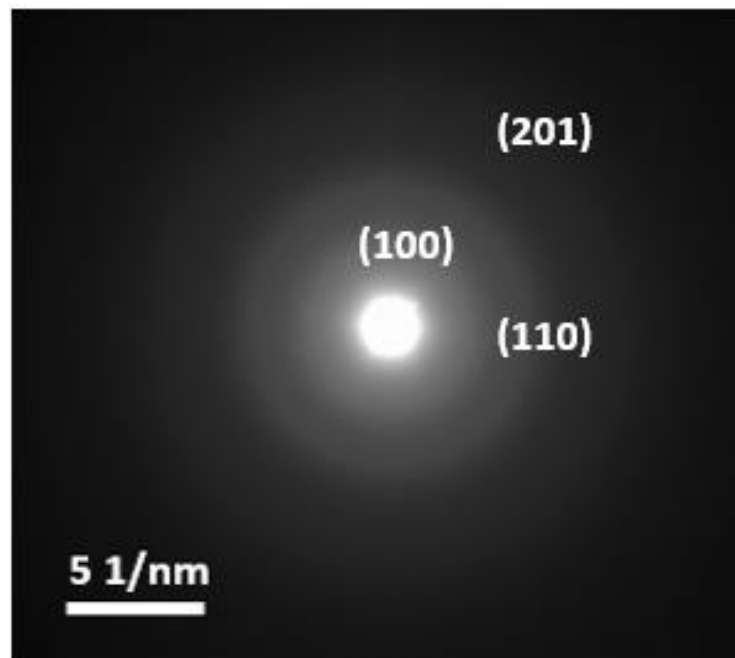
Fig. S3-3 SAED pattern for sample 3D

96
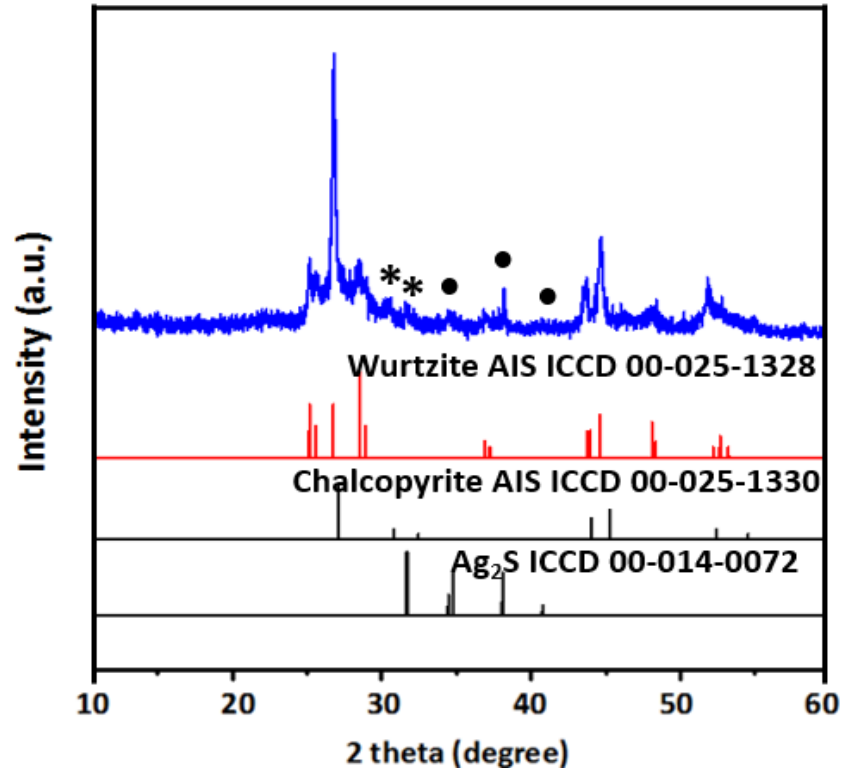
Fig. S3-4   PXRD patterns for sample 4A compared to chalcopyrite AgInS₂ and Ag₂S

Copyright information and permissions

Fig. 1.2 Classification of nanosemiconductors based on dimensionality

98

Fig. 1.3 Optical Properties of Nanomaterial in Different Size

Fig. 1.6 Cu$_9$In$_{10}$S$_9$(SEt)$_{21}$(PPh$_3$)$_3$ nanocluster synthesized through single source decomposition method

100

Fig. 2.1 Different structures of CuInS$_2$ crystals

101

Fig. 3.1 (a) Regular chalcopyrite (b) CuAu-like chalcopyrite CuInSe$_2$ crystals

102

www.manaraa.com

Fig. 3.2 The (a) photoluminescence colours and (b) emission spectra of AIS doped with Zn. The value of x in $(AgIn)_xZn_{2(1-x)}(S_2CN(C_2H_5)_2)_4$ ranges from 0.4 to 1.0.

103

Curriculum Vitae

Name: Xuzhao Zhao

Employment:

2014 – present   **Research Assistant**, Department of Chemistry

The University of Western Ontario, London, Canada

2014 – present   **Teaching Assistant**, Department of Chemistry

The University of Western Ontario, London, Canada

2011 – 2014   **Assistant Engineer**, Department of R & D,

Dongfang Company

Sinopec China, Beijing, P.R. China

Education:

2014 – present   **Master of Science (Chemistry)**

Department of Chemistry

The University of Western Ontario, London, Canada

2007 – 2011   **Bachelor of Science (Applied Chemistry)**

Department of Science

Beijing University of Chemical Technology, Beijing, P.R. China

Courses in UWO:

Chemistry 9541 (Crystallography I) – 86

Chemistry 9531 (Molecular Energy Conversion) – 80

Chemistry 9581 (Basics of Solid-state NMR) – 84

Chemistry 9658 – 83